Scuola Normale Superiore – Pisa

Tesi di Perfezionamento in Fisica:

Invariant Mass Spectrum of Jet–Jet Events in Proton–Antiproton Collisions at $\sqrt{s}$ = 1.8 TeV

G. Punzi – Author

Candidato

Dott. Giovanni Punzi

Relatore

Chiar. Prof. Giorgio Bellettini

INDEX

Introduction

1. Physics motivations 1
   1.1 QCD: the standard theory of strong interactions
   1.2 Jets in hadron collisions
   1.3 Quark Compositeness

2. The CDF detector 5
   2.1 Overview
   2.2 Calorimetry
   2.3 Tracking

3. The data sample 13
   3.1 Trigger and DAQ structure
   3.2 The 1989 run and data sample

4. Offline jet finding 21
   4.1 Generalities on jet reconstruction
   4.2 Clustering algorithms of CDF
   4.3 Performance of clustering algorithms

5. Corrections to jet energy and momentum 27
   5.1 Evaluating the corrections
   5.2 The Correction Function

6. Tracking corrections 31
   6.1 Monitoring the resolution
   6.2 P_T balance of jet events
   6.3 Correction for non–linearity
   6.4 Correction for crack losses
   6.4 Correction Summary

7. Event selection 50
   7.1 Offline cuts
   7.2 Cosmic background

8. Resolution and Unsmearing 57
8.1 Formalism
8.2 Measuring the resolution
8.3 Smearing procedures
8.4 Results

9. Systematic uncertainties 73
9.1 Simulation uncertainty
9.2 Systematic uncertainties on the dijet cross section

10. Radiation effects 80
10.1 Definition of jet
10.2 ISAJET predictions
10.3 Distribution of non–leading jets in the data
10.4 Sensitivity of M_{jj} to QCD radiation
10.5 ISAJET vs. HERWIG
10.6 Sensitivity to the $\Delta\varphi$ Cut
10.7 Summary

11. Comparing data and theory 97
11.1 Absolute comparison to leading order QCD
11.2 Relative comparison to leading order QCD
11.3 Testing for quark compositeness
11.4 Lower limit to the compositeness scale
11.5 Conclusions

Introduction

This thesis reports on an experimental study of hard parton–parton interactions in proton–antiproton collisions at the highest energy currently available ($\sqrt{s}$=1.8 TeV) at the Tevatron Collider of Fermi National Accelerator Laboratory, USA. In high energy interactions, characteristic structures are present in the collision products: bunches of particles ("jets") traveling in a common direction that are regarded as fragmentation products of single hadron constituents ("partons"). In the present work we study the differential cross section for production of jet pairs as a function of their invariant mass, as a test of the current theory of hadronic interactions (QCD), and as a search for deviations that could signal new physics.

The data sample (almost 5 inverse picobarns of integrated luminosity) was collected with the Collider Detector at Fermilab (CDF), the first large general purpose experimental apparatus to take data at the Tevatron, during its very successful run of 1988/89.

Chapter 1 summarizes the physics motivations for this measurement. Chapter 2 and 3 describe the parts of the detector and of the acquisition system more directly involved. The off–line procedures follow, beginning with the jet finding algorithms (Chapter 4), and the jet energy and momentum calibration (Chapter 5). The following Chapters deal with the work done by the candidate. A jet–by–jet correction procedure to improve resolution, obtained by integrating the calorimetric data with tracking information is described in Chapter 6, the sample selection cuts in Chapter 7, the correction for the smearing due to finite detector resolution in Chapter 8, the analysis of systematic uncertainties in Chapter 9. A discussion of the difficulties introduced by the presence of additional QCD diagrams is given in Chapter 10. The results are compared with QCD and with composite models predictions in Chapter 11. The comparison allows us to push the lower limit on the energy scale for quark compositeness beyond 1 TeV.

Much care has been devoted to make our measurement easily comparable to QCD calculations to higher orders in α_s, that will presumably be available in the future (order α_s^3 calculations for the inclusive jet transverse energy spectrum are already available). This will allow a fuller exploitation of the information provided by our data than possible with the currently available theoretical calculations.

CHAPTER 1

Jets and QCD

1.1 QCD: the standard theory of strong interactions

QCD ("Quantum ChromoDynamics") is the part of the Standard Model describing the strongest of the four fundamental fields. This theory pictures all hadrons (strong–interacting particles) as bound states of quarks. Quarks are fundamental fermions, existing in three colors for each flavor, and interact via an octet of color field ("gluons"), according to a non-abelian SU(3) gauge symmetry.

The effective coupling has been evaluated as [1]

$$\alpha_s(Q^2) = \frac{16\pi^2}{(11 - 2/3N_f)\ln(Q^2/\Lambda^2)}$$

where N_f is the number of flavors. This expression includes the leading logarithms from all orders. It is of great importance that this "running" coupling constant goes to zero when Q^2 goes to infinity (as long as the number of flavors is less than 16). This fact ("asymptotic freedom") allows using perturbation theory in theoretical calculations to produce experimentally verifiable prediction at least for hard scattering processes. In fact, the large value of the coupling constant at limited Q^2 is the source of most of the mathematical complexities and uncertainties that still surround QCD calculations.

Since no quark has ever been observed free, in the Standard Model all observable objects are assumed to be color singlets. All barions are assumed to be a bound state of three quarks, and all mesons to be quark–antiquark states. There are strong indications that the confinement of quarks in these states is indeed a consequence of the QCD Lagrangian. Hadrons are described as composite objects containing "partons" (quarks and gluons), that, from the point of view of a very energetic particle appear as quasi–free objects.

1.2 Jets in hadron collisions

It follows from the hadron picture outlined above that we can divide a hard hadron collision into three independent phases, occurring on different time scales. Partons approach each other with some momentum distribution inside the parent hadron (structure functions). A hard

collision takes place between a pair of partons (regarded as free particles). New partons are generated by the two scattered partons and eventually cluster into hadrons (fragmentation).The final particles produced in the fragmentation process have limited transverse momenta relative to the primary parton direction. As a consequence, they appear as collimated beams of particles traveling around a common direction ("jets"). Experimental studies of jets, like the work described here, can therefore allow testing of the predictions of QCD .

1.2.1 Structure functions

The share of momentum by hadron constituents is summarized by probability distributions of the momentum fraction x carried by each parton type. In principle, these structure functions and their dependence on Q^2 are completely determined by the QCD Lagrangian. However, their determination implies non–perturbative calculations that today we do not know how to perform. Therefore, they must be at least partially determined from the experiment. Actually, since the evolution of the functions with Q^2 can be computed perturbatively, a measurement of the structure functions at a particular value of Q^2 is sufficient to calculate them at any other Q^2, provided Q^2 is large enough to make the parton description of the hadron meaningful. Several sets of structure functions have been evaluated by different authors. Popular examples are Duke–Owens' (DO) [2] and Eichten–Hinchliffe–Lane–Quigg's (EHLQ) [3]. DO structure functions are based on several sets of deep inelastic scattering data, and dimuon and J/ψ mass distributions. Since the gluon distribution are not directly obtainable form this data, two sets of fits were given. These distributions are strongly correlated with the assumed natural scale of momentum transfer, Λ. The choices were DO1 (softer gluon distribution, Λ=200 MeV) and DO2 (harder gluon distribution, Λ=400 MeV), in the hope of bracketing the "true" distributions. EHLQ structure functions are based on CDHS data only and are parametrized in terms of Chebychev polynomials. They also come in two sets with different gluon distributions, EHLQ1 and EHLQ2.

1.2.2 Hard Parton Collisions

The lowest order cross sections for elementary $2 \rightarrow 2$ parton processes have been calculated by several authors[3]. They have a simple form and are reported in Tab. 1.1 as functions of the Mandelstam variables. It can be seen from the numbers that at 90° the dominant process is $gg \rightarrow gg$. The two–jet cross section is evaluated to the leading order by summing all of these processes, weighted by the structure functions of the initial partons. The work described in the present thesis is the experimental measurement of this cross section as a function of s.

1.2.3 Hadronization

The process of hadronization is non–perturbative, and therefore QCD calculable only in principle. For this reason, several models of fragmentation have been developed, having a variable number of parameters to be determined experimentally.

In the independent fragmentation scheme, each parton is separately evolved into a parametrized distribution of hadrons. In the Lund scheme, color field strings are stretched between hadrons and then fragmented. In the cluster fragmentation each parton is evolved into a number of other partons of lower virtuality, and the final partons are then grouped in color–singlet hadrons. We have used extensively the ISAJET Montecarlo, that adopts a mixed method[4]: it first performs a parton pre–showering and then fragments the products with the independent fragmentation method.

In the present work, we are concerned about fragmentation because the detector response to a jet depends on how the jet fragments. Fragmentation affects the amount of energy lost in cracks, the effect of the calorimeter non–linear response, the energy lost outside the jet cone or spiraling without reaching the calorimeter, etc. We will discuss these effects in Chapters 5,6.

1.3 Quark compositeness

Several extensions of the Standard Model have been developed by theorists, that could cause a detectable deviation of the dijet cross–section from QCD predictions.

A natural speculation is that the quarks, instead of being the ultimate constituents, are actually composite particle themselves, being made of truly fundamental particles called "preons". These particles should be bound together by a new non–abelian field ("metacolor"), confining and asymptotically free as the standard QCD color field.

In this model, an effective 4–fermion interaction appears when the Q^2 of the parton interaction becomes large enough to approach the compositeness scale Λ_c^2. This would be similar to the low energy effect of W,Z bosons exchange in weak processes. This additional Feynman diagram would contribute to the scattering amplitude. At large enough values of Q^2 the contribution would become appreciable and produce a cross–section larger than predicted by QCD only. We will look for an effect of this kind in the high mass region of our spectrum (Chapter 11).

$q_i q_j' \to q_i q_j'$	$\frac{4\alpha_s^2}{9s}\frac{s^2+u^2}{t^2}$	14.8
$q_i \bar{q}_i \to q_j \bar{q}_j$	$\frac{4\alpha_s^2}{9s}\frac{t^2+u^2}{s^2}$	1.47
$q_i \bar{q}_i \to q_i \bar{q}_i$	$\frac{4\alpha_s^2}{9s}\left[\frac{t^2+u^2}{s^2}+\frac{s^2+u^2}{t^2}-\frac{2u^2}{3st}\right]$	17.3
$q_i \bar{q}_i \to g\,g$	$\frac{8\alpha_s^2(t^2+u^2)}{3s}\left[\frac{4}{9tu}-\frac{1}{s^2}\right]$	6.93
$g\,g \to q_i \bar{q}_i$	$\frac{3\alpha_s^2(t^2+u^2)}{8s}\left[\frac{4}{9tu}-\frac{1}{s^2}\right]$	1.00
$g\,q \to g\,q$	$\frac{\alpha_s^2(s^2+u^2)}{s}\left[\frac{1}{t^2}-\frac{4}{9su}\right]$	40.7
$g\,g \to g\,g$	$\frac{9\alpha_s^2}{2s}\left[3-\frac{tu}{s^2}-\frac{su}{t^2}-\frac{st}{u^2}\right]$	202.7

Tab. 1.1 Cross sections for elementary parton processes.The third column is the value of each contribution at $\theta=90°$ (arbitrarily normalized to the smallest value).

CHAPTER 2

The CDF Detector

Several papers appeared in 1987 and 1988, giving detailed information about the Collider Detector at Fermilab (CDF) [9]. In this chapter, after a quick detector overview, we give a synthetic description of the subsystems that are relevant to the present analysis. The emphasis will be on calorimetry and tracking at large angles.

2.1 Overview

CDF has been the first general–purpose detector to take data at the Tevatron Collider. The collider energy in the center of mass is 1.8 TeV, currently the highest in the world. Fig. 2.1 shows a cut–away view of CDF. The detector weighs 5000 tons and consists of a mobile (sideways to the beam) central part covering the angular region $10^\circ < \theta < 170^\circ$ and two identical forward and backward spectrometers, covering down to 1.7° from the beam. Additional tracking detectors at very small angle are used to measure elastic scattering and total cross section. The coverage in ϕ is 2π.

The central part consists of:

- Tracking: Vertex TPC (VTPC), Central Tracking Chamber (CTC)
- EM calorimeter: Central EM Shower Counter (CEM), Plug EM Shower Counter (PEM)
- Hadron calorimeter: Central Hadron Calorimeter (CHA), End Wall Hadron Calorimeter (WHA), Plug Hadron Calorimeter (PHA)
- Muon detector: Central Muon Chamber (CMU)

The CTC is surrounded by a superconducting solenoid coil (3 m outer diameter, 5 m long) producing a B field of 1.5 Tesla .The CEM and CHA are contained in 48 wedges arranged in 4 self-supporting arches that can be individually retracted for servicing.The whole assembly can be rolled from the assembly hall to the beam line.

The forward/backward spectrometers consist of

- Trigger counters: Beam-Beam Counters (BBC)
- EM calorimeter: Forward EM Shower Counter (FEM)
- Hadronic calorimeter: Forward Hadron Calorimeter (FHA)

- Muon detector: Forward Muon Spectrometer (FMU), employing magnetized iron toroids

These forward spectrometers were assembled in the interaction area and sit permanently on the Tevatron beam line.

2.2 Calorimetry

The calorimetric detectors cover the pseudorapidity range $|\eta|<4.2$ ($\eta \equiv -\ln(\tan(\theta/2))$). The segmentation of each calorimeter is uniform in η and ϕ. All calorimeters have a projective tower geometry and are of the sampling type. The sampling medium is scintillator in the central region ($\theta>30°$: CHA,CEM,WHA), while is gas proportional chambers at smaller angles. A summary of the main properties of the CDF calorimeters is reported in Tab. 2.1.

Our analysis involves mainly data collected in the central region ($|\eta|<1.3$). The remaining part is used on occasions to provide event topology information. The central region is segmented in $24 \times 24=576$ towers, each having a size 0.11 ($\Delta\eta$) $\times$ 15° ($\Delta\phi$). The range $|\eta|<0.9$ is covered by CHA+CEM, while WHA+CEM cover the range $0.9< |\eta| <1.3$. In the center to plug transition two towers on each end are WHA+PEM (Fig. 2.2). At $\eta = 0.0$ there is a few centimeters wide uninstrumented region between the two halves of the central calorimeters.

The thickness of the CEM is about 18 radiation lengths (with lead absorber). It contributes 1 interaction length for hadrons, in addition to the 4.7 (at 90°) of CHA (with iron absorber) and 4.5 of WHA (in the direction perpendicular to the calorimeter).

The readout of the CEM is realized with plastic sheets doped with wavelength shifters on the ϕ sides of each tower, bringing light to the guides which pass through holes in the hadronic calorimeter to reach the photomultipliers. Towers are read out on both sides, giving a rough indication of the ϕ position of the shower. The light collected on each side decreases exponentially with the distance traversed in the scintillator, therefore the quantity ln(Left/Right) is a measurement of the azimuth of the shower. A proportional strip chamber is embedded in the EM stack at the depth of about 6 radiation lengths. It gives a measure of the position and energy density of the shower in two dimensions (strips and wires) with a resolution of about 2 mm. The information from this chamber is essential in signalling isolated electrons, but is not used in our analysis.

In the CHA, the readout is performed with wavelength shifter strips on the θ sides of the towers, going to light guides at the azimuthal ends of the modules (Fig. 2.3).The comparison of the readings on the two sides gives again a ϕ measurement. This might not appear as obvious at a first sight, and was obtained by making the attenuation length in the BBQ bars much shorter than in the scintillator slabs. A rough φ measurement is thus obtained by the Left/Right p.m. pulse height ratio.

The phototube signal ratio is also useful in tagging particles going through the light guides

and emitting Çerenkov light ("hot spots"). Hot spots cause the L/R ratio to be abnormally high or low. The gaps in ϕ between modules have been protected by metal bars 10 radiation lengths thick. Test beam studies[10] have shown that this completely eliminates hot spots for electrons and photons, but not completely for pions. An offline cut on L/R eliminates any remaining background.

It is also possible for the arriving particle (of any kind) to interact very little in the φ cracks and part or all of the energy can escape detection by the calorimeter. Fig. 2.4 shows a test beam study of this effect. This is the larger response nonuniformity remaining after the careful equalization performed on the tower surface [10].

2.3 Tracking

The tracking detectors are the VTPC and the CTC. The VTPC is the innermost one, and tracks charged particles at angles greater than $\approx 3.5^\circ$ from the beam. It is made of eight octagonal time projection chambers in a row along the beam. Adjacent chambers have a relative rotation in ϕ of 11.3°, to avoid inefficiency for tracks passing through octant boundaries. Each chamber is divided by a central high voltage grid into two opposite direction drift regions (15.25 cm long). The sense wires at the chamber ends (24 in each octant) are parallel to the sides of the octagon, thus providing an r-z measurement. There are also 24 cathode pads for ϕ measurement, but the main purpose of the chambers is the measurement of tracks in the r-θ plane. The VTPC provides us with two kinds of information. First, it shows clearly whether the event is a true beam-beam collision, a beam gas collision, a false trigger, or a double beam-beam interaction (having two primary vertexes along z). Second, it gives the z position of the interaction vertex (with 3 mm resolution). In jet analysis this is used to derive from the impact point on the calorimeter the jet production angle.

The VTPC is surrounded by the CTC, a cylindrical drift chamber of radius 1.3 m that provides precise momentum measurement for all charged particles within $|\eta|<1$. Within this region, the design transverse momentum resolution is $\delta p_T/p_T = 2\cdot 10^{-3} p_T$ (p_T in GeV/c). This was recently enhanced to $1.1\cdot 10^{-3} p_T$ by a careful cell and wire software alignment and by constraining the tracks to come from the beam spot [11]. The chamber has 84 layers of sense wires, grouped into 9 super-layers; 5 axial super–layers are alternated to 4 stereo super–layers tilted by $\pm 3^\circ$ with respect to the beam axis. There are 12 layers in an axial super–layer, and 6 in a stereo one. The single cell space resolution is ≈ 200 μm, providing a z resolution of 4 mm ($0.2/\sin(3^\circ)$) in the stereo layers. An additional 3-dimensional point is provided by three layers of drift tubes (CDT) mounted on the external surface of the CTC. Tracks having transverse momentum smaller than ≈ 300 MeV do not reach the outer surface of the CTC, but keep spiraling inside.

In our analysis, we have used the CTC information to detect low momentum particles swept in and out of the jet cone by the magnetic field, to measure jet fragmentation in order to correct for the lower response of the calorimeter to soft tracks, and to monitor the amount of charged energy hitting insensitive calorimeter areas.We discuss these subjects in Chapter 6.

	CEM	CHA	WHA	PEM	PHA	FEM	FHA
$\|\eta\|$ coverage	0÷1.1	0÷0.9	0.7÷1.3	1.1÷2.4	1.3÷2.4	2.2÷4.2	2.3÷4.2
Tower size $\Delta\eta\times\Delta\varphi$	.11×15°	.11×15°	.11×15°	.09×5°	.09×5°	.1×5°	.1×5°
Longit. samples/tower	1	1	1	3	1	2	1
Active medium	polystyrene	acrylic	acrylic	Prop. tube chambers with cath. pad readout			
Thickness/tube size	.5	1.0	1.0	.7×0.7	1.4×0.8	1×0.7	1.5×1.0
Number of layers	31	32	15	34	20	30	27
Absorber	Pb	Fe	Fe	Pb	Fe	Pb/Sb	Fe
Absorber thickness	0.32	2.5	5.1	0.27	5.1	0.48	5.1
Total Depth	$18X_0/1\Lambda_a$	$4.7\Lambda_a$	$4.5\Lambda_a$	$20X_0$	$6\Lambda_a$	$25.5X_0$	$8.2\Lambda_a$
Typical high voltage	-1100	-1500	-1100	1700	2120	1900	2200
Typical tube/wire gain	$1.2\cdot10^6$	$6\cdot10^5$	10^6	$2\cdot10^3$	$2\cdot10^4$	$5\cdot10^3$	10^4
Typ. tower signal (pC/GeV)	-4	-4	-4	1.25	1.3	2	0.7
E resolution at 50 GeV (%)	2	11	14	4	20	4	20
Pos. resolution at 50 GeV	0.2×0.2	10×5	10×5	0.2×0.2	2×2	0.2×0.2	3×3

Tab. 2.1 Parameters of the CDF calorimeters.

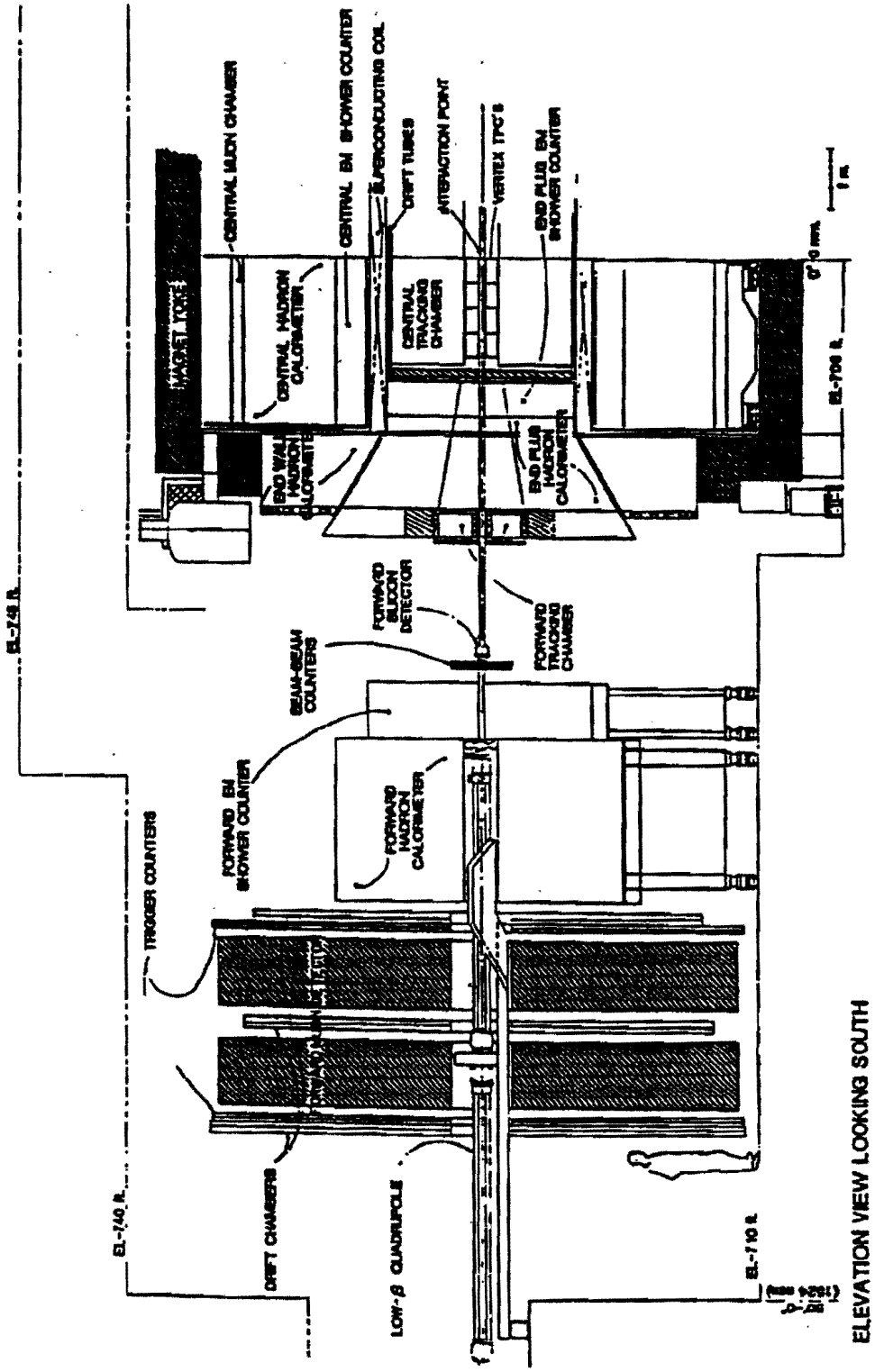

Fig. 2.1 Cut–away view of the CDF detector.

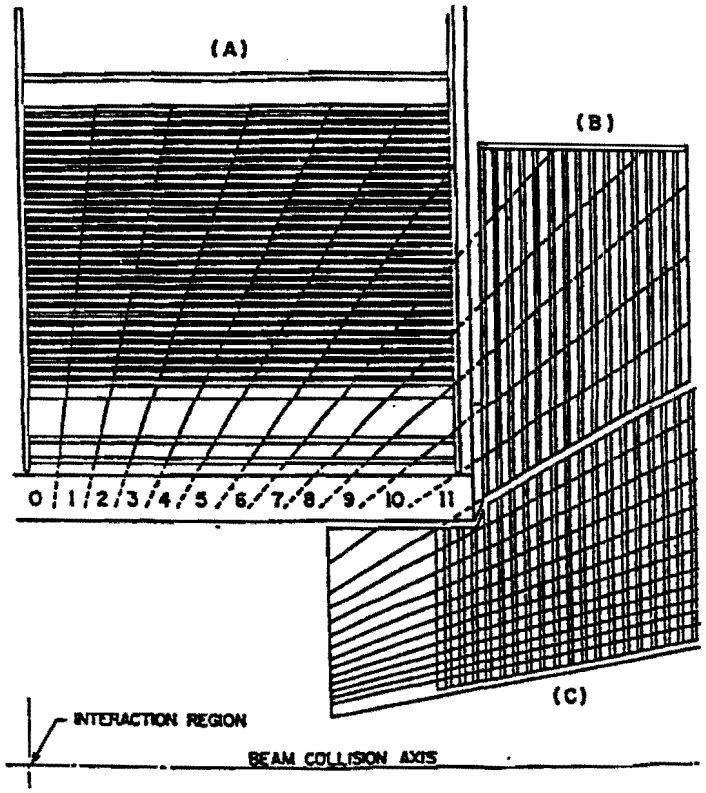

Fig. 2.2 Cut–away of a quadrant of the Central, Endwall, and Plug calorimeters.

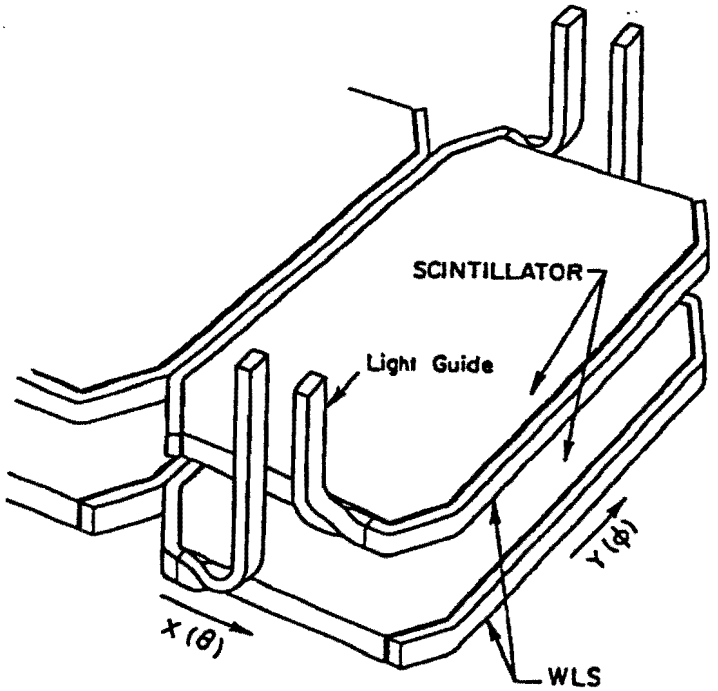

Fig. 2.3 Light collection system for CHA towers.

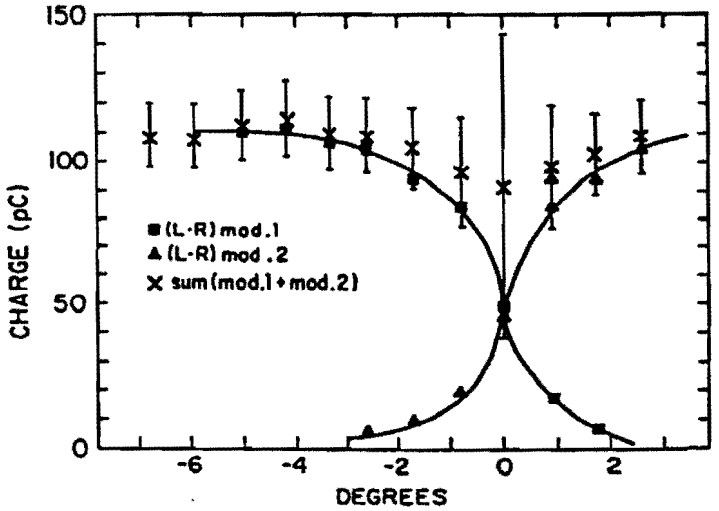

Fig. 2.4 φ scanning of the interface between two CHA modules with 50 GeV pions.

CHAPTER 3

The data sample

CDF is installed on one of the interaction areas of the Tevatron, that operated in the 1988/1989 run with 6 proton and 6 antiproton bunches of 900 GeV energy. The design luminosity of $10^{30}s^{-1}cm^{-2}$ was reached and surpassed. At this luminosity, the rate of proton–antiproton collisions in CDF is about 50 kHz, while the rate of recording events on tape must be reduced to ≈1Hz. Therefore, a drastic event selection must be made before storing on tape. This selection must be done mostly within the 3.7 μs available time between beam crossings, in order not to introduce dead time in the acquisition. This was a difficult task that could only partially be performed by the trigger system.

3.1 Trigger and DAQ structure

The CDF trigger is organized in a multi–level structure. The idea is to perform a reduction of rate at each step, giving time to the following level to perform at a lower rate a more elaborate decision and further reduce the rate. The operations performed range from a simple coincidence of trigger counters (BBC) at Level 0 to a full offline–type elaboration in FORTRAN language on dedicated processors at Level 3.

Several papers describe the structure of the data acquisition system of CDF [12]. With exception of the front end electronics, the system is realized with FASTBUS units. We give in this Chapter a simplified description of its functions, with some more detail on the selection of jet events.

3.1.1 Front End Electronics

Overall, there are a total of 10^5 channels to be read out in the CDF detector. About 40K (all tracking and trigger information) are read by the FASTBUS–based SSP's (SLAC Scanner Processors), and the remaining ≈60K channels (including calorimetry) are read by RABBIT electronics (Redundant Analog Bus–Based Information Transfer), scanned by MX modules. Each MX (in the control room) communicates with the downstream FASTBUS system through a MEP

(Multiple Event Port) module, and reads several RABBIT crates that are located in the collision hall, next to their detectors. The analog signals are digitized to 16 bits by EWE (Event Write Encoder) modules in the RABBIT crates. Those modules are also able to suppress channels below a threshold (software settable) before digitizing, and to subtract the pedestal from each channel, before passing the data to the MX.

The MX applies channel dependent corrections and can store up to four events while waiting for being read by the Event Builder.

3.1.2 Level 0

The Level 1 trigger electronics can in principle make its decision within the time between bunch crossings (3.7 μs). However, some extra time was required for the trigger analog input signals to settle to their final values. If one solves this problem by "brute force", one would cause a straight 50% deadtime already at Level 1. This difficulty will not be there in future runs. In the 1989 run, the problem was solved by introducing a fast coincidence between beam–beam counters left and right of the intersection region, and the bunch–bunch crossing gate. This allows rejecting no–interaction crossings and beam–gas interactions. This remedy works as long as the probability of a bunch–bunch crossing to give an event is low. This was not the case at the highest Tevatron luminosity. At the highest luminosity, the 6μs long gate opened by Level 0 caused a deadtime of nearly 20%.

3.1.3 Level 1

A scheme of the Level 1 and Level 2 trigger system is shown in Fig. 3.1. Most of the electronics is shared by the two systems.

The information available at Level 1 is:

- BBC;
- Presence of a CTC track with P_T above a given threshold from the Fast Track Finder;
- Presence of a muon candidate with P_T above given thresholds in central or forward chambers;
- Flags for elastic or diffractive candidates from the small angle system;
- Sum of E_T, $E_T\cos\varphi$ and $E_T\sin\varphi$ (EM, Had, and EM+Had separately) over the calorimeter.

All processing is done with analog signals, traveling on trigger dedicated lines independent of

the digitizing path.

In the calorimeter part of the trigger, the EM and Hadronic towers are processed separately. They are first grouped in "trigger towers" of size $\approx 0.22(\Delta\eta) \times 15^{\circ}(\Delta\phi)$, obtained by adding together two towers in the central region (that is, summing the outputs of 4 phototubes, with a FASTBUS module named "Tubesum"), or six towers in the gas calorimeters (done directly on the front end amplifiers). The 24 analog signals of each $\Delta\eta=0.2$ slice are fed to a RAW (Receive And Weight) card, which applies a linear correction to them in order to correct for pedestals and gain differences and to translate E into E_T[1] . Each RAW card sends the corrected tower outputs to a partner CAS (Compare And Sum) card, that performs the three sums E_T, $E_T\cos\varphi$, and $E_T\sin\varphi$, after suppressing the towers below a settable threshold. This sum is performed four times in parallel with four different thresholds. The card has a 24 bit register used as a mask to exclude bad channels from the sum.

The output of all CAS cards of each crate (10 crates total) are added together by a Crate Sum module, that also computes the sums $E_T\eta$ and $E_T\eta^2$ for use by Level 2. All sums are then digitized by 8 bit flash ADC's. Finally, the grand total of E_T, $E_T\cos\varphi$, and $E_T\sin\varphi$ is performed digitally by three Level 1 Sum boards, and compared to given thresholds. The final output of these boards is formed by combining logically the results of these comparisons for each of the 4 tower thresholds. Since the sums of $E_T\cos\varphi$ and $E_T\sin\varphi$ are the x and y components of the missing E_T vector, it is possible to select events according to their E_T and missing E_T.

The flags from the various systems are all routed to a module named FRED, who makes the final Level 1 decision with the help of a look–up table residing in a RAM. There are actually four RAM tables, and each of them is associated to a programmable prescale factor. The output is the logical OR of the four bits. In this way it is possible to trigger on rare processes at full efficiency while at the same time picking up a small subsample of events of a frequent kind. When an event is accepted, a Level 1 accept signal is sent to prevent a reset of the front end electronics, while Level 2 is started. A tipical rate out of Level 1was a few kHz. Level 1 is dead–time free.

3.1.4 Level 2

The Level 2 is designed to introduce less than $\approx 10\%$ dead–time. This means that Level 2 is allowed a time of the order of 10 μs to make a decision (a longer time is allowed for a small fraction of special events).

The additional pieces of information available at Level 2 are:

– More detailed information on stiff tracks in the CTC, including their azimuthal angle;

[1] The signals coming from the gas calorimeters already represent transverse energy; the signals from the central calorimeter represent E and are weighted by $\sin\theta$ in the RAW cards.

– More detailed information on muon candidates, including their z–φ positions;

– More accurate measurements of the calorimeter energy sums;

– Number and properties of energy clusters in the calorimeter (jet candidates), separately in EM and E_{tot}. For each cluster E_T, P_T, the (η,φ) centroid, and rms η and φ widths are available.

The Level 2 electronics can put together the information from different detectors. Tracks in the CTC and in the muon chambers are matched to establish "golden" muon candidates, CTC tracks are matched to EM clusters to make electron candidates, etc. This allows building many selective triggers that can run at the same time.

We include here a description of how the on–line cluster finder operates, that is basic to triggering on jets.

In the Level 2 cluster finder, the CAS cards are involved again, but this time the quantities added do not correspond to the entire calorimeter, but to a cluster. The procedure is repeated for several cycles by imposing a decreasing set of tower thresholds to CAS, starting from some high value (say, 100 GeV). When some towers show up above threshold, the ramp is stopped, and the addresses of these seed towers are sent to the Cluster Finder, on a 1008 bit bus (each bit is the logical OR of the hadronic and the EM flags). Then, a low threshold (order of 1 GeV) is used to select non–zero towers, and their addresses are sent to the Cluster Finder. The Cluster Finder than takes control, and builds clusters by addressing the nearest neighbor towers to a seed tower and turning them on if they pass the low threshold (a neighbor must share a side with the seed: "diagonal neighbors" are not considered). The lit towers send signals to their own neighbors, and so on, until no more towers are added. Then the binary array representing the cluster is sent to the CAS cards so that they can perform their sums using only the specified towers, and the process is repeated with another seed, with a cycle time of about 150 ns. When all seeds are used, the high threshold resumes ramping down until finding more seeds, and the whole process repeats itself.

At the end, the OR of all clusters is loaded into the CAS to reevaluate the global calorimetric sums with completely settled signals.

The Crate Sum modules work as in Level 1, but in addition they evaluate the sums of $E_T\eta$ and $E_T\eta^2$, and keep track of the number of towers in each cluster. The digitized data is then passed over to the Listmaker, that performs several calculations to build two 64 bit words for each cluster which are sent to the Level 2 Processors. Of the two words, one contains EM quantities and the other EM+Hadronic quantities. Each word contains: E_T, $E_T\sin\varphi$, $E_T\cos\varphi$ (10 bits each), η, σ_η (8 bits each), φ (7 bits), σ_φ (8 bits).

The Level 2 processors input the list of clusters at the rate of one every 150–200 ns. For each cluster, three 64 bit words are received, two of them coming from the Listmaker, and the third one from the Timing Control, containing the number of towers in the cluster, the address of the seed

tower, and the presence and momentum of a possible stiff track pointing to the cluster. The data is used in parallel by a number of Mercury Modules, each of them being dedicated to the calculation of a specific quantity. One module counts the number of clusters above a threshold and their total E_T, another one selects electron candidates based on EM/hadronic ratio, cluster width, and presence of a stiff track, another selects muon candidates by matching muon chambers, CTC tracks, and calorimetric energy, etc. Additional modules can be added at any time if one wants to evaluate additional quantities. Each module summarizes the results of the evaluation in a summary register. A Jupiter module reads all registers and performs an elaboration according to a microcode program to arrive at an accept/reject decision. In this way, sophisticated trigger decisions can be made in a few microseconds. The module can be reprogrammed whenever needed to change the decision logic.

The Level 2 accept/reject signal is sent to FRED, who takes the final Level 2 decision.

It is necessary at this point to mention the partitioning feature of the CDF trigger. The CDF detector can be split in up to four independent partitions. Each partition can run independently with its own trigger. The readout of each partition is controlled by a different Trigger Supervisor, and all Level 2 accept/reject signals are sent to FRED, that takes the global Level 2 decision. Each partition is in "standard" or "veto" mode, and the event is accepted if at least one of the standard partitions accepts it, and no veto partition rejects it. A start scan signal is than issued, and the system is dead for a time of about 1 ms. The total rate out of Level 2 is of the order of a few Hz, and the associated deadtime is normally negligible.

Besides the four "physics" partitions, other 12 partitions exist for calibration and debugging. Those do not use the Level 1/Level 2 scheme and are handled by a different type of FRED boards called "Autonomous FRED", in contrast with the other one that is called "CDF FRED".

3.1.5 Level 3

The Level 3 hardware is a farm of 32 bit processors in VME crates, each having 4 Mbytes of RAM. The processors run FORTRAN programs, of the same kind as the offline analysis programs. The trigger logic that can be implemented at this level is very complex. Some cleanup procedures (discarding cosmic rays, particle splashes from the Main Ring, bursts of cable noise, etc.) are performed by Level 3, decreasing the fraction of useless events written to tape. A further reduction of rate is accomplished by partial or total in this way, arriving at the final tape recording speed of ≈ 1 Hz.

3.2 The 1989 run and data sample

The data for the analysis presented in this thesis were collected during the Tevatron collider run started in October 1988 and ended in May 1989. The accelerator performance was very good. The peak luminosity often exceeded 10^{30} $cm^{-2}s^{-1}$, and the luminosity decay constant was ≈30 hours. The majority of stores were terminated voluntarily when a fresh store was ready, rather than by failures. A total of 9.05 pb^{-1} of integrated luminosity was delivered to CDF, of which 4.69 pb^{-1} were logged on tape (total of ≈5500 tapes). The inefficiency was due to trigger deadtime, deadtime at the start and end of runs, deadtime caused by DAQ failures, and time needed to re–calibrate some detectors at the start of run. Fig. 3.2 shows a plot of integrated luminosity vs. time. More than thirty triggers ran simultaneously, tuned to different physics processes. The following is a (partial) list of frequently used triggers :

- Minimum bias
- One or more electrons (E_T>12 GeV)
- One or more muons (P_T>9 GeV)
- At least one electon (E_T>12 GeV) and one muon (P_T>5 GeV)
- Two muons (P_T>3 GeV)
- Neutrinos: missing E_T>25 GeV
- One or more jets (E_T>20,40,60 GeV)
- Three or more jets (E_T>15 GeV)
- Photons
- Jet + lepton

The sample for our analysis comes from the inclusive jet triggers, that require at least one calorimetric cluster to be found by the Level 2 cluster finder. Three such triggers were present, with E_T thresholds of 20, 40, and 60 GeV (named JET_20, JET_40, and JET_60). The rate increases exponentially by lowering the threshold, therefore the JET_40 and JET_20 rates were pre–scaled by a factor of 10 to 30 and 100 to 300 respectively, depending on Tevatron luminosity. The JET_60 trigger was not prescaled. The effective integrated luminosities of the subsamples are approximately 4.7pb^{-1} for JET_60, 0.16 pb^{-1} for JET_40, and 0.016 pb^{-1} for JET_20.

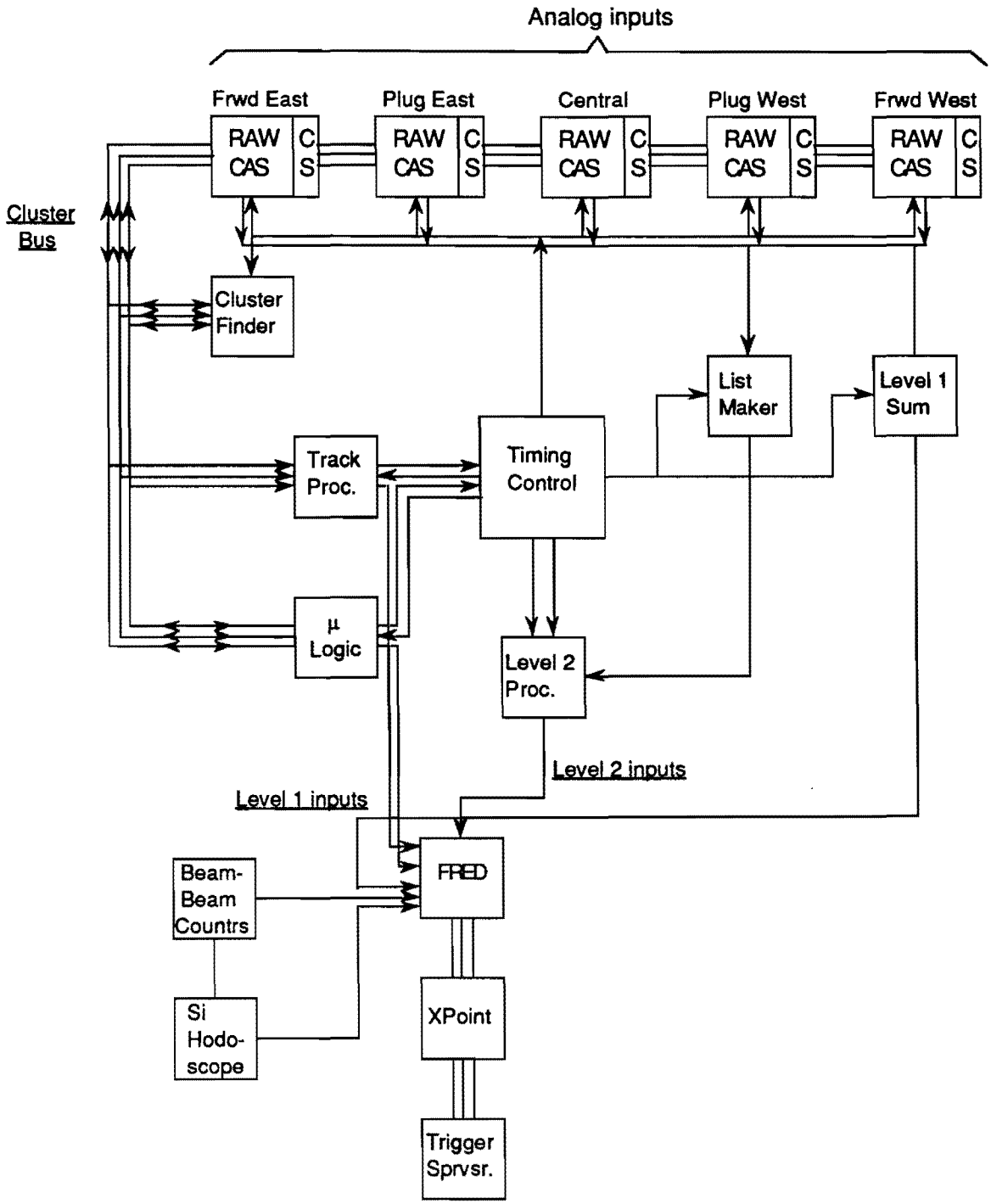

Fig. 3.1 Block diagram of CDF Level 1/Level 2 trigger system.

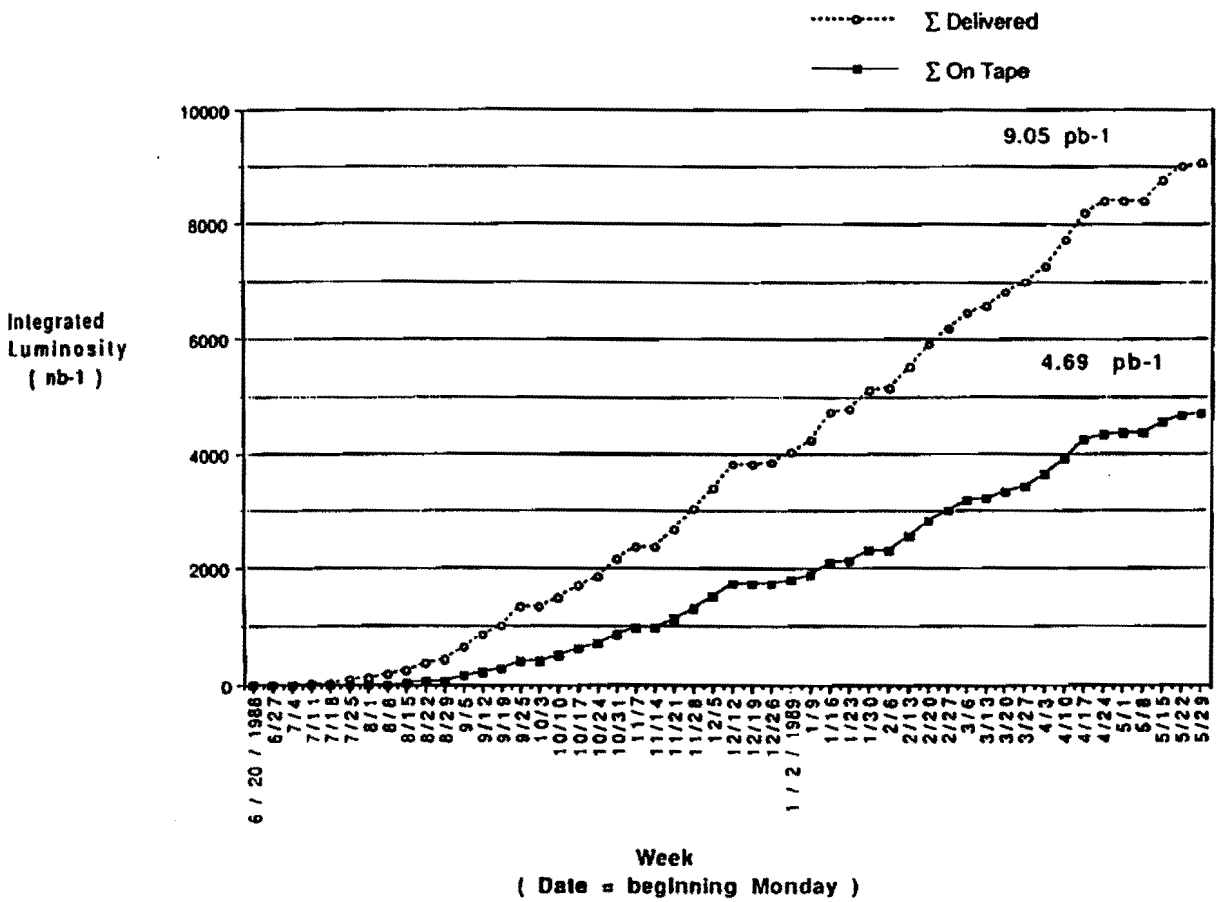

Fig. 3.2 Integrated luminosity vs. time for the CDF run 1988/1989

CHAPTER 4

Offline jet finding

For physics studies of jets an offline clustering is needed, more sophisticated of the online one used for triggering purposes. The variety of algorithms that can serve this purpose is virtually infinite. We will describe in this Chapter the algorithms which were studied by CDF and discuss the motivations for our choice of JETCLU.

4.1 Generalities on jet reconstruction

Several characteristics are common to all jet finding algorithms considered here. First of all, the search for jets is based on finding energy clusters in the calorimeter. There have been studies on whether jets could be found based on tracking information. However, this approach was found to be advantageous only for very weak jets (mini–jets), where the advantage of avoiding the spread of impact points on the calorimeter due to the magnetic field is substantial. Second, we used in clustering E_T rather than E, since the most interesting QCD processes involve large Q^2, i.e. jets of large transverse energy. Finally, the tower energy was defined as the sum of the energy depositions in the HAD and EM compartments. In principle there might be better ways of combining the two quantities, but we were unable to demonstrate any improvement in doing otherwise with CDF data.

The 4–momentum of a jet is evaluated from the tower cluster in the following way. The energy is taken to be the scalar sum of the energies of all towers, and the 3–momentum is calculated by summing the vectors pointing to the energy centroid of each tower (calculated from the phototube ratio), with magnitude equal to the tower energy. This is equivalent to assuming that each tower was hit by a single massless particle. It is worth underlining that this approximation is more accurate than it may appear at a first glance. Indeed, if we assume instead that the particle has the pion mass, the change in 3–momentum is smaller than 1% even for a tower energy of only 1 GeV. It is clear that the average contribution by particle masses to jet momenta is much smaller than this, and is negligible compared to any other systematic effect in our measurement. Of course a non–zero mass may also arise because energy is deposited in a tower by several particles, hitting on different points. However, even in the extreme case of the energy being concentrated in two equal lumps at the opposite ends of a tower, implying a mass of about 13% of their energy, the 3–momentum contributed by the tower would change by less than 1%[1]. In conclusion the zero mass approximation is very good and we do not need to worry

[1] A simple rule of thumb is $m \approx E\theta$ and $|p| \approx E(1-\theta^2/2)$, where θ is the half opening angle of the two energy lumps. Note that momentum is a much more stable quantity than mass.

about it.

4.2 Clustering algorithms in CDF

Four clustering algorithms have been developed and are available in the CDF analysis package. They are named CLUST2, CLUST3, CLUST4 and JETCLU. CLUST2 is a simple neighbor search, CLUST3 is a variable cone algorithm, CLUST4 is a refinement of CLUST2 (as explained below), and JETCLU is a fixed–cone algorithm. We describe them briefly in the following.

4.2.1 CLUST2

With this algorithm, there is no predetermined limit to the cluster size; contiguous towers are merged to a seed tower as long as they are above a minimum threshold and their energy keeps decreasing.

First, a seed tower list and a candidate tower list are formed. They are selected by requiring that they pass a given threshold in E_T, typically 1 GeV for the seed towers and 0.1 GeV for candidate towers. Then the highest E_T tower in the seed list is used to start a cluster, and the 8 nearest neighbor towers are examined and added to the seed if their E_T is not larger than a given factor (typically 2) times the seed tower E_T. The added towers are removed from the candidate list and the neighbor search is repeated for each of them, until the cluster stops growing. Then the process starts again with the following seed, until all seeds are used.

Finally, clusters are merged if they are nearer than 0.7 in the (η,ϕ) space.

4.2.2 CLUST3

This algorithm collects energy within a cone in the (η,ϕ) space whose size is a decreasing function of the cluster E_T. This is a natural procedure if one assumes that particles in jets have a constant average transverse momentum with respect to the jet axis. The radius is therefore $R(E_T) = \mathrm{Min}(C/E_T, R_{min})$; by default, R_{min} is 0.6 and C is 12.0 GeV. The algorithm begins by making a seed tower list and a candidate tower list like CLUST2, then picks up the highest E_T seed and adds all towers within $R(E_T)$. The new E_T is computed for the cluster and the procedure is iterated with the new $R(E_T)$, until the cluster remains stable. Then, as usual, the involved towers are removed from the list and the algorithms repeats with a new seed tower, until the seed list becomes empty.

4.2.3 CLUST4

CLUST4 is a more sophisticated version of CLUST2. After making the usual seed and

candidate tower lists, a first pass is performed using only the seed towers, starting as usual from the highest E_T seed. From the seed, a precluster is grown by adding neighboring seed towers having E_T smaller than the parent. The procedure is iterated until possible. When all seeds are used, a second phase begins using the preclusters as seeds. Each preclusters is allowed to include the adjacent candidate towers, and this is repeated again, adding an annulus to each precluster at each pass. If two clusters grow to touch each other, then the depth of the valley between them is tested: if the minimum is lower than a given fraction of the energy of the two clusters and of their peaks, they are kept separate, otherwise they are merged.

A final merging phase then occurs, to build full clusters from the preclusters. A list is made of all pairs of preclusters and ordered by increasing distance between its members. The top preclusters initiates a cluster, and the unmerged clusters are scanned and tested in this way: if the energy within a cone of 0.7 around the precluster being tested, and already assigned to the cluster, is larger than the energy of the precluster itself than the precluster is added to the jet. At the end, all preclusters assigned to more than one cluster are deassigned, the list of pairs is re–scanned and whenever a precluster is found coupled to a precluster assigned to some cluster, it is also assigned to the same cluster.

4.2.4 JETCLU

This algorithm uses a fixed cone radius to define jets (0.7 by default). JETCLU is the algorithm which is the most similar to the ones used in previous experiments.

In the preclustering stage, the candidate and seed lists are formed as described above. At this point, the gas calorimeter towers are grouped in bunches of three in φ, in order to have the same granularity as in the central calorimeters. Preclusters are formed as continuous chains of towers of decreasing E_T. Preclusters of E_T less than 2 GeV are dropped.

Then comes the clustering stage, in which the gas calorimetry towers are again considered one by one. The E_T weighted centroid of the preclusters is found, and a cone of the assigned radius is drawn around it. All candidate towers within this cone are assigned to the cluster. The centroid is recalculated, the axis of the cone is adjusted accordingly, and the list of assigned towers is updated. The procedure iterates until the cluster remains stable.

Finally comes the merging stage. If two clusters overlap, an overlap fraction is computed as the E_T of the common part divided by the E_T of the smaller cluster. If the overlap fraction is larger than 50% the two clusters are combined; if it is less than 50%, each tower in the overlap region is assigned to the nearest cluster. The centroids of the clusters are reevaluated and the overlap region is shared again until the stable point is reached.

4.3 Performance of clustering algorithms

The above list of algorithms gives an idea of the variety of clustering methods that can be devised, all reasonably good at finding jets. One must make a choice, based on some criteria. Several parameters can be devised to measure the performance of a clustering algorithm. Examples are the two–cluster separation, the amount of energy lost out of a cluster, the frequency of reconstructed anomalous clusters (like very large ones or with bad shapes or clusters embedded in another cluster, etc.), the accuracy in the assignment of the respective energies to pairs of closely spaced clusters, the efficiency in finding low energy or wide clusters, etc. Comparisons by visual scan of events have been performed, too.

In general, each algorithm performs better in a test and worse in another, so the best choice depends on what we strive for. Tab. 4.1 shows some results of the evaluation of the algorithms from ref. [13], where the algorithm parameters have been chosen in such a way to put them in the most similar conditions (cone and merging radii are 0.7, candidate tower thresholds are 0.1 GeV in all cases).

It is interesting to see whether the jet parameters are sensitive to the algorithm being used (see Tab. 4.2). It is reassuring that the differences are not large, so that we cannot expect a significant systematic effect due to the choice of a particular algorithm.

JETCLU was adopted in most CDF analyses. The main motivations are the stability of the reconstructed cluster energy in presence of nearby clusters and the sharp transition to a single (merged) cluster when two clusters get closer than a critical distance. It is also generally appreciated that JETCLU is simpler, faster, and more similar to the algorithms already used by other experiments, making the results easier to compare; also, it has no tendency to form pathological clusters, that other algorithms show to some degree.

We want to underline that our choice for JETCLU for the present analysis had a deeper motivation, in addition to the points listed above. As we shall discuss in the following chapters, we shifted from the usual point of view about the clustering algorithm. The standard point of view is that the algorithm should gather as a jet all particles coming from a primary parton[2]. This definition of jet,however, brings along the need for tuning the cluster energy/momentum scale to the primary parton energy/momentum with the help of some Montecarlo program (see Chapter 5). We rather define the jet in such a way as to have the algorithm reconstruct it exactly in the case of a "perfect" detector.The clustering algorithm becomes part of the jet definition itself,we therefore need to correct only for detector defects. In this approach, it is advantageous to have a simple definition of jet, like having a cone of fixed radius. The jet is defined as the bunch of particles emitted by the parton within the given cone. One day, it may become possible to compute theoretically the energy flow within the cone, and to make an accurate comparison with data.It could be more difficult to do the same with other algorithms. For example, it is hard to give a simple definition of a jet that corresponds to what CLUST4 is trying to reconstruct

[2] This assumes a fragmentation model where each parton hadronizes independently. It can only be an approximation, the decay of a colored particle into a colorless system being unphysical.

with its complicated neighbor search[3]. It does not seem likely that it will ever be possible to calculate theoretically something of such complexity.

To conclude this discussion on jet finding, we observe that comparisons between the clusters found by the Level 2 trigger and by JETCLU[14] have shown that very seldom a cluster found by JETCLU escapes detection or appears much smaller at Level 2. Therefore we can assume the trigger to introduce no inefficiency in our measurement, after excluding a limited turn–on region just above the trigger threshold.

[3] Note that the concept itself of neighbor is tied to the tower dimensions.

MEASURE	CLUST2	CLUST3	CLUST4	JETCLU
CPU/event (VAX 8650 sec)	0.075	0.093	0.141	0.063
Embedded clusters	3%	0%	0%	0%
Abnormally large clusters	1%	0%	0%	0%
Mean η width	0.73	0.82	0.78	0.95
Mean φ width	1.21	1.17	1.25	1.26
E_T lost to nearby clusters (GeV)	0.96	0.72	0.90	0.43
Merging distance	0.62	0.64	0.71	0.79
Merging sharpness	0.19	0.14	0.22	0.15
Merging distance (E_T >25GeV)	0.77	0.67	0.65	0.81
Merging sharpness (E_T >25GeV)	0.17	0.07	0.33	0.12
P_T resolution (GeV)	13.4	13.0	11.3	11.4

Tab 4.1 Performance of clustering algorithms in a number of tests (from ref. [13])

Comparison	ΔE_T(GeV)	ΔN_{towers}	$\Delta\eta$	$\Delta\varphi$
CLUST2–JETCLU	-0.16	0.46	0.0014	0.064
CLUST3–JETCLU	-0.32	0.08	0.0055	0.065
CLUST4–JETCLU	0.68	5.24	0.0088	0.064

Tab 4.2 Difference in cluster parameters evaluated by different algorithms (from ref. [13]).

CHAPTER 5

Corrections to jet energy and momentum

5.1 Evaluating the corrections

Due to various effects (non linearity of the calorimeter, leakage, loss in cracks, loss outside the cone, etc.), the jet 4–momentum as evaluated by the clustering algorithm is inevitably biased in some direction. No algorithm can be made so sophisticated to compensate for everything. In practice, nearly all detector effects amount to a loss of energy, therefore the measured momenta are always underestimated.

This is the motivation for making corrections to the jet 4–momenta. These corrections have the same effect as a calibration, that is adjusting the overall momentum scale without affecting the resolution. Actually, the detector is not perfectly uniform; therefore, if we make our corrections to depend on the jet position we will also compensate for part of the resolution deterioration. We have used a η–dependent correction because the detector characteristics change appreciably along η. This correction is a widely used tool in CDF for jet analysis, and is described in detail in ref. [15]. It is an extension of a previous work [16] that was limited to the central calorimetry and had no η–dependence. The nonuniformities in φ are less important and occur within distances smaller than the jet dimensions. In fact, no ϕ dependence can be seen in our data (see Chapter 6).

The above corrections are derived from simulation studies with ISAJET and QFL which allow to estimate the relationship between measured and true jet 4-momentum. It is important to clarify how the "true" jet 4–momentum was defined.

A problem was that ISAJET performs a pre–showering of the primary partons into partons of lower virtuality before fragmenting them into hadrons. This is necessary to reproduce correctly the number of jets observed in real events, since in ISAJET only QCD diagrams with more two outgoing partons are considered. For this reason, in ISAJET–generated events several jets are often produced by a single primary parton, each of them coming from one or more of the secondary partons generated in the pre–showering process. Therefore it is not possible to identify unambiguously the parent parton of each jet in order to compare its 4–momentum to the 4–momentum of the jet.

In earlier CDF works, the ambiguity due to the presence of multi-jet events was solved by rejecting events where a secondary parton was radiated at a η–ϕ distance larger than 1.0 from its

parent parton (only 1% of ISAJET–generated events survives this cut). After this selection, each parton is assigned all particles in its hemisphere, and the needed correction is evaluated by comparison with the calorimeter energy collected in that same hemisphere. An additional correction (based on actual CDF data) is introduced to account for the particles lost in the clustering process.

The scale correction currently applied in CDF jet studies was derived by turning off the parton pre-showering in ISAJET and letting the two primary partons to fragment directly into hadrons, so as to have always clean two–jet events. No initial state radiation or underlying event is simulated. Jets reconstructed after detector simulation are then associated to a parton if the cluster axis is within 0.4 in η–ϕ from the parton direction. In this way, it never happens that more than one cluster is assigned to the same parton (well separated extra clusters are occasionally found and rejected as fakes). In this scheme the reference momentum is simply the parton momentum[1].

We have applied this correction to our data. However, we shall re–scale everything according to our (still different) definition of "true jet momentum" during the unsmearing process (see Chapter 8). What we do is to define the "true" 4–momentum of the jet as the total 4–momentum actually contained within the jet cone at the vertex. This means we do not correct for the energy emitted outside the jet cone during the hadronization process, while we correct for all detector–related effects. Note that we *do* correct for the loss of particles due to bending by the magnetic field or to decays of real particles.

The motivation for doing this is the dependence of the standard correction on a particular hadronization model. We rather apply any needed model–dependent correction to the theoretical prediction when performing the comparison, and keep a purely experimental meaning for the data.

Nonetheless, we apply the standard correction at the beginning of our analysis for two reasons:

i) it corrects for the η–dependence of the detector response (while ours does not) and

ii) it leaves us with a smaller overall correction to do at unsmearing time, that makes our job easier.

Since we do apply this standard CDF jet correction to our data, we briefly recall in the following how this correction was derived. A number of limitations which are evident in this derivation shall be overcome by our final correction.

5.2 The Correction Function

[1] In practice the parton momentum must be calculated by adding the momenta of all generated daughter particles, because for ease of simulation the hadronization process is not forced to conserve 4–momentum.

The correction is expressed as a function of two variables: η and P_T of the jet. In principle it is possible to use E_T rather than P_T but P_T is probably better because it is balanced in each event. The earlier method corrected both P_T and E_T independently, but this is not appropriate at large η, where the jet mass would often be made negative by this procedure. Also, a separate correction would not conserve the jet rapidity. The correction we use re–scales the 4–momentum as a whole, of a quantity determined only by the measured P_T.

Since the effect of the underlying event was not simulated, it has been determined separately from the 1987 data, by looking at the momentum falling in a "ghost jet" cone at 90° in ϕ from the true jets. This effect is subtracted from the raw jet momentum.

The correction was derived from 200K simulated events, which were generated with a flat parton P_T distribution between 2 and 350 GeV. For every η and parton P_T bin, the average jet P_T was determined with a gaussian fit. This does not account for the effect of the long tails present in the simulated data, which are excluded from the fit. This is one of the reasons why we have developed the more accurate correction discussed in Chapter 8.

The relationship between cluster and parton P_T was fitted with a quadratic function, and the final result is a smooth interpolation of its three parameters as a function of η. The correction is finally expressed by these three functions of η. They are plotted in Fig. 5.1. The effect of the various transition regions between detectors shows up clearly.

It is interesting to note that a test has demonstrated that this correction, when applied to 1987 data, reduces to zero (within the statistical error) the P_T imbalance between jets in different detector regions. This supports our confidence that the simulation program reproduces faithfully the behavior of the detector.

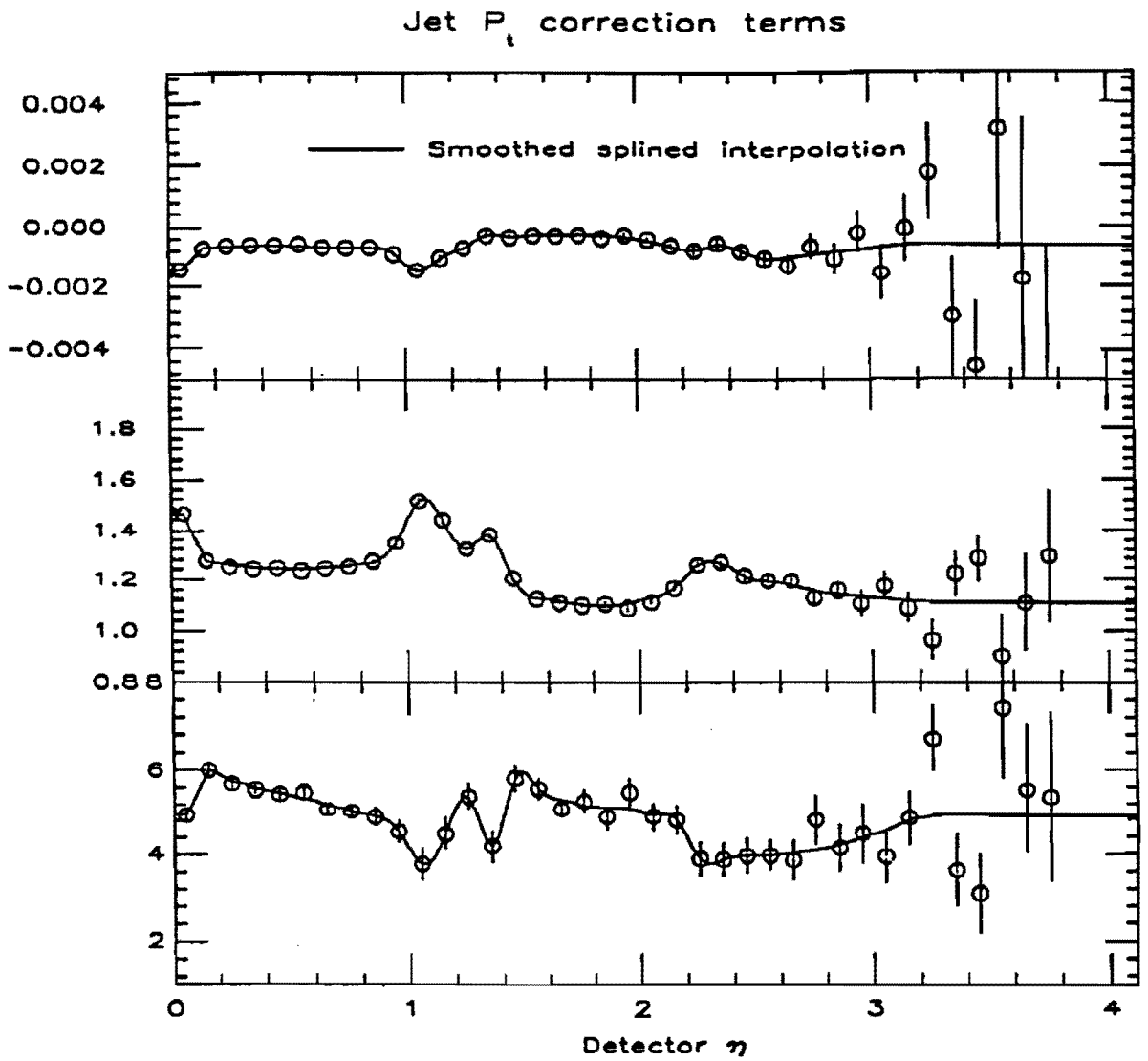

Fig. 5.1 From top to bottom: quadratic, linear, and constant term of the jet scale correction (from ref. [15])

CHAPTER 6

Tracking corrections

In the previous Chapter we described our scale correction to the jet 4–momentum. The detector effects responsible for this shift fluctuate from jet to jet, causing a spread of the measured values that cannot be compensated by means of an average correction. In this Chapter we discuss the possibility of improving the resolution by correcting for detector effects on a jet–by–jet basis.

Since the calorimetric information is already thoroughly exploited, the only possibility to improve the resolution lies in using extra information. The tracking system provides us with a great deal of potentially useful information. About 65% of jet energy is found in the charged component, it is therefore possible to think of methods for measuring jets by combining calorimetric and tracking information. We have chosen a less ambitious attitude, that is to use tracking as a tool for correcting for some calorimeter defects. We describe here a technique for correcting for the response nonlinearity and for the effect of uninstrumented regions in the calorimeter (cracks).

6.1 Monitoring the resolution

The first thing we need when trying to improve the resolution is a method for monitoring the improvement. We decided to base our work on real data, in order to be unquestionably sensitive to detector effects, that could in principle be partly unknown or incorrectly reproduced in the simulation.

With this approach we do not have a simulated value of the measured quantity, and we must find a way to estimate the resolution from the data. Actually, we do not need the absolute value of the resolution: it is sufficient to monitor any parameter whose value is mostly determined by the resolution.

We are interested in the resolution in invariant mass, which depends on the resolution in jet 4–momentum. It should be clear from the way it is calculated (Chapter 4), that the relative uncertainty on the magnitude of the momentum is larger than the relative uncertainty on the energy. In fact, it is easy to verify that the jet momentum, as we measure it, can be written as

$|P| = f*E$, where f is a factor ($0<f<1$) depending on the energy distribution among the cluster towers, which is affected by an additional uncertainty.

The relative importance of the jet momentum error versus jet energy error in the measurement of the dijet invariant mass is approximately $(1+\cos\phi)/2$. Therefore, when the jets are nearly back to back ($\phi \approx \pi$), the error on the energy is dominant. Unfortunately, we have no direct way to measure the energy resolution because at a hadronic collider the invariant mass of the colliding partons is not known. On the other hand, the transverse momentum of the initial state is approximately zero, so that the total P_T measured in the final state can be ascribed mostly to the experimental errors, and may be used for estimating the momentum resolution. This vector is opposite to the so called missing E_T vector. This name comes from the fact that it is calculated by adding vectorially the E_T of the calorimeter towers, as an approximation to the P_T carried by the final state particles.

The width of the distribution of the dijet $|P_T|$ gives an estimate of the resolution in jet P_T, and, for what we said above, an estimate (by excess) of the E_T resolution.

A detailed discussion of the topics examined in this Chapter can be found in [17].

6.2 P_T balance of jet events.

We use here some definitions similar to those adopted in ref. [18].

Let **K** be the total P_T of the dijet system, and K_η , K_ξ its components respectively in the direction of the bisector of the angle between the two jets and in the orthogonal direction (see the picture below). When the sign is relevant, we define the ξ versor so that $(P_1 \cdot \xi)>0$, and the η direction so that $\eta \times \xi = z$, where z is the positive direction along the beam axis. Note that our convention is different from what was done by UA2 [19], that defined K_η and K_ξ as the moduli of the **K** components.

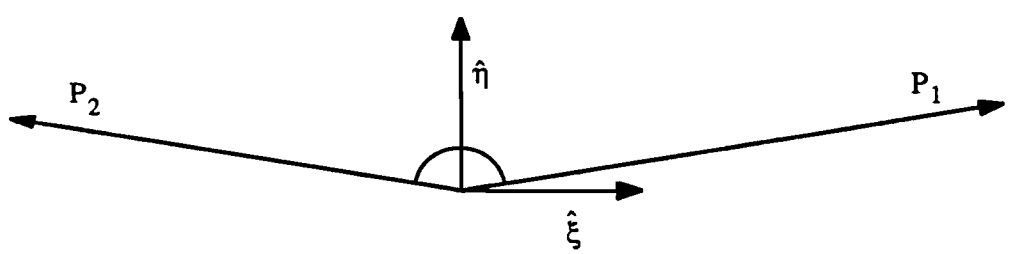

Let σ_ξ e σ_η be the standard deviations of the K_ξ and K_η distributions.

It is easily understood that σ_ξ is mostly determined by the finite resolution in the jet P_T measurement and by the intrinsic transverse momentum of the primary parton pair as contributed by primary and final state bremsstrahlung. Conversely, σ_η is sensitive to angular errors as well as to the intrinsic transverse momentum of the parton pair. Therefore, σ_ξ can help monitoring the detector resolution, while σ_η allows monitoring the amount σ_ξ which is of

physical origin.

We used in this work a sample of about 17K jet events from the 1987 CDF run, obtained with a trigger requiring at least 30 GeV of total E_T in the central calorimeter. Jet events are selected offline by requiring at least one jet above 30 GeV in E_T.

We applied the following cuts to this sample:

a) the main event vertex must be within 50 cm in z from the nominal interaction point;
b) all jets must be more than 0.1 in rapidity away from the 90° direction (η=0). This is to avoid a fake P_T imbalance due to a possible loss of energy in the 90° crack;
c) $|P_{T1}| + |P_{T2}| > 60$ GeV, to avoid a bias on **K** due to the 30 GeV cut on the leading jet;
d) the two leading jets must be in the central calorimeter;
e) The two leading jets must point at opposite φ hemispheres, i.e. they are back to back in φ within 90°.

Here the two leading jets are randomly assigned the labels 1 and 2, in order to make the K_ξ and K_η distribution have zero mean.

Fig. 6.1 shows plots of σ_ξ and σ_η vs. $\sqrt{(P_{T1}+ P_{T2})}$. Both r.m.s. widths decrease if we impose a cut on the third jet, and keep decreasing down to very low values of the cut (5 GeV), causing a substantial drop in statistics (see Tab 6.1). Moreover, σ_η is found not to be small with respect to σ_ξ. This means that the contribution to σ_η, and consequently to σ_ξ, of the energy emitted outside of the two leading jets is not negligible, and even tight cuts on the third jet cannot eliminate it completely.

Also errors on jet azimuth contribute to σ_η. To get an estimate of this effect, we plotted the difference between jet azimuth and the azimuth of the charged jet component. The standard deviation of this distribution is about 3°, and is determined by the errors of the two φ measurements. It must be pointed out the jet charged component is found to be well contained within the jet cone (see fig. 2), therefore the two φ measurements are uncorrelated. We can then assume that 3° is an upper limit for the error in the calorimetric measurement of φ. This means, for instance, that the angular error contributes less than $\approx$3.7 GeV to σ_η for jets of 50 GeV. At that energy, σ_η varies between 7÷12 GeV depending on the third jet cut. Therefore we can say that the contribution of physical effects is dominant, and we neglect the angular measurement error. The angular error would probably have to be taken into account if one was trying to estimate the absolute value of the resolution. This, however, is not our present concern.

Our goal is rather to reduce the contribution of physical effects to σ_ξ in order to increase its sensitivity to the resolution of the measurement. This would be easy if we could assume the radiation emission to be isotropic in φ. In this case we could subtract σ_η from σ_ξ in quadrature (neglecting the angular error) and use the result to monitor the resolution. Unfortunately, this is

not the case. In fact, most of the contribution to σ_η comes from the presence of a third jet, whose direction has a strong correlation with the direction of the two leading jets (see Chapter 10). Therefore, its contribution to the P_T imbalance is stronger in the ξ than in the η direction. Conversely, part of the energy radiated along the ξ direction is likely to be included in one of the leading jet cones. This has the effect of making the contribution to σ_ξ smaller than that to σ_η. Our conclusion is that the most fruitful approach is to use a procedure which minimizes σ_η and use the corresponding σ_ξ without any subtraction as our resolution estimator.

One way to do this would be to cut very tightly on secondary jets. As already mentioned, this would cause a severe loss in statistics. We chose instead to include the contribution of the secondary jets in the evaluation of the P_T imbalance.

There is no problem in including additional jets in the calculation of **K**. One only needs to redefine the ξ , η directions. We could use the "thrust" of the jet system or another similar quantity, but we prefer the following algorithm, which has the advantage of reducing to the usual definition when only two jets are present:

a) assign the labels 1 and 2 in the usual way;
b) take the transverse momentum P_n of the next jet (according to E_T) and evaluate $(P_n \cdot P_1)$ and $(P_n \cdot P_2)$;
c) redefine the momentum of the leading jet having the larger dot product with P_n by adding P_n to it;
d) repeat from b) unless no more jets are present or the required maximum number of jets is reached.

This procedure yields two vectors P_1 and P_2 that are used to define ξ and η .

Tab. 6.2 shows the decrease of σ_η , σ_ξ when more jets, up to a maximum of five, are added in. It is also interesting to look at the correlation between **K** as calculated with n jets and the direction of jet n+1. Fig. 3 shows the azimuthal difference between those vectors. There is an obvious correlation for n=3 , that decreases with n, but is still present for n=5.

The use of secondary jets in the imbalance calculation poses the problem of what is the jet momentum at which we are measuring the resolution. When using only the two leading jets, we can simply take their average momentum as the reference value, because the momenta are not very different. Now we have instead several jets of different energies, and there is no obvious answer to the above question. Nevertheless, if we assume that the error on the momentum of a single jet grows as $\sigma = \alpha\sqrt{P}$ where α is some constant, one can easily show that the contribution of the detector resolution to σ_ξ is :

$$\sigma_\xi(\text{detector}) = \alpha\sqrt{\sum_1^N P_n \cos^2\phi_n \sin^2\theta_n}$$

where the sum runs on all n jets included in **K**. θ_n are the polar angles and ϕ_n the azimuthal angles relative to ξ. We will call "equivalent momentum" (P_{eq}) of the multijet system the quantity under the square root. Then, we can say that all events with the same P_{eq} have a σ_ξ corresponding to the resolution for a single jet of momentum P_{eq}. Fig. 6.4 shows a plot of σ_ξ/P_{eq} vs. $1/\sqrt{P_{eq}}$, calculated with six jets. The points lie approximately on a straight line, thus confirming the assumption made in defining P_{eq}[1].

6.3 Correction for non–linearity

What follows is a description of the algorithm that was implemented to correct for the non linear calorimeter response and for the effect of the magnetic field. A detailed report can be found in ref. [17].

After imposing some quality cuts on the tracks, for each jet we make a list of all tracks within its cone, and a separate list of all tracks hitting the calorimeter within the jet cone boundary.

For each track associated to a jet both at the vertex and at the calorimeter, the difference between the track momentum and the expected (non linear) response (as measured in ref. [20]) is evaluated. This difference is the quantity to be added to the jet 4–momentum. If a track is inside the cone at the vertex but exits the cone before reaching the calorimeter surface because of the magnetic field, the whole particle momentum must be added to the jet. Conversely, tracks hitting the calorimeter within the jet cone which are outside of the cone at the vertex do not belong to the jet and their momenta must be subtracted.

For each jet, all contributions are added together to give on overall correction P_{corr}. This correction is not simply added to the jet 4–momentum. This is because the CTC η–acceptance is limited, and for jets extending beyond the CTC acceptance there is a risk of biasing the jet rapidity. On the other hand, we would like not to limit the correction to jets completely contained in the region of full tracking efficiency, but rather to have the correction turning itself off with no abrupt jumps when the tracking information is gradually lost.

Therefore, we apply the correction in such a way as to keep the jet η constant. Prior to applying a correction, we project it onto the plane containing the jet axis and perpendicular to the plane defined by the beam and the jet itself. This procedure is such that corrections can only

[1] Note that one can define P_{eq} with respect to a direction other than ξ, for instance with respect to η. In principle the same formula still holds and α is unchanged. However, one expects an additional contribution from angular errors. For this reason we believe that the ξ direction is the best choice.

change the jet azimuthal and not the jet polar angle[2]. Optionally, one can require also ϕ to remain constant, by projecting the correction onto the jet axis.

We have tested the effect of this correction by looking at σ_ξ vs. $\sqrt{P_{eq}}$ and comparing to what is obtained when only the average correction described in the preceding Chapter is applied. Since the tracking correction does not correct for all effects taken into account by the global correction, the P_{eq} of an event in the two cases would be different. For this reason, in order to make a comparison it is necessary to equalize the energy scales in the two cases. To accomplish this, we evaluated the average residual correction after the tracking correction, and applied it to the tracking–corrected data.

It is interesting to note that the average effect of the tracking correction amounts approximately to a momentum independent factor of ≈ 1.2, in agreement with the estimated average effect of the non–linearity found in simulation studies [15,16].

The comparison is shown in fig. 6.5, and shows a small but consistent decrease of σ_ξ when the tracking correction is applied. Note that the statistical errors in the two plots are correlated because they refer to the same event sample. Therefore, the statistical significance of the resolution improvement is stronger of what may appear by looking at the two sets of errors bars in this plot.

In conclusion, we can state that the observed decrease sets a lower limit of $\approx 10\%$ to the resolution improvement obtained with the procedure described. This is a conservative estimate because σ_ξ is determined in part – as discussed before – by effects which are not measurement errors

6.4 Correction for crack losses[21,22]

As mentioned in Chapter 2, two kinds of cracks are present in the central CDF calorimeter. The vertical gap between the two barrels (at $\theta=90°$), and the 24 azimuthal interfaces between calorimeteric wedges, which are equally spaced in φ and run across the whole length of the central calorimeter. The 90° crack is about 20 cm wide and its effect can be clearly seen in the pseudorapidity distribution of the leading jet, which shows a clear dip at $\eta=0$ (see fig. 6.6). This problem is often bypassed in CDF analysis by rejecting events with jets pointing too close to the crack. We have not made an effort to correct for this with the help of tracking. The φ–cracks are narrower and their distance from each other is much smaller than the jet cone size. Their influence in the measurement is less dramatic than the 90° crack. On the other hand, all jets are involved with φ–cracks. We therefore devoted some effort to developing a jet–by–jet correction for the effect of these cracks. For the above reasons, it is not surprising that no correlation between the jet axis distance in φ from a crack and its energy can be put in evidence

[2] This does not keep η exactly constant, but the difference is negligible if the correction vector is not large compared to the original jet momentum. This is always valid in our case.

in the data. This test was performed on the same sample of events from the 1987 run used in the previously discussed analysis.

We randomly labeled the two leading jets as "probe" and "reference", and studied the distribution of $\Delta E_T = E_T^{probe} - E_T^{reference}$ for different positions of the probe jet centroid within a φ wedge. Four regions are defined within each wedge, as in the diagram below

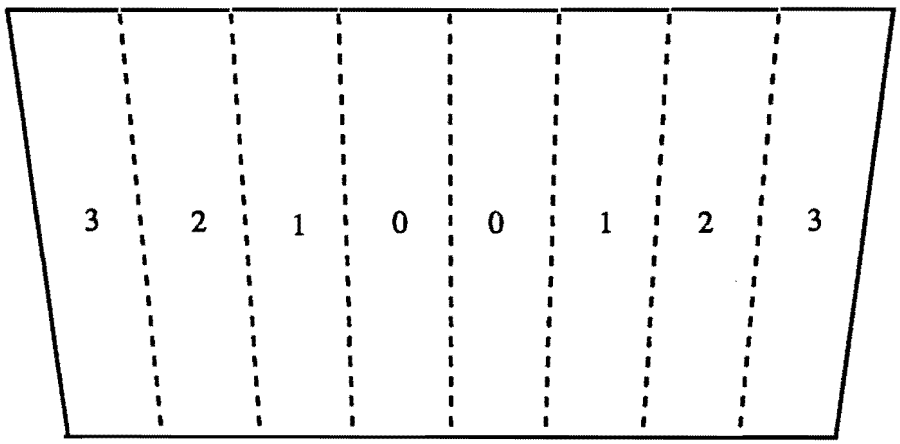

The four corresponding plots are shown in Fig. 6.7. No significant position dependence is seen[3] . The change in shape of the distribution is not relevant to this analysis, and is discussed in ref. [21].

In turn, we can estimate the amount of energy going into φ–cracks in a particular jet with the help of tracking. For each jet, we call E_{crack} the scalar sum of the momenta of all its associated tracks pointing to within $\pm 1°$ from the cracks. Tracks having a momentum smaller than 1 GeV are not considered, because their angle of incidence on the calorimeter essentially allows them to skip the crack. Then we assign the label "1" to the jet with the smaller E_{crack}, and the label "2" to the other. If the energy pointing to the cracks is subject to losses, then jet 2 gets a larger effect than jet 1, and one should observe an average shift of K_ξ towards positive values (the ξ versor lies in the jet 1 emisphere). On the other hand, we must not miss the fact that by selecting the jet with the larger E_{crack} we introduce a bias on its energy. A jet with more energy will also have, on the average, more charged energy pointing to cracks. This has the opposite effect of pushing the average K_ξ towards negative values. To account for this, we have repeated the same plot with respect to fictitious cracks placed at positions of full calorimeter efficiency. Fig. 6.8 shows a plot of the average K_ξ as a function of $E^1_{crack} - E^2_{crack}$ for the real cracks compared to the

[3] The criticism could be made that the kinematic correlations (back to back) between the two jets could cause the reference jet to fall in the same region as the probe jet. It has been verified by looking at the scatter plot of φ_1 vs. φ_2 that this is not the case, since the correlation is much wider than the width of these regions.

average values obtained from three control regions (at 1/4, 1/2, and 3/4 of the tower width). The difference between the two plots is plotted in fig. 9, and indicates that a fraction of 20÷25% of the charged energy seen as pointing to cracks is indeed lost.

This result can be used to perform a correction by adding to each jet the estimated amount of lost energy. Nevertheless, we could not demonstrate any resolution improvement following the application of this correction. We attribute this to the fact that the average energy loss of particles hitting cracks is subject to wide fluctuations[10] that are likely to wash out the effect of the correction, as far as resolution is concerned. Therefore, we also tried the approach of rejecting events with jets having a large E_{crack}, that have a high probability of being mismeasured. Fig. 6.10 shows the σ_ξ of the sample passing a tight cut of 5 GeV on E_{crack} compared with the original sample. The plot obtained by using the "fake cracks" at the tower centers is also shown. An improvement is clearly seen, that is not reproduced in the control sample. As expected, the correction has little effect on low energy jets, due to their low content in particles with P_T>1GeV. Fig. 11 shows the fraction of events surviving the cut as a function of the threshold value. We can see that our cut requires some sacrifice in statistics, that can be as large as 30% when the E_{crack} cut is as tight as 5 GeV, as in the plot of fig. 6.10.

6.5 Correction summary

We have seen that a resolution improvement can be obtained with the help of tracking information. The correction for low–momentum tracks and the cut on energy pointing to cracks are uncorrelated, and a larger improvement (12÷15%) is obtained when both are applied (see fig. 6.12). These correction algorithms can help when searching for bumps in the mass spectrum, as, for example, in the case of the hadronic decay of the W,Z bosons. They also reduce the systematic error due to the uncertainty in the jet fragmentation, which enters in determining the correction to be applied to account for non–linear response. In addition, the tracking–based non–linearity correction was used in CDF for the analysis of jet fragmentation in 1987 data, to cancel the bias on the momentum of jets undergoing a soft fragmentation, that would otherwise distort the shape of the fragmentation function [23].

Nevertheless, we decided to postpone the use of the tracking correction in the analysis of the dijet cross section to a later stage , for the following reasons:

i) the present analysis is mainly concerned with putting into evidence possible deviations from the predicted QCD cross section over ranges much wider that the resolution;

ii) the full tracked data from the 1988/89 run was not available when most of the analysis work for this thesis was performed (it actually became available at the beginning of 1990);

iii) the study that could gain the most from a resolution improvement, namely the study of the W/Z bump, could not be performed with data of the 1989 run. Our data sample has a

minimum jet E_T threshold of 20 GeV, that, after offline corrections and allowing for the trigger turn–on, puts the lower edge of our dijet spectrum at ≈80GeV, that is midway of the W/Z bump;

iv) the evaluation of the systematic error when tracking corrections are used, relies on the reliability of the Montecarlo simulation of the tracking detectors. As of today, this has not yet been studied as thoroughly as the calorimeter simulation.

	Maximum E_T of jet 3			
	∞	20	15	5
σ_η	12.9	11.3	9.6	6
σ_ξ	14.1	13.3	12.8	11
# events	2082	1831	1283	220

Tab. 6.1 Effect of a third jet cut on the width of the **K** components

	2 jets	3 jets	4 jets	5 jets
σ_η	12.9	8.3	7.4	7.3
σ_ξ	14.1	12.4	11.9	11.5

Tab. 6.2 Width of the **K** components, evaluated by adding in a different number of jets

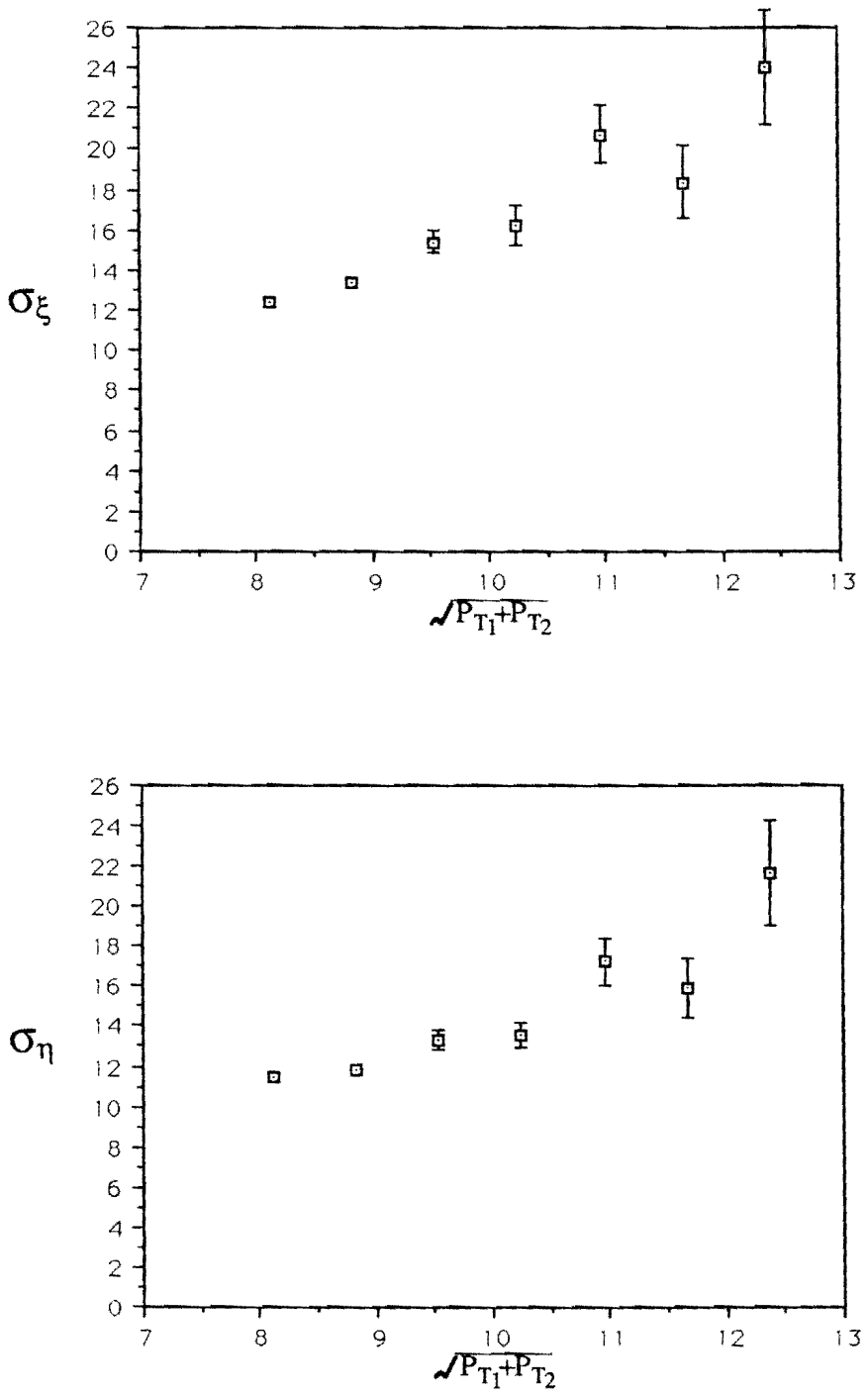

Fig 6.1 Standard deviation of the K_ξ and K_η distributions.

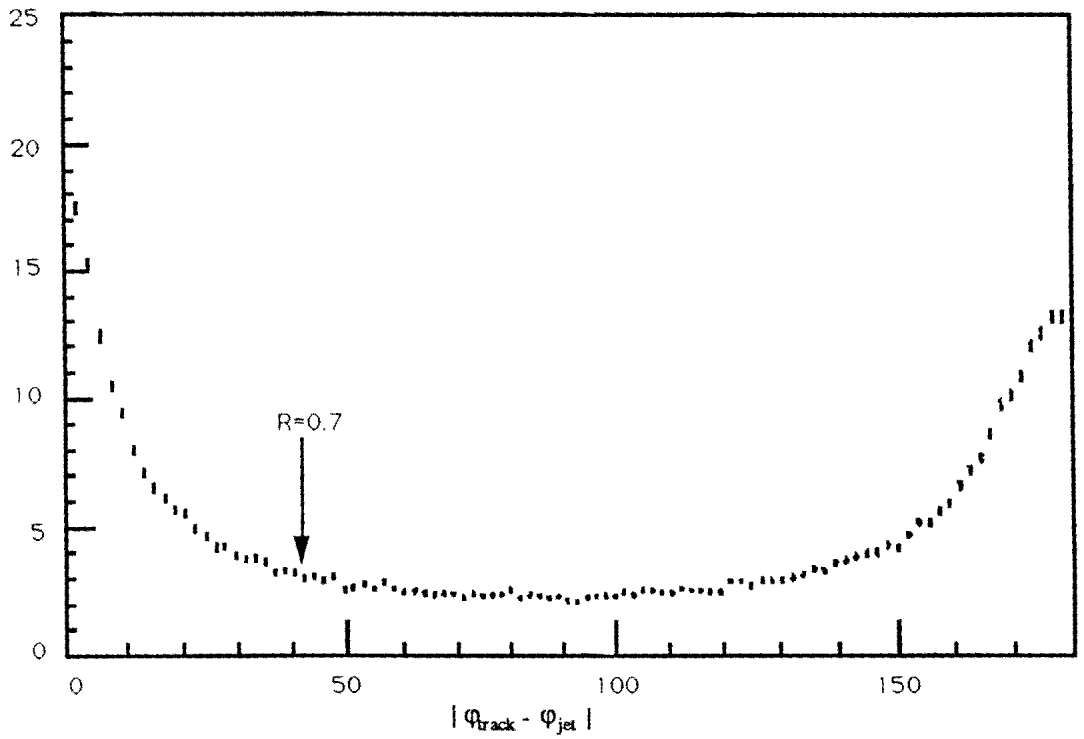

Fig 6.2 Distribution of tracks in φ around the jet axis.

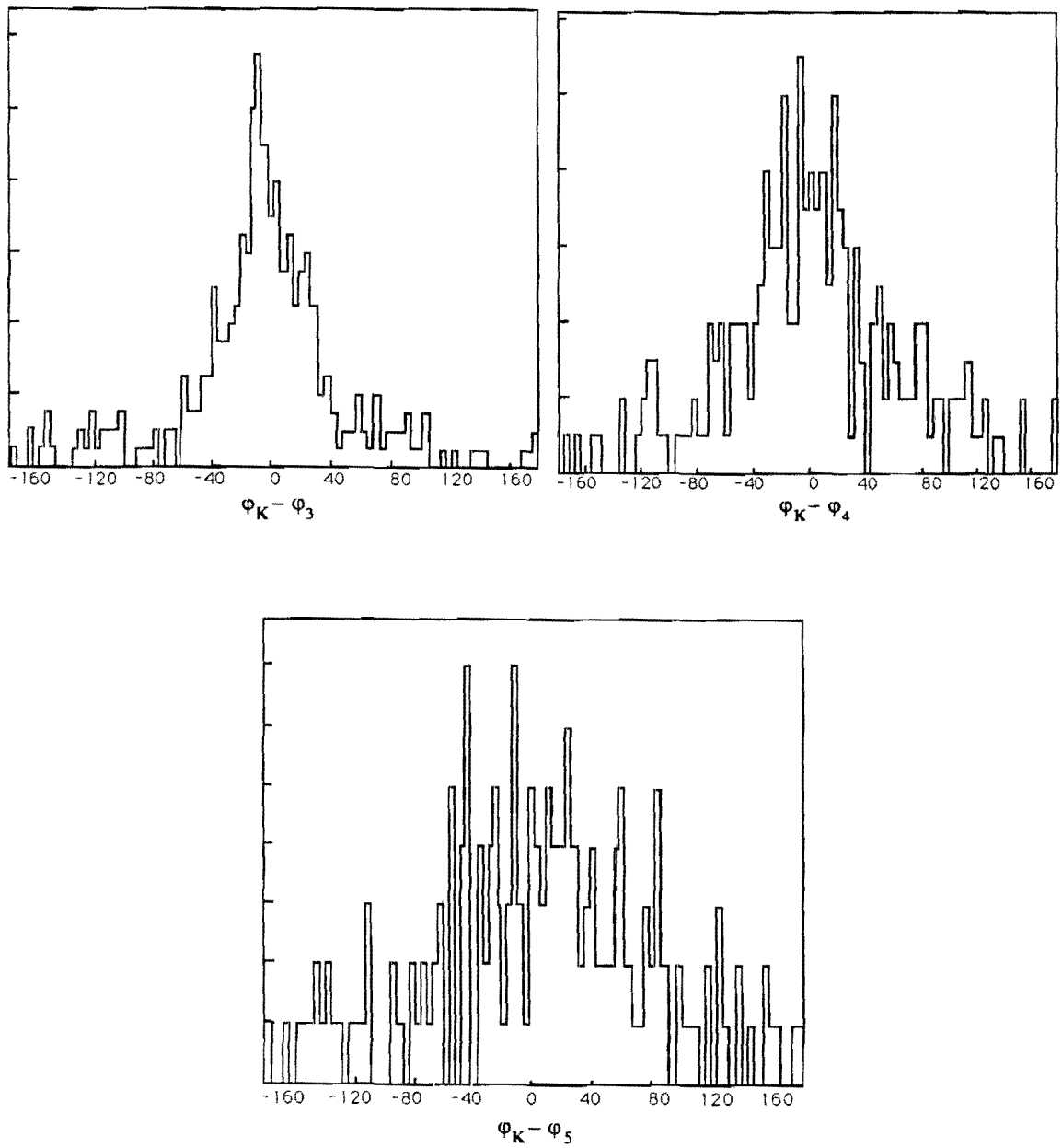

Fig 6.3 Correlation of the missing E_T of the leading n jets with the direction of the $(n+1)^{th}$ jet

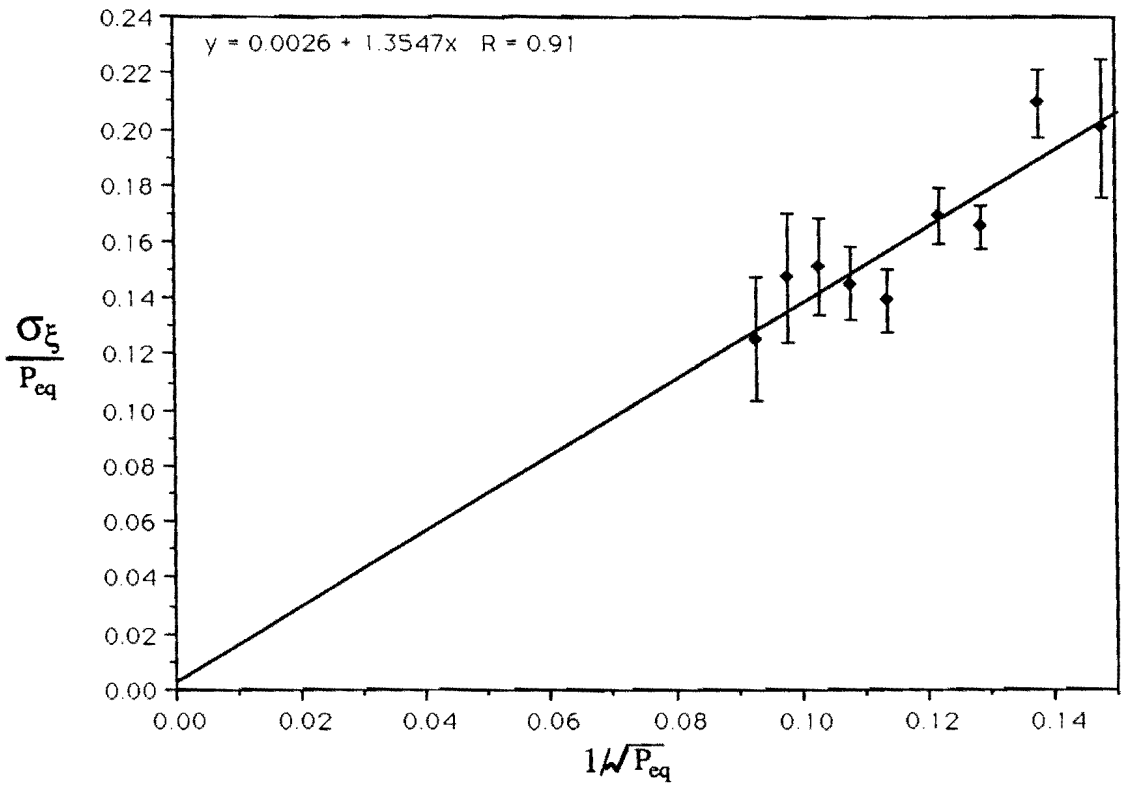

Fig 6.4 σ_ξ/P_{eq} vs. $1/\sqrt{P_{eq}}$ evaluated with six jets, with a linear fit

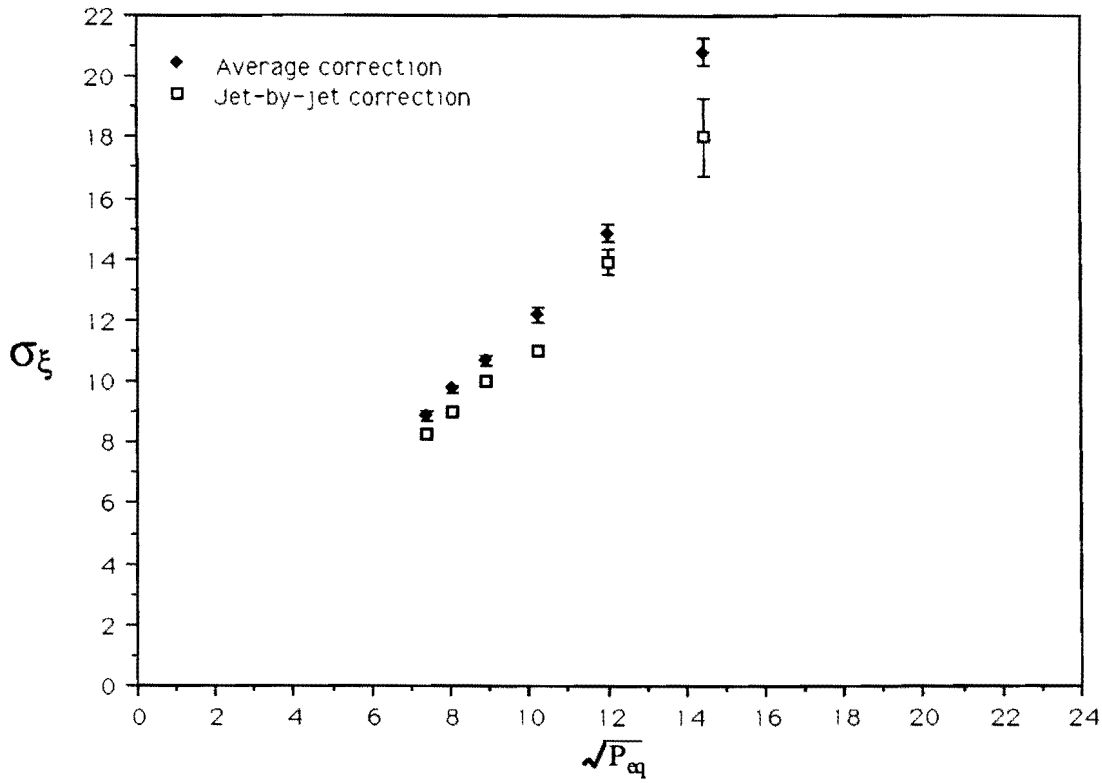

Fig. 6.5 Resolution improved by correcting for calorimeter non–linearity on a jet–by–jet basis

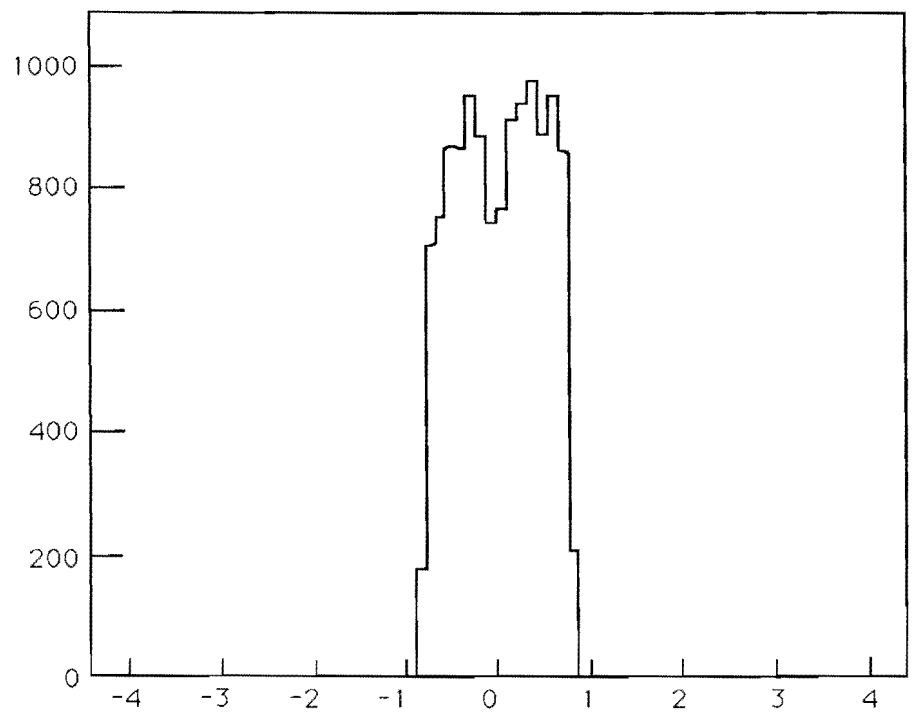

Fig 6.6 $\eta_{detector}$ distribution of the leading E_T jet.

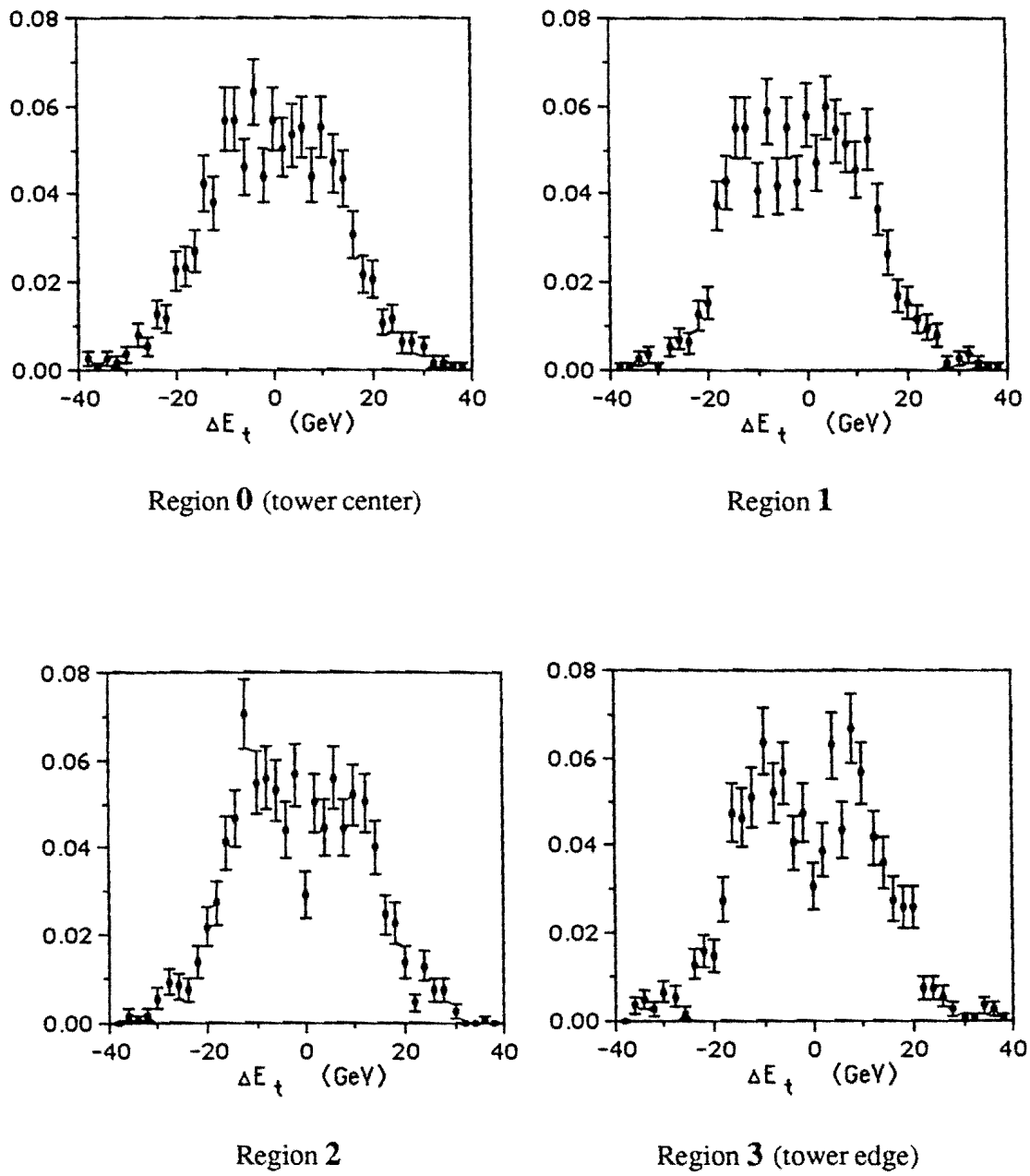

Region **0** (tower center)

Region **1**

Region **2**

Region **3** (tower edge)

Fig. 6.7 Energy difference distribution for different tower regions.

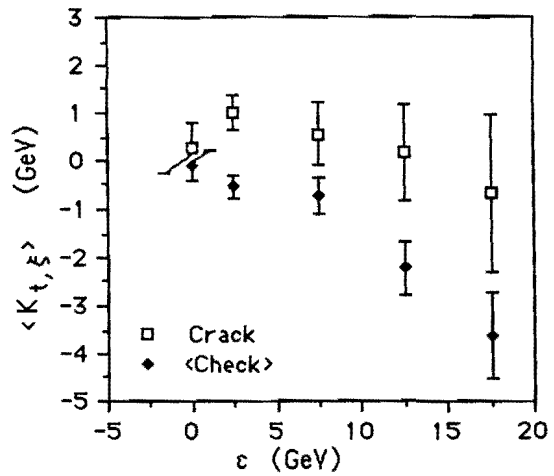

Fig. 6.8 Average momentum imbalance vs. difference of charged momentum pointing to cracks (check) regions.

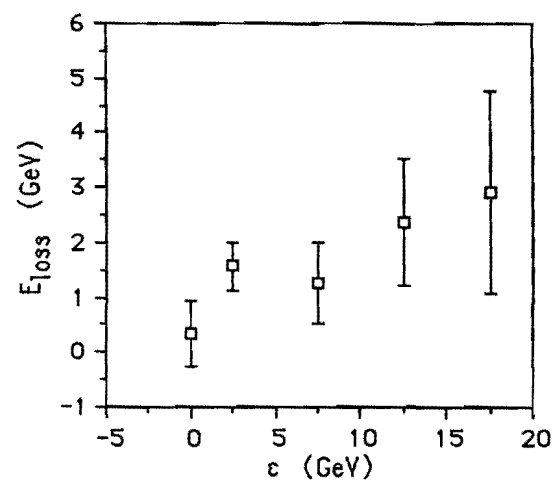

Fig. 6.9 Average energy loss for tracks pointing to φ–cracks.

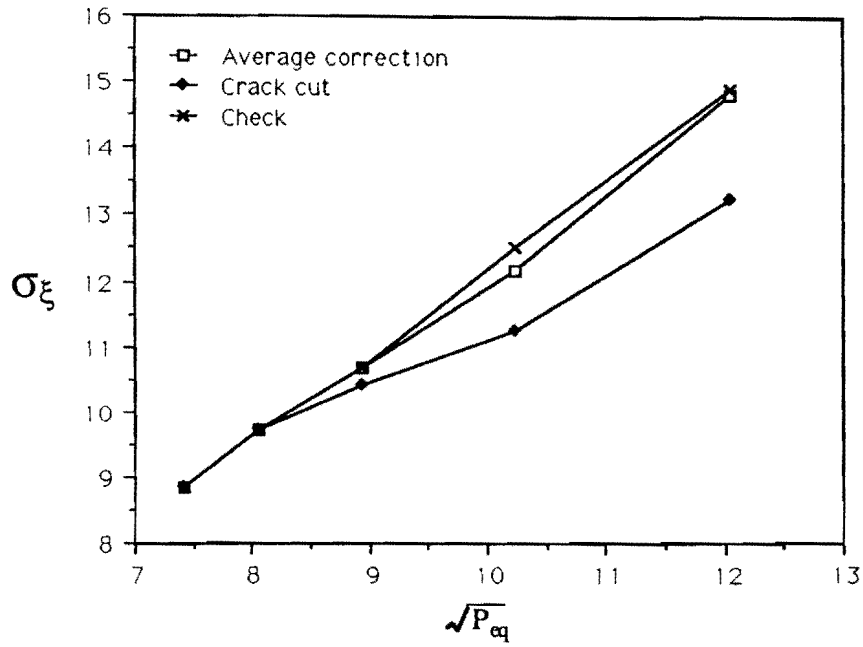

Fig 6.10 Effect on σ_ξ of a 5 GeV cut on the charged energy pointing to cracks

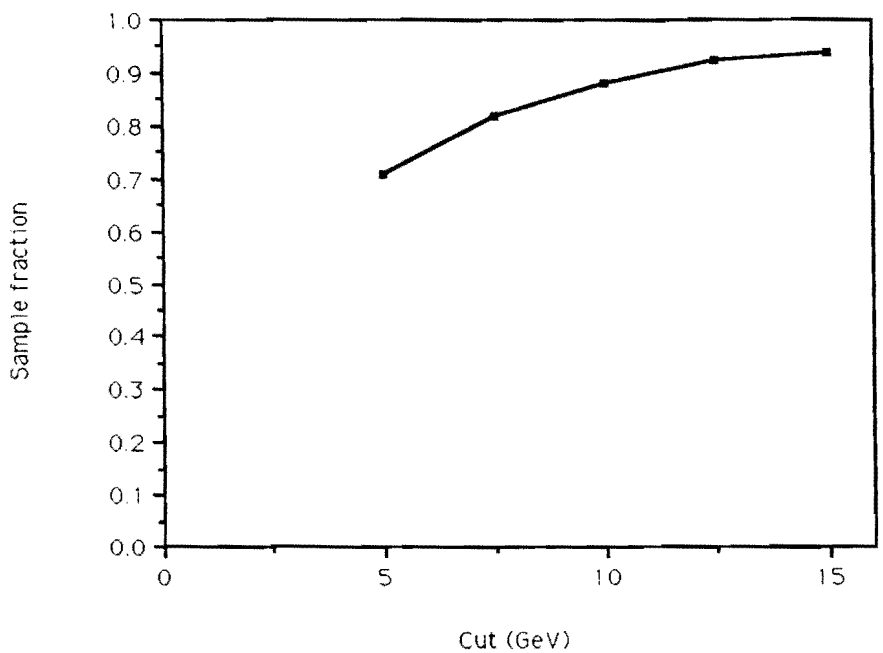

Fig 6.11 Fraction of events passing a cut on the charged energy pointing to cracks

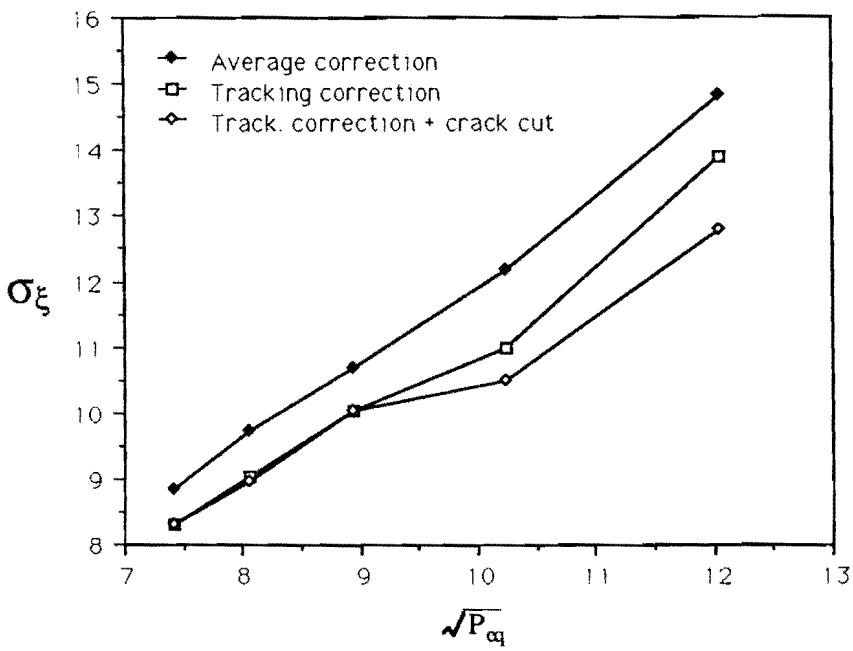

Fig 6.12 Combined effect of tracking correction and crack cut

CHAPTER 7

Event selection

In the following we describe in some detail the cuts applied to the data .

7.1 Offline cuts

a) Clustering was performed with the JETCLU algorithm (see Chapter 4) with the following parameters:

– candidate tower threshold: 0.2 GeV;
– seed tower threshold: 1 GeV;
– cone radius 0.7.

b) $|Z_{vertex}| < 60$ cm.

The primary interaction vertex was required to be within 60 cm of the geometrical center of the detector in the beam direction. This is a standard fiducial cut applied in most of the CDF analysis streams. Particles from an off–center event would hit the calorimeter at an angle with respect to the projective tower axis. This could introduce systematic deviations in the calorimeter response. Moreover, as the consequence of this cut our kinematical region of acceptance, when translated into the lab system, remains inside the central calorimetry region, that we understand best. Actually, we have studied the rejected data to see if any anomaly shows up, and we found nothing. Nonetheless, we kept the cut to be safe.

The acceptance of this cut has been measured on "minimum bias" data, and turned out to be 94.3%. We have corrected the cross section accordingly (see after). Lately this acceptance has been calculated [24] also on several different selections of jet data and was found to be reproducibly in the range 94÷95%.

c) $|\Delta\varphi| < 20°$.

The two leading jets are required to be back to back within 20° in the transverse plane. Fig. 7.1 shows the original distribution of $\Delta\varphi$ and the position of the cut. This cut is part of our experimental definition of two–jet events. It is intended to reject events with a too striking multi–jet topology, like for instance the so called "Mercedes events", having 3 jets of similar energy at about 120° to each other. Other cuts could have been used to obtain the same effect,

like cutting on the energy of the third jet or on the fraction of the total energy carried by the two leading jets, etc. The cut on $\Delta\varphi$ was preferred because it is related only to the two leading jets, and is therefore insensitive to possible problems in the measurement of additional non–leading jets (involving the whole CDF calorimetry) and to noise spikes. However, the value of the cut is arbitrary (even if we may judge it to be reasonable). If it will become possible in the future to introduce this cut explicitly in the theoretical calculation, the cut will be regarded as a parameter of the measurement. The cut on $\Delta\varphi$ is probably easier to use for this purpose than the other cuts mentioned above.

We will further discuss the effect of this cut in Chapter 11.

d) $|Y_{boost}| < 0.4$, $|Y^*| < 0.4$.

$Y_{boost} = (Y_1+Y_2)/2$ is the rapidity of the center of mass of the two leading jets and $Y^* = (Y_1 - Y_2) / 2$ is the rapidity of jet 1 in the center of mass frame. This is the kinematical region we have chosen to integrate the cross section over. It is a simple square region in the (Y^*, Y_{boost}) space around the 90° emission. This cut is narrow enough to ensure that both jets are measured in the central calorimeter, giving us a more homogeneous response.

The invariant mass was calculated as $M_{jj} = [(E_1+E_2)^2 - (\mathbf{P}_1+\mathbf{P}_2)^2]^{1/2}$, where E_i and P_i are the measured energies and momenta of the two leading jets. Our data consists of four separate samples, two from JET_20 and JET_40 triggers, and two from the JET_60 trigger. Of the latter two, one is the $\approx$850 nb^{-1} sample that had been pre–processed from the raw data tapes by the standard CDF offline programs at the time of the present analysis. The other sample was extracted from the full 4.65 pb^{-1} of raw JET_60 data by requiring at least one jet with E_T>100 GeV. We will call this sample JET_100 because it can be looked at as an "offline trigger". In this way we can use the full statistic of the run in the high mass region.

We obtain the distributions dN/dM_{jj} independently for the four samples and we correct them separately for the luminosity and the prescale factor. We use the overlap regions of the different spectra to decide where to put the mass cut in order to avoid the trigger bias (fig. 7.2). The cut is set at 77, 140, 196 and 273 GeV respectively for JET_20, JET_40, JET_60 and JET_100. Then we join the four spectra in a single distribution and we apply the correction for the acceptance of the z cut to obtain the $d\sigma/dM_{jj}$ (nb/GeV). Fig. 7.3 shows the resulting plot of the differential cross section $d\sigma/dM_{jj}$ as a function of the dijet invariant mass M_{jj}, which extends over 6 orders of magnitude. It still needs to be corrected for the finite detector resolution (see next Chapter) and rebinned in the high mass region.

7.2 Cosmic Background

We have checked the residual contamination of cosmic rays in our data by using the CENJET program [25,26] that identifies offline cosmic rays with an elaborate algorithm. Even a small amount of background can be dangerous if it contaminates mostly the large mass region, where the cross section is very small. It could simulate an excess of rate over the QCD predictions of the type predicted by new physics processes.

We have studied the mass distribution of events recognized by CENJET as cosmic rays. The distribution is shown in Fig. 4. All events have a very low mass and their contribution to our spectrum is completely negligible. Actually, a number of events have a very energetic jet, that makes them potentially dangerous for the inclusive single jet E_T distribution; but the imbalance with the other jet causes the mass of the two–jet system to be low.

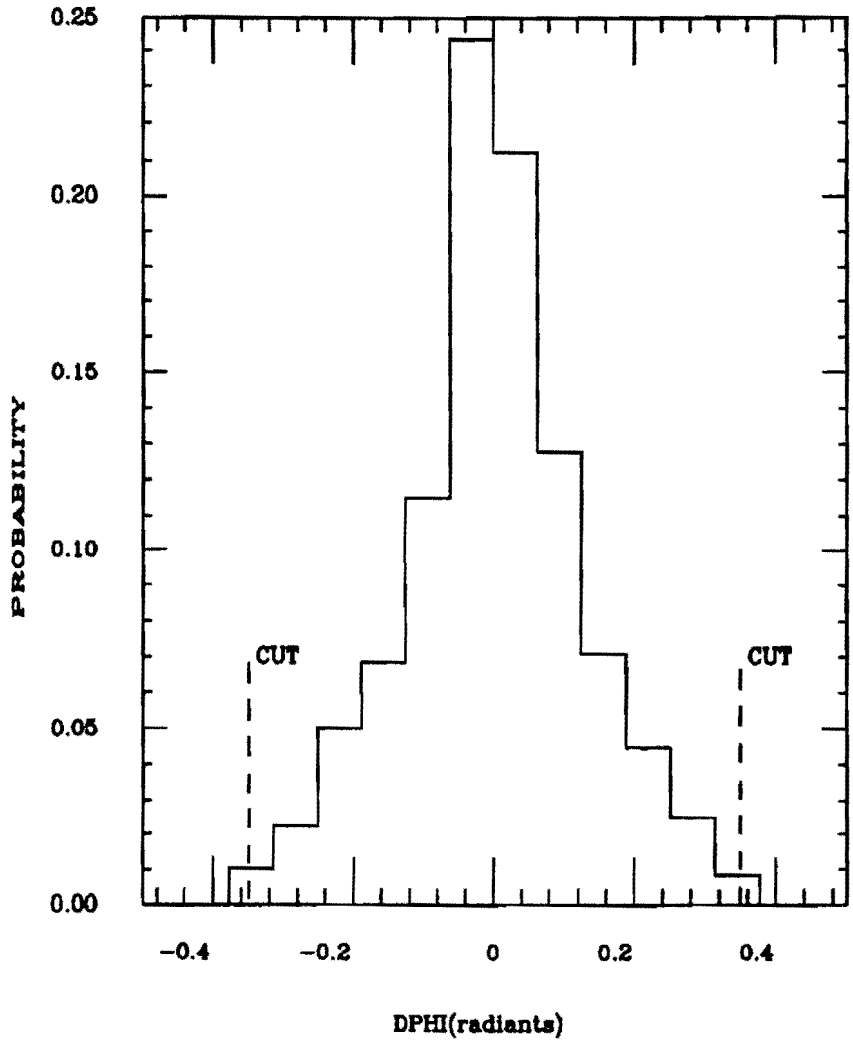

Fig. 7.1 $\Delta\varphi$ distribution of high mass events (M_{jj} >225 GeV).

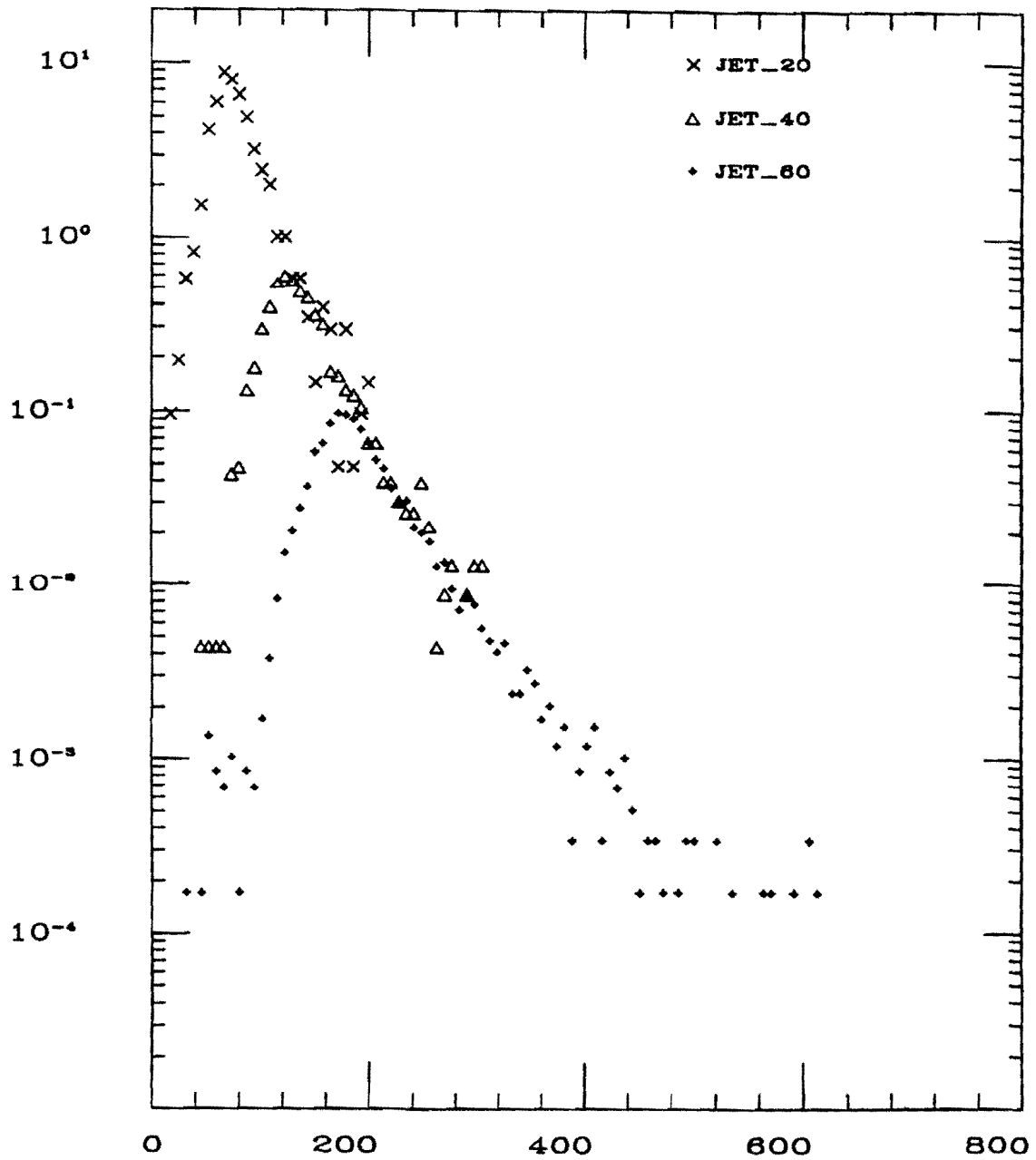

Fig. 7.2 Overlap of M_{jj} distributions from different triggers.

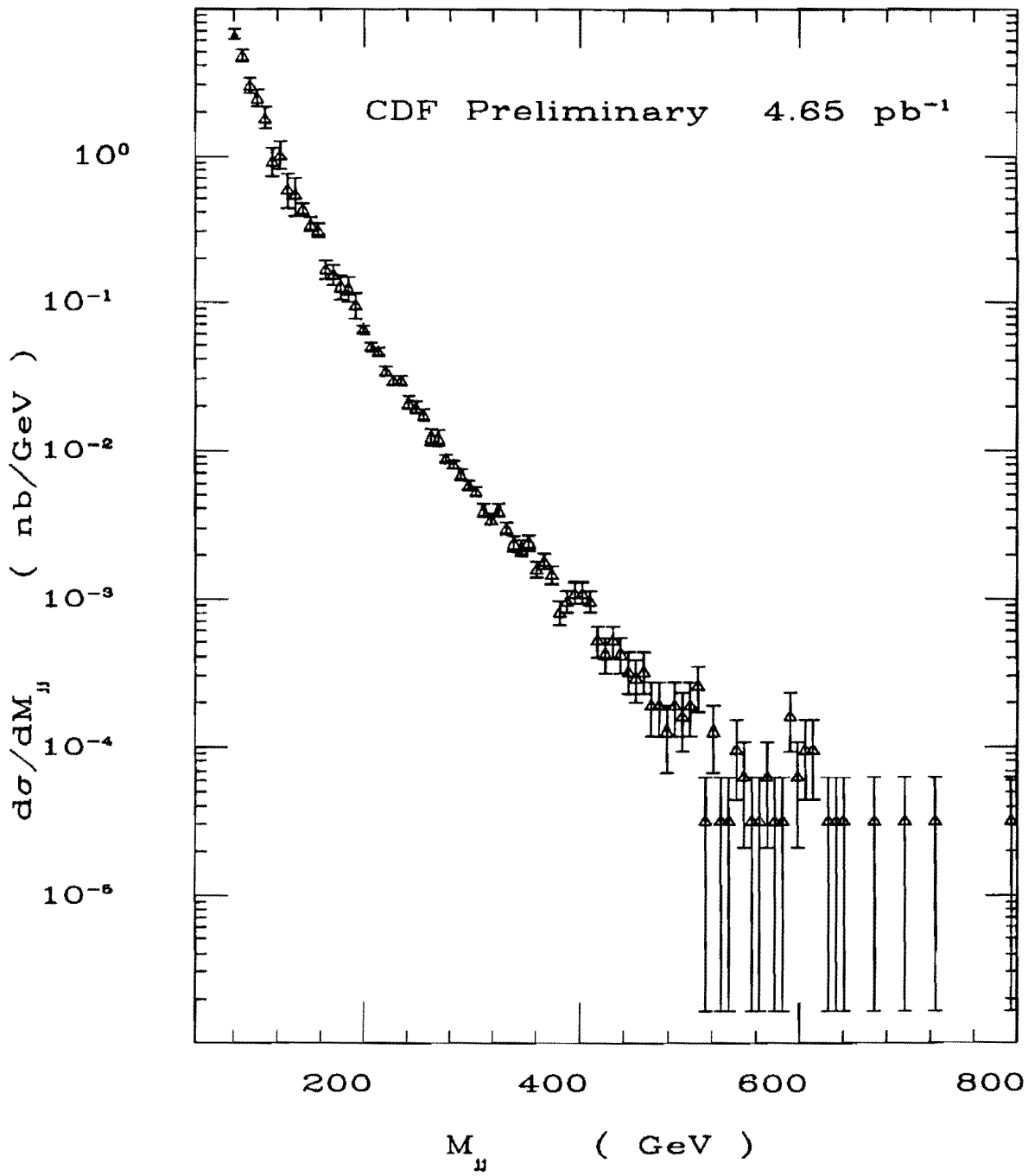

Fig. 7.3 Raw M_{jj} distribution. Detector resolution is not corrected for.

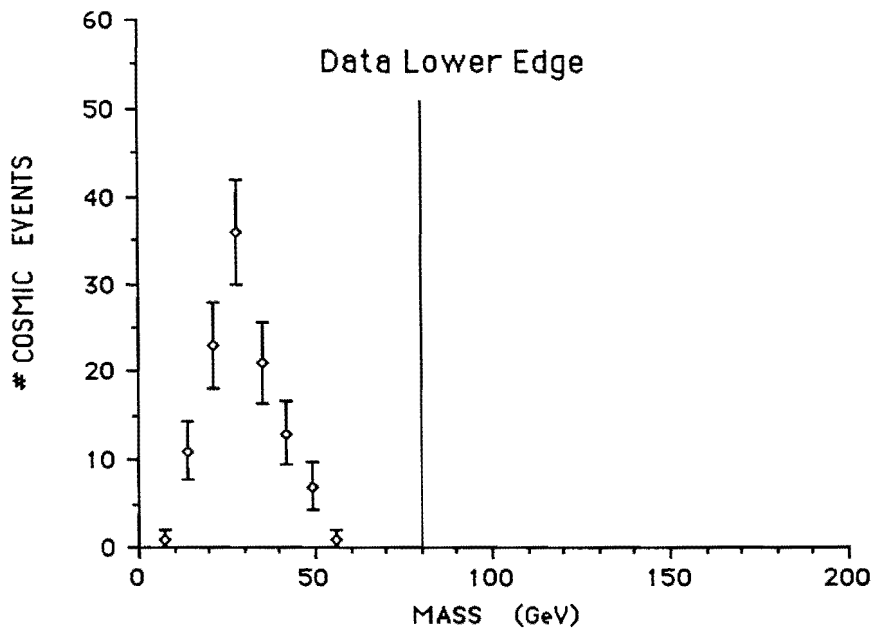

Fig. 7.4 Distribution of apparent dijet mass from cosmic background.

CHAPTER 8

Resolution and unsmearing

In this Chapter we describe the work done to correct the two-jet invariant mass spectrum to account for the effect of finite resolution.

The resolution has been determined from the QFL simulation, with no reference to the studies of jet balancing based on real data, as discussed in Chapter 6. The reason for this is that it is not easy to eliminate the effect of jet direction correlation and extract the absolute value of the resolution from studies of jet balancing. Indeed, we used that method as a handle for relative resolution studies. On the other hand, the simulation program is carefully tuned on a large set of data, from both the test beam and the CDF runs[27]. Actually, it turns out that the simulation closely mimics the data also with respect to jet balancing. In summary, we found the simulation to be sufficiently trustworthy for this job. In Chapter 10 we will estimate the systematic error introduced by the simulation.

An additional and rather fundamental reason for using the simulation is that we wish to adopt a purely experimental definition of "resolution". That means we would like to take into account only detector effects, and not, for instance, the fluctuations in the parton energy emitted (at the vertex) outside the jet cone or other physical effects that cannot be disentangled from the resolution in balancing measurements.

Our procedure to perform the correction on the data is to smear with the given resolution an appropriate parametric function, and determining the parameter values by fitting the smeared curve to our data. The data points are then divided by the ratio of the smeared curve to the original one (the "smearing factor").

In the smearing process we took into account the detailed shape of the resolution function, which is asymmetric and has non gaussian tails.

The smearing was done with two different methods:

a) by fitting the shape of the resolution function by an analytical expression and performing a numerical evaluation of the smeared cross section;

b) by using an analytical approximation of the integral which represents the smeared cross section. In this methods one needs only the first few moments of the resolution function.

The two results have been compared as a cross-check.

8.1 Formalism

First of all, let us give a formal description of the smearing problem.

Let x be an observable (that we will later identify with M_{jj}) and f(x) its probability distribution; let $\tilde{x}$ be the measured value of x and $\tilde{f}(\tilde{x})$ its distribution (the "smeared" function we measure). Then we have:

$$\tilde{f}(\tilde{x}) = \int f(x)g(\tilde{x}-x,x)dx \tag{1}$$

where g is our resolution function. This means g(y,x)dy is the probability of making a measurement error of size y, that is the probability of finding the value x+y when the actual value is x. We allow it to depend not only on y but also on x, so we have a different resolution function for every possible value of x. They must all be normalized:

$$\int g(y,x)dy = 1 \qquad \forall x \tag{2}$$

but are not required to have zero mean. The normalization of f is unimportant.

The appearance of the integration variable in both of g's arguments being unpleasant, we define another function h:

$$h(y,z) \equiv g(y,z-y) \tag{3}$$

then we can rewrite the integral with x appearing only in the first of h's arguments:

$$\tilde{f}(\tilde{x}) = \int f(x)h(\tilde{x}-x,\tilde{x})dx \tag{4}$$

Finally, by replacing $x = \tilde{x}-t$ we get to the form that we find most convenient for our purposes[1]:

$$\tilde{f}(\tilde{x}) = \int f(\tilde{x}-t)h(t,\tilde{x})dt \tag{5}$$

The h function has the following interpretation: $h(t,\tilde{x})$ is the probability of having made an error t when we get the value $\tilde{x}$ from our measurement. Like g, h represents the resolution, but from a different point of view.

Let's also define C and μ respectively as the normalization and mean[2] of the h distribution:

$$C(\tilde{x}) \equiv \int h(t,\tilde{x})dt \tag{6}$$

$$\mu(\tilde{x}) \equiv \frac{1}{C(\tilde{x})}\int t\, h(t,\tilde{x})dt \tag{7}$$

8.2 Measuring the resolution

The g and h functions have been evaluated with the QFL simulation program, using a

[1] Note that the change in the integration variable does not bring in a minus sign.

[2] It is to be noticed that, excluding the trivial case $\partial g(y,z)/\partial z=0 \Rightarrow g(y,z)=h(y,z)$, normalization and mean of the h distribution are not the same as for g. Also, g being gaussian does not imply h being gaussian or even symmetrical.

modified version of the ISAJET program that generates events according to a flat distribution in Pt. What we actually need is a flat distribution in invariant mass. However, the required correction can be applied with little effort.

We generated about 130K events with M_{jj} ranging from zero to 1200 GeV. We reconstruct the measured mass M_{meas} for each event with the same code used in the data analysis. The true mass M_{true} is evaluated according to our definition of jet, that is the set of all particles emitted by the scattered parton within a cone of the specified η–φ radius around the cluster axis [28].

We have made two scatter plots of M_{meas} - M_{true}, one versus M_{true} (g function) and the other versus M_{meas} (h function). The original distribution of M_{true} is shown in fig.8.1, and it is not completely flat. To correct for this, we have "poured" events from an additional simulation run to fill all bins of our plots to the same average level, while preserving the statistical fluctuations (Fig. 8.2). The final distributions obtained after this correction to the generated spectrum[3] are shown in Figs 8.3, 8.4.

By looking at the plots it is evident that there is a long tail in the region of negative $M_{meas} - M_{true}$, indicating non gaussian losses in the calorimeter. This is better shown in figs. 8.5, 8.6 where some slices of the g and h plots at given masses are displayed. The tail gets more pronounced with increasing mass, and is more pronounced in h than in g. We have further investigated this in order to understand what is the source of this effect and to make sure it is not due to some characteristic of the simulation not reflecting a real effect.

First of all we have verified that the energy losses are not due to particles lost by the detector simulation because of software errors. Then we studied the possible detector causes of energy losses. For each event we divided the contributions to the jet losses into three classes:

- EN_LEAK : energy lost because of punch–through and shower leakage from the back of the calorimeter;
- EN_UND : particles not reaching the calorimeter region at all;
- EN_LOST : energy lost in dead areas, namely any non active material or space traversed by the particles before or inside the calorimeter.

In fig. 8.7 the scatter plots show these three lost energy contributions versus the mass measurement error M_{true}-M_{meas} for events with masses between 400 and 500 GeV. It appears that the leakage and bending effects have a small influence, while there is a clear correlation with losses in dead areas. This shows that the tail of the resolution comes mainly from a known detector effect, that is also the main responsible for the response non–linearity. A study on the degree of accuracy of the simulation of these effects has been described in [27]. We discuss the systematic error due to simulation of non–linear effects in Chapter 10.

[3] Note that we need to generate events at true masses higher than the maximum M_{meas} in the h plot in order to avoid a depletion in the bottom right region of the h plot. It is easy to see that one needs to extend the range by the half-width of the plot in y, that is 500 GeV in this case.

Coming back to figs. 8.5, 8.6, another obvious feature of the plots is that for M_{jj} larger than about 400 GeV there is a larger and larger deviation of the mean from zero. This can be understood by recalling that our analysis program corrects the jet 4-momenta with the formulas described in Chapter 5, which were fitted on a sample of events having masses smaller than 400 GeV. Therefore, at higher masses the correction is just an extrapolation, and the fact that it becomes less accurate is not surprising.

However, the mean is slightly different from zero also at lower masses. This can be ascribed in part to the fact that we are using a slightly different definition of jet [28], and in part to the fact that the correction formula we used was developed in order to adjust the scale of the jet 4–momentum, and not that of the mass[4].

8.3 Smearing procedures

To obtain the smearing factor one has to calculate the integral (5) assuming some parametric function f_{fit} for f and tuning the parameters to fit the data. Then the ratio between the smeared function and f_{fit} will give the smearing factor.

To perform the integration (5), one has either to know the details of the resolution function $h(t,M_{meas})$ or to find some approximation, such as an appropriate series expansion, that allows the use of global properties of the resolution function like its mean and its variance. We used both methods and compared the results.

In the first method we assumed a parametric form for the resolution function h and we determined the parameters by fitting the simulated data of fig. 8.6. We will call this method

[4] At a first glance, it may seem that once the right scale of jet energy and momentum is set, all derived quantities will also have the right scale, but this is not so. Indeed, if a quantity f is a function of a set of random variables x and the average of x is μ, one has in general:

$$\langle f(x)\rangle \neq f(\mu)$$

To get a feeling for the order of magnitude of this effect in our case, let usexpand f in a series to the second order around μ :

$$f(x) \approx f(\mu) + \sum_j \frac{\partial f}{\partial x_j}(x_j - \mu_j) + \frac{1}{2}\sum_j\sum_k \frac{\partial^2 f}{\partial x_j \partial x_k}(x_k - \mu_k)(x_j - \mu_j)$$

$$\langle f(x)\rangle \approx f(\mu) + \sum_j \frac{\partial f}{\partial x_j}\int (x_j - \mu_j)P(x_j)dx_j + \frac{1}{2}\sum_j\sum_k \frac{\partial^2 f}{\partial x_j \partial x_k}\int (x_k - \mu_k)(x_j - \mu_j)P(x_k,x_j)dx_j dx_k$$

$$\langle f(x)\rangle \approx f(\mu) + \frac{1}{2}\sum_j \frac{\partial^2 f}{\partial x_j^2}\sigma_j^2 \qquad \left(\sigma_j^2 = \int (x_j - \mu_j)^2 P(x_j)dx_j\right)$$

To make a simple estimate of the effect in our case, suppose the jets are massless ($E=|\mathbf{P}|$) and exactly back to back; then:

$$M(E_1,E_2) \approx 2\sqrt{E_1E_2}$$

$$\langle M(E_1,E_2)\rangle \approx M(E,E) - \frac{\sigma_E^2}{2M(E,E)}$$

By putting in the numbers, it turns out that the mass will be underestimated by an amount of the order of a GeV.

It is easy to understand intuitively how this happens, by noticing that the fluctuations in the energy measurements cause the total energy of the dijet system to fluctuate both up and down, but the modulus of the dijet momentum can only fluctuate up. Since $M^2=E^2-|\mathbf{P}|^2$, on the average the mass gets underestimated. It can be seen that angular errors also contribute in the same direction.

"smearing by integration" because the integral (5) is explicitely calculated.

In the second method we expanded the f funtion of equation (5) in a Taylor's series truncated to a suitable order. As we will see this reduces the integral (5) to the calculation of the moments of the h function. We will call this method "smearing by expansion".

The two procedures carry two different systematic errors on the mass spectrum. For example, fitting the resolution function h requires the assumption of some functional form which may be different from the true parent distribution. On the other hand, uncertainties come from truncating the Taylor's series as well as from estimating the moments of h with a finite statistics.

Comparing the results from the two methods provides an estimate of the systematic error introduced by the procedures.

8.3.1 Smearing by Integration

This method consists of the following steps:

i) Slicing the resolution function.

We divided the scatter plot of fig. 4 into vertical slices 20 GeV wide. Each slice represents the resolution function $h(t,M_{jj})$ for a given value of the measured mass M_{jj}.

ii) Fitting the resolution.

We fit each slice with the functional form

$$h_1(t,M_{jj}) = \frac{1}{c}\int \frac{1}{a} e^{\frac{(y-\mu)}{a}}\, \theta(\mu-y)\, \frac{1}{b\sqrt{2\pi}}\, e^{-(t-y)^2/2b^2}\, dy \qquad (8)$$

$$\text{where:} \quad \theta(\mu-y) \begin{cases} = 0 & y > \mu \\ = 1 & y < \mu \end{cases}$$

and determined the a, b, c, μ parameters for each value of M_{jj}.

The idea is to express h as the convolution of a gaussian term (corresponding to some "basic" resolution) with an exponential term truncated by the θ function (corresponding to the effects generating the asymmetric losses). The "center" μ of the distribution is allowed to be different from zero, to account for the mass scale correction.

iii) Interpolating the resolution parameters.

We plotted the parameters a, b, c, μ found in step ii) as functions of the measured mass M_{jj} and we fit the plots with low degree polynomials in M_{jj}. Fig. 8.8 shows the result of these fits.

At this point we had an easily computable approximation of the resolution function $h(t,M_{jj})$:

$$h_2(t,M_{jj}) = \frac{1}{c(M_{jj})}\int \frac{1}{a(M_{jj})} e^{\frac{(y-\mu(M_{jj}))}{a(M_{jj})}} \theta(\mu(M_{jj})-y) \frac{1}{b(M_{jj})\sqrt{2\pi}} e^{\frac{-(t-y)^2}{2b(M_{jj})^2}} dy \tag{9}$$

where $a(M_{jj})$, $b(M_{jj})$, $c(M_{jj})$, $\mu(M_{jj})$ are known polynomials and the integral is evaluated by numerical techniques.

Fig. 8.9 shows some examples of the function $h_2(t,M_{jj})$ superimposed to simulated data.

iv) Smearing the parent distribution.

Finally, we assumed for the unsmeared spectrum the functional form:

$$\frac{d\sigma}{dM_{jj}} = f_{fit}(M_{jj}) = \left(\frac{M_{jj}}{C}\right)^{\gamma} \exp\left(\frac{M_{jj}}{\alpha}\right) \tag{10}$$

and we evaluated the integral (5) numerically:

$$\tilde{f}_{fit}(\tilde{M}_{jj}) = \int f_{fit}(M_{jj})\, h_2(\tilde{M}_{jj} - M_{jj}, \tilde{M}_{jj})\, dM_{jj}$$

Equation (10) contains three parameters: C, γ, α which were determined by fitting the smeared curve to the experimental mass spectrum.

8.3.2 Smearing by Expansion

First of all we define a new variable, representing the measured observable corrected for the non zero mean of h (independently of the mean of g), and expand f in Taylor's series around that value:

$$\hat{x} \equiv \tilde{x} - \mu(\tilde{x}) \tag{11}$$

$$f(\tilde{x}-t) = f(\tilde{x}) + \sum_{n=1}^{\infty} \frac{[\mu(\tilde{x})-t]^n}{n!} f^{(n)}(\tilde{x}) \tag{12}$$

hence:

$$\tilde{f}(\tilde{x}) = f(\tilde{x})\int h(t,\tilde{x})dt + \sum_{n=2}^{\infty} \frac{f^{(n)}(\tilde{x})}{n!}\int [\mu(\tilde{x})-t]^n h(t,\tilde{x})dt \tag{13}$$

In (13), the n=1 term was dropped, being identically zero because of how μ is defined.

We can rewrite this formula in terms of the moments of the h function:

$$M_n(\tilde{x}) \equiv \frac{\int [(t-\mu(\tilde{x})]^n h(t,\tilde{x})dt}{C(\tilde{x})} \tag{14}$$

$$\tilde{f}(\tilde{x}) = C(\tilde{x})\left[f(\tilde{x}) + \frac{f''(\tilde{x})}{2}\sigma^2(\tilde{x}) + \sum_{n=3}^{\infty}(-1)^n \frac{f^{(n)}(\tilde{x})}{n!} M_n(\tilde{x})\right] \tag{15}$$

This is our formula[5], expressing the integral (5) in terms of the derivatives of the function to be smeared and of the moments of the resolution function.

Of course we need to truncate the series at some suitable n. How many terms do we need? We can easily get a qualitative estimate. If the f function can be well approximated by a polynomial of degree n within a range of the order of the width of the resolution, then n terms will do. That means, if f is reasonably smooth (as in our case) we need very few terms (actually, it occurs rarely in practice to be interested in fitting data with a function which is detailed to a much finer scale than the experimental resolution).

Looking back to our h function, we observe that the presence of a long tail makes the convergence of our moment series slower, even if this tail has very little influence in the smearing. In fact, the events in the tail have been shifted downward into a mass region where the cross section is much higher than the cross section at the mass to which they really belong[6]. Therefore, if we use a truncated function in place of the original one the result will not be affected very much, since those events add so little that dropping them makes no real difference. On the other hand, the moments of the truncated function are much smaller, thus making the convergence of our series quicker. We stopped at n=4.

To select a safe cut, we made sure that the fraction of rejected events times the factor of cross section drop at the cut is small. This quantity, that represents an upper bound to the size of the effect we are neglecting, was never larger than a fraction of a percent, that is completely negligible when compared with other uncertainties in our measurement.

From this trimmed function we have evaluated the moments we need and fitted them with low degree polynomials in M_{jj}. The first four derivatives of the fitted function (10) were evaluated analytically and, together with the moments of the h function, provide our analytical expression (15) of the smeared cross section, that has been fitted to the data.

8.4 Results

We have used in the fits only the data in the mass range above 80 GeV, to get rid of the bias

[5] The formula clearly exhibits a couple of not immediately intuitive aspects:

a) even a constant distribution gets changed by the smearing when, as in our case, the resolution depends on the energy (C is constant only if the resolution is a constant);

b) the first derivative does not appear. Any straight line gets just the same smearing as a constant, independent of the slope. To the leading order, the amount of smearing is related to the curvature of the function, not to its slope.

[6] Of course the presence of a positive tail would have been a much more serious matter. Note that care has been taken to suppress hot spots carefully (see Chapter 2).

of the JET_20 trigger. We obtained a very good fit.

As we said in the introduction, the smearing factor is defined as the ratio between the smeared and the original curve (10). To obtain the unsmeared cross section the 'raw' mass spectrum must be divided by the smearing factor. The smearing factors resulting from the two methods are shown in fig. 10 as functions of the invariant mass. The two functions agree very well over most of the range, but they differ by 10÷20 % in the low mass region. This was found to be due to the difficulty in determining the shape of the narrow resolution functions at low M_{jj} . However, we have not taken the trouble of a more accurate determination of such shapes, nor of accounting for this systematical uncertainty, because the low mass region is not going to be used in fitting the theoretical predictions to our data. This is because this region is affected by sizable uncertainties that are not easy to estimate, as we will see in Chapter 10.

Finally, to verify the convergence of the series (15) in the case of smearing by expansion, the first few terms contributing to the smearing factor are compared in fig. 8.11. It should be noted that the term with n=0 is mainly related to the offset in the mass scale discussed above. The leading resolution–related term is n=2.

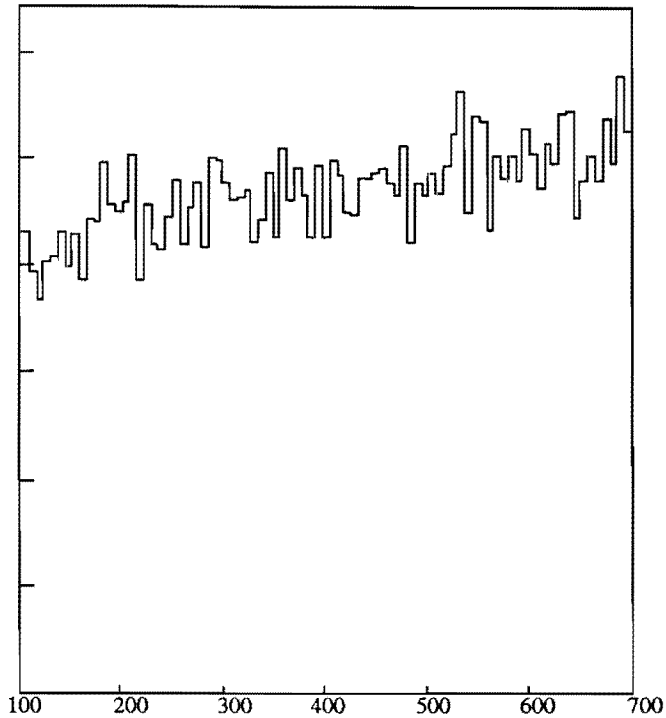

Fig. 8.1. True mass distribution before filling.

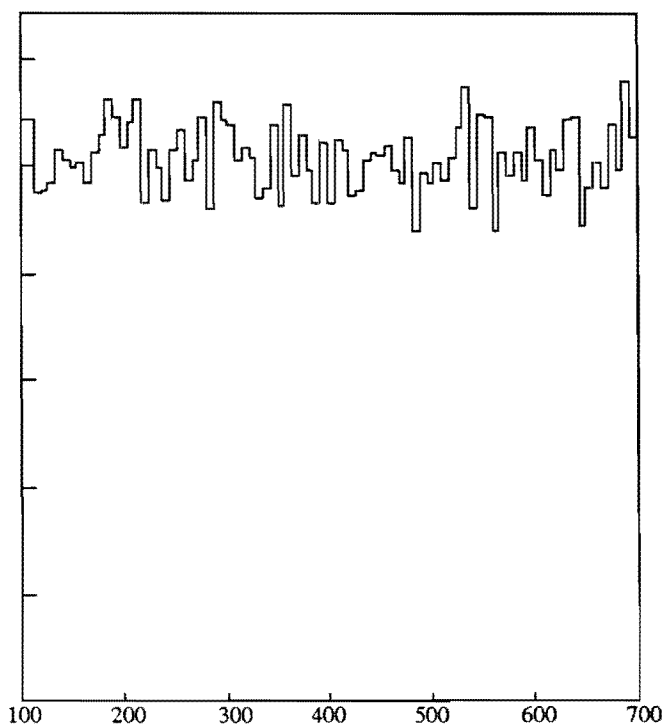

Fig. 8.2. True mass distribution after filling.

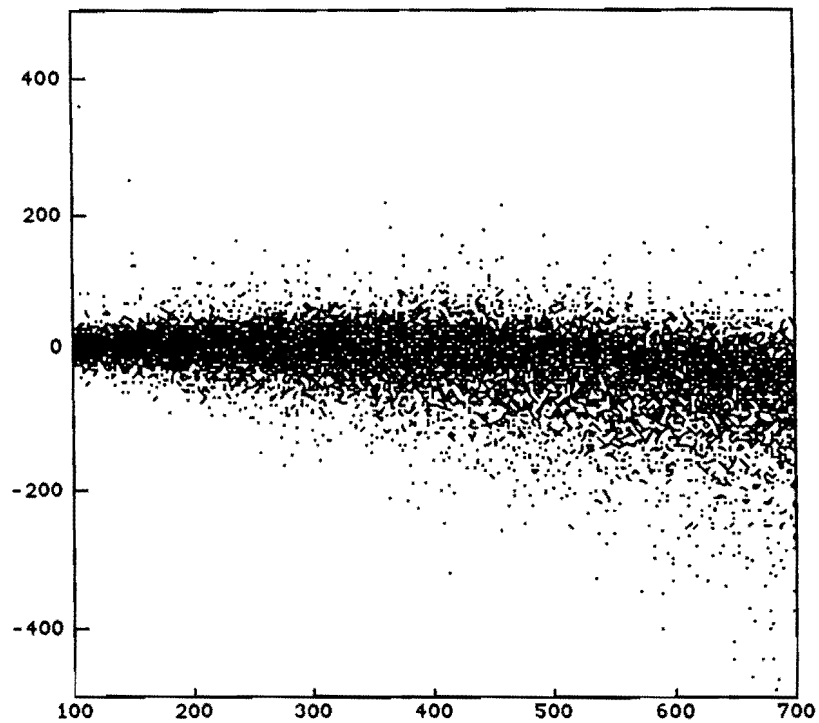

Fig. 8.3. M_{meas}- M_{true} vs. M_{true} (g function).

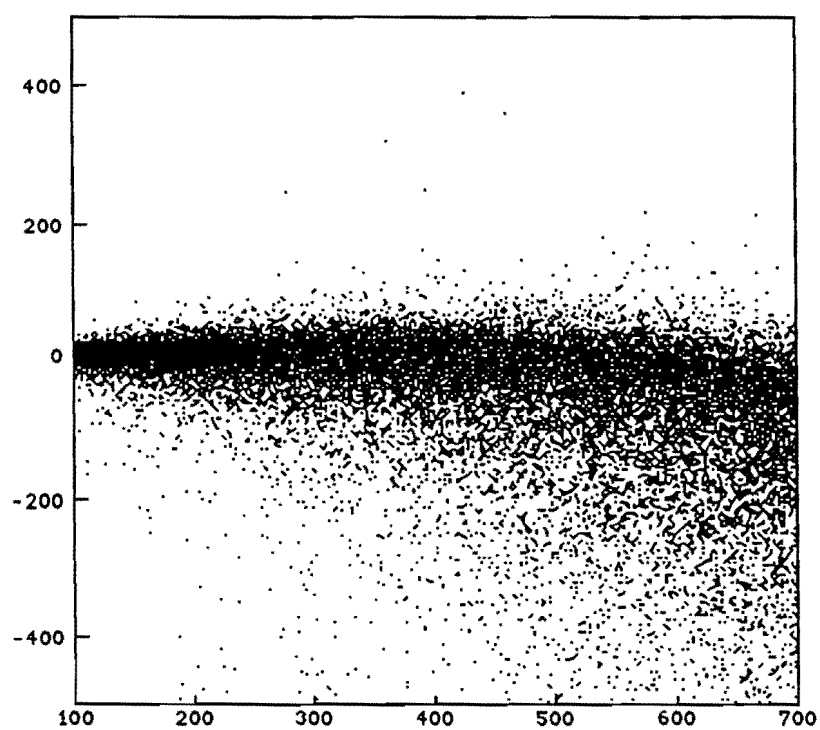

Fig. 8.4. M_{meas}- M_{true} vs. M_{meas} (h function).

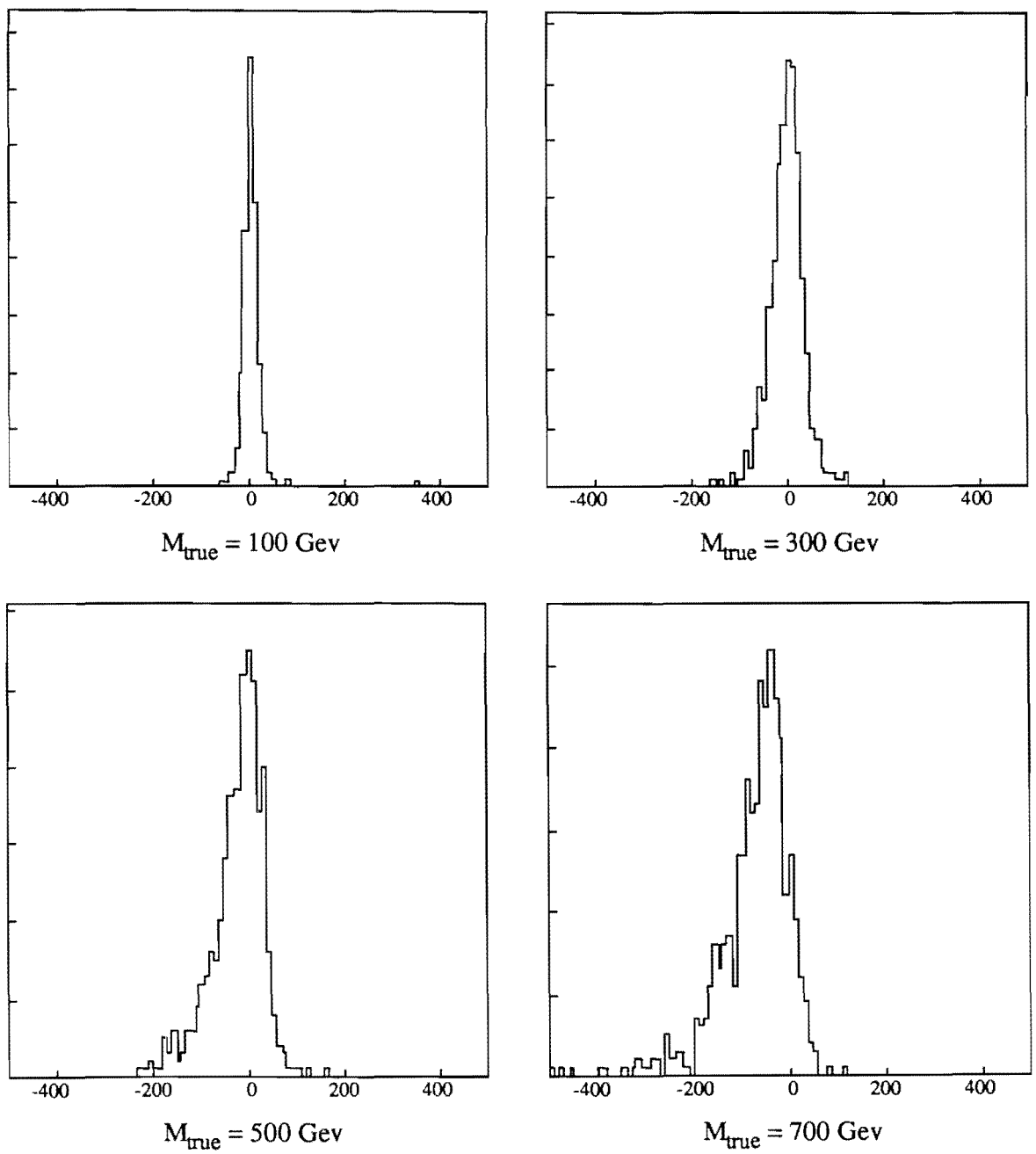

Fig. 8.5. Some slices of the g function plot in fig. 8.3.

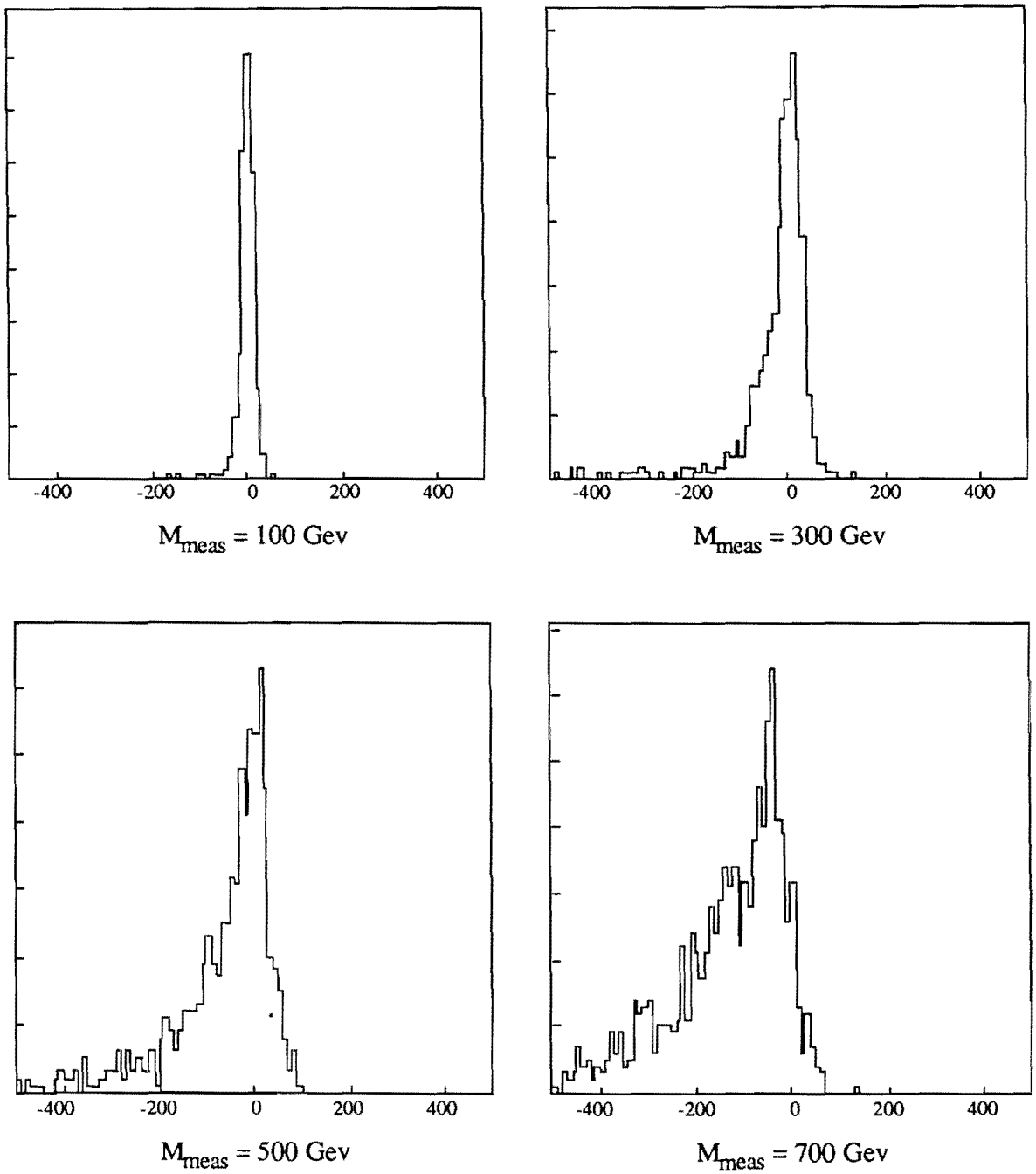

Fig. 8.6. Some slices of the h function plot in fig. 8.4.

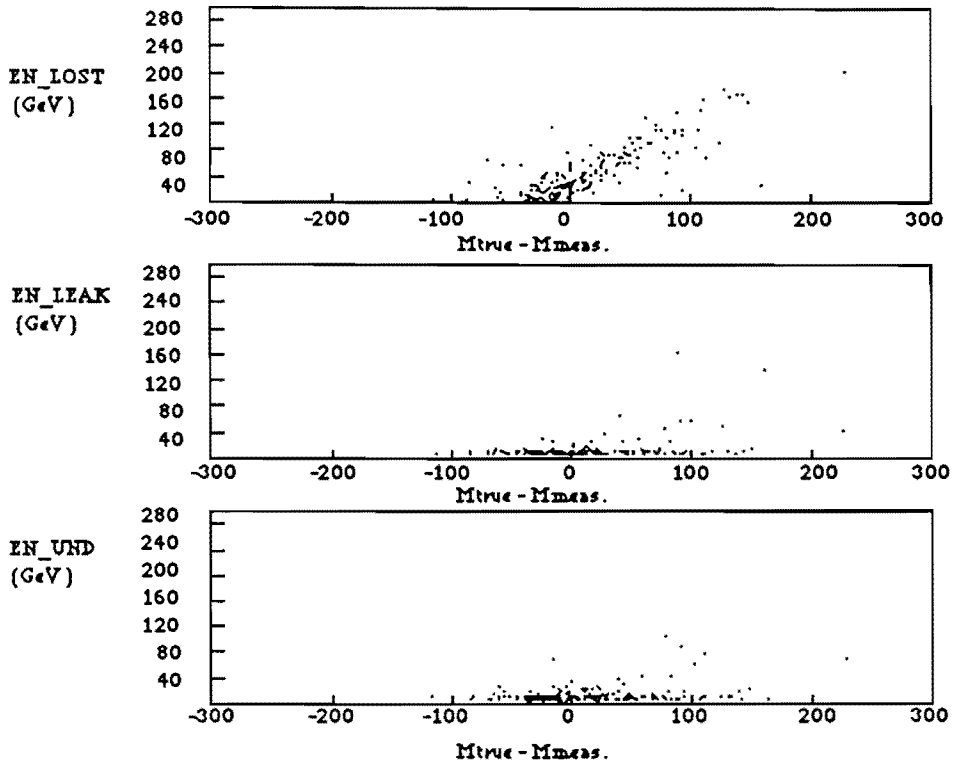

Fig. 8.7. Correlations between jet energy losses and mass mismeasurement.

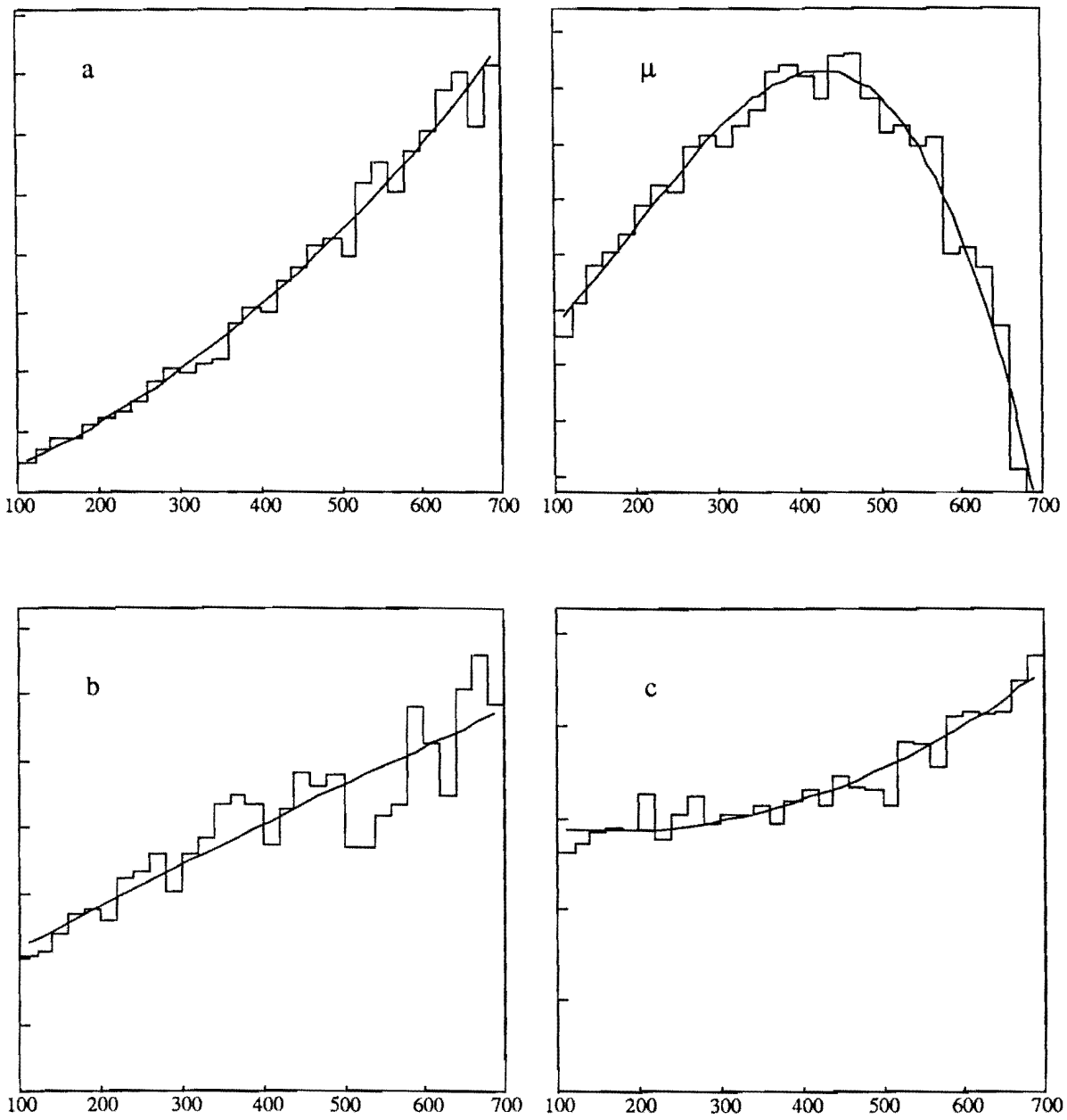

Fig. 8.8. Resolution parameters a, μ, b, and c as functions of the measured mass (see text)

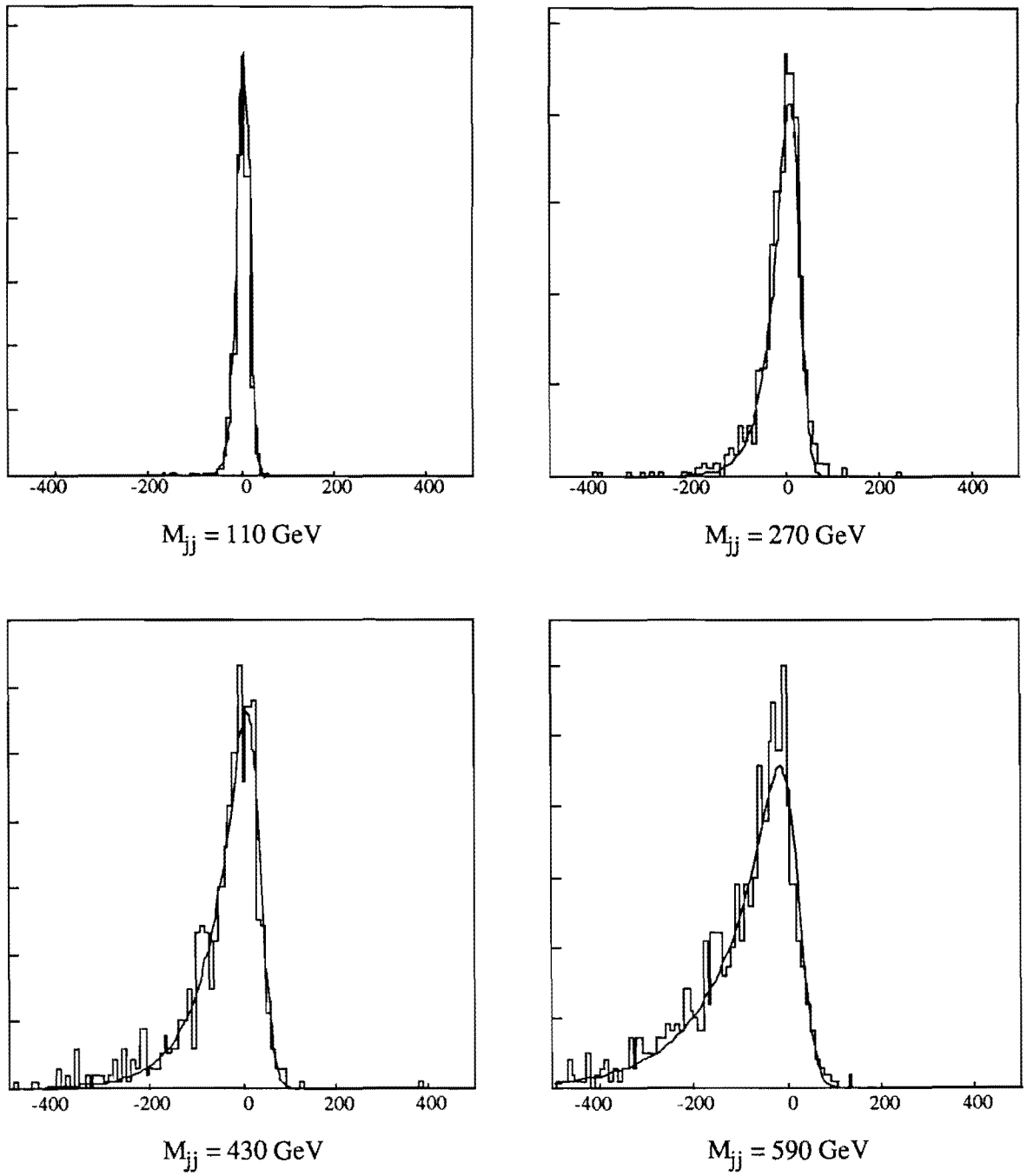

Fig. 8.9. Examples of simulated resolution functions and analytical approximations.

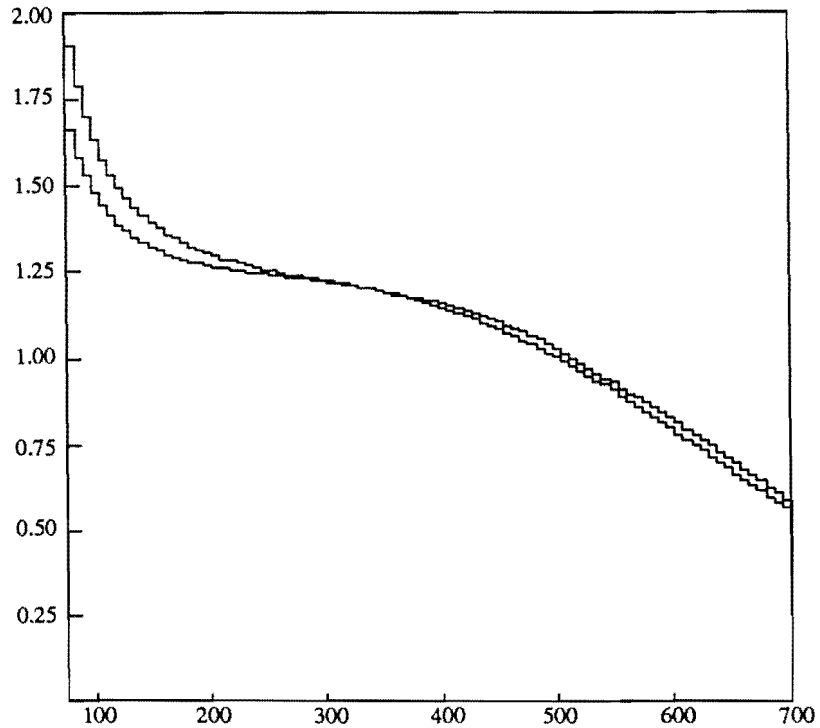

Fig. 8.10 Comparison of smearing factors from the two methods.

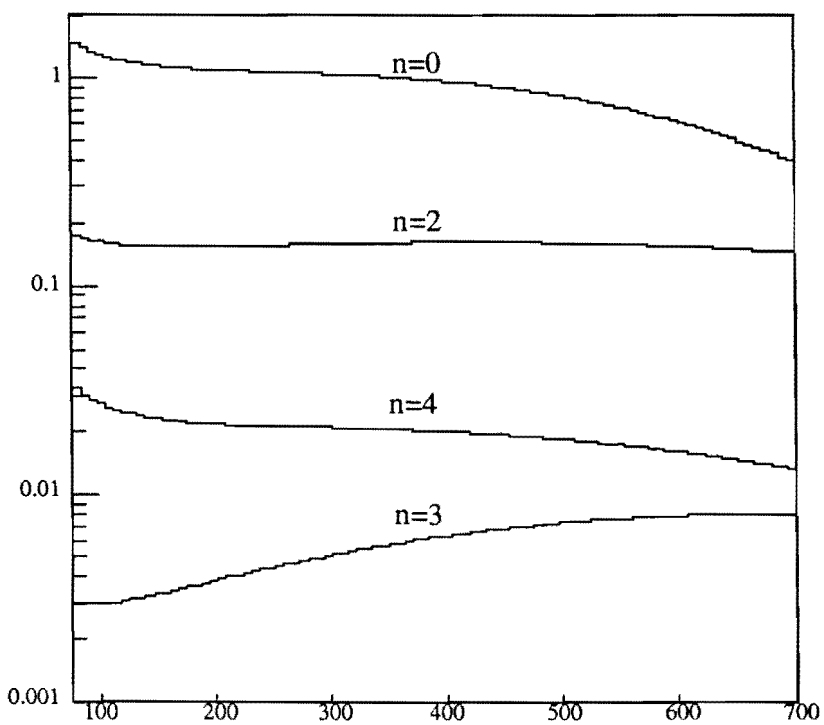

Fig. 8.11 Single term contributions to the smearing factor

CHAPTER 9

Systematic uncertainties

We report here the results of a study of the major sources of systematic uncertainty in our measurement of $d\sigma/dM_{jj}$.

As seen in the previous chapters, the procedure followed to obtain the final $d\sigma/dM_{jj}$ relies heavily on ISAJET and QFL for determining the mass scale and the mass resolution (Chapter 7). Most of the systematic error on the M_{jj} spectrum comes from the use of the QFL simulation.

Along with the effect of the simulation uncertainties on the mass spectrum, other sources of systematic error were also considered.

We summarize the effects studied in the following list:

1) uncertainty in the fragmentation functions;
2) uncertainty in the effect of the 90° crack;
3) uncertainty in the non linear calorimeter response to low energy particles;
4) uncertainty in the charged/neutral response ratio;
5) uncertainty in the underlying event energy;
6) uncertainty in the absolute calorimeter calibration;
7) uncertainty in the integrated luminosity.

Item 1) to 5) correspond to uncertainties in the generation–simulation Montecarlo

9.1 Simulation Uncertainty

We varied one parameter at a time in the simulator within its uncertainty range and looked at the effect on the mass spectrum.

First of all we generated the mass spectra using ISAJET and QFL with identical parameters as those used to calculate the mass scale and the mass resolution for the data analysis, with the proper fast falling E_T distribution.

The events simulated through the detector were analyzed as the real data (actually with the

same program). To obtain good statistics in the high mass region we generated several sets of events with increasing minimum parton P_T in ISAJET . The different runs were normalized using the luminosity information given by ISAJET, and joined together, cutting the regions biased by the generation thresholds (a procedure similar to that used to merge real data obtained with different triggers). Finally, the unsmearing was applied as described in Chapter 7 to obtain the spectrum shown in Fig. 9.1. We will call this the "reference spectrum", $d\sigma_{ref}/dM_{jj}$. The solid line represents a fit with the usual parametric curve.

To measure the effect on the spectrum of the uncertainty of a given parameter we simulated events and repeated the whole analysis with that parameter set to its limit values. The idea is to keep firm the analysis path and to change the data under the hypothesis that the reality is slightly different from what we have assumed in calculating the scale correction and the resolution. So we produced two additional spectra for each parameter under study ($d\sigma_{up}/dM_{jj}$, $d\sigma_{low}/dM_{jj}$) using an upper and a lower bound for the parameter. The mass scale and the unsmearing corrections applied to the new data are exactly the same used for the $d\sigma_{ref}/dM_{jj}$ spectrum.

It should be pointed out that "resolution" is not an independent parameter in our analysis, since it is a function of the parameters that we varied in the simulation. For this reason the systematic error due to an incorrect estimate of calorimeter resolution is not an independent uncertainty but is rather automatically accounted for in the above process.

The differences between the limiting and the reference spectra are our estimate of the systematic error due to the parameter under study. To get rid of the statistical bin to bin fluctuations we computed the fractional differences between the fitting curves. To estimate the statistical error on the determination of the systematic error we generated a second sample of reference data with the same statistics. The difference between the two reference spectra gives an idea of the statistical error, which is of few percents and is negligible on the scale of our systematics.

9.2. Systematic Uncertainties on the Dijet Cross Section

Fig 9.2 displays a summary of the obtained results.

9.2.1 Charged/Neutral ratio

The contribution to the systematic error from the uncertainty on the charged/neutral response ratio was already studied in previous CDF analyses, and turned out to be much smaller

than the other ones (fractional error on cross section: 2-3 % [29]). For this reason we did not repeat this study in our analysis.

9.2.2 Underlying Event

An upper bound for the error due to a possible underlying soft component was determined as follows. We produced a spectrum by duplicating the analysis of the '89 data but not correcting for the underlying event. The curve shown in Fig. 9.2 is obtained as the fractional difference between the fits to the unsmeared spectra. The underlying event correction is a small and nearly constant amount of energy subtracted to both jets in the event. This explains why its effect decreases rapidly as the event mass increases.

9.2.3 Fragmentation Functions

From the study described in CDF-686 we decided to use the FF fragmentation function parametrization (a=.88, b=2.0), that seems to reproduce the CDF data, to obtain the reference sample. The TASSO (a=.57, b=2.0) and FSR (a=.96, b=3.0) parametrizations were used as extreme settings to obtain the $d\sigma_{up}/dMjj$ and $d\sigma_{low}/dM_{jj}$. The fragmentation curve in Fig. 9.2 represents the quantity

$$(d\sigma_{up}/dM_{jj} - d\sigma_{low}/dM_{jj}) / (2*d\sigma_{ref}/dM_{jj}).$$

9.2.4 Crack at 90°

Here we performed a rough test by a rather drastic change of the 90° crack simulation. In order to obtain the $d\sigma_{up}/dM_{jj}$ we completely turned off the crack simulation, while to obtain $d\sigma_{low}/dM_{jj}$ we doubled the nominal width of the crack. Fig. 9.2 shows the fractional difference between $d\sigma_{up}/dM_{jj}$ and $d\sigma_{low}/dM_{jj}$. This should be considered more as an upper limit for the 90° crack contribution. It is interesting to note that this is the only relative contribution that increases with the mass.

To get a feeling for the effect of varying the crack width from 0 to a factor 2, we plotted as control variables the $\eta_{detector}$ distributions of the leading jets. This is shown in Fig. 9.3, superimposed to the real data. These plots show that the two simulations actually bracket the real data.

9.2.5 Calorimeter Nonlinearity

In this case $d\sigma_{up}/dM_{jj}$ and $d\sigma_{low}/dM_{jj}$ are obtained by changing by a factor 5 % up and down the calorimeter response to particles of energy below 10 GeV. Again, Fig. 9.2 shows the fractional difference between the upper and lower spectra.

9.2.6 Luminosity

The 15% luminosity uncertainty is directly reflected as a 15% scale uncertainty on $d\sigma/dM_{jj}$.

9.2.7 Calorimeter Calibration

The uncertainty on the absolute calorimeter calibration is quoted to be smaller than 1% [10] and its contribution to the systematic error on $d\sigma/dM_{jj}$ is negligible.

It can be seen in Fig. 9.2 that the total systematic error turns out to be nearly constant as a function of M_{jj}, at the level of 30%.

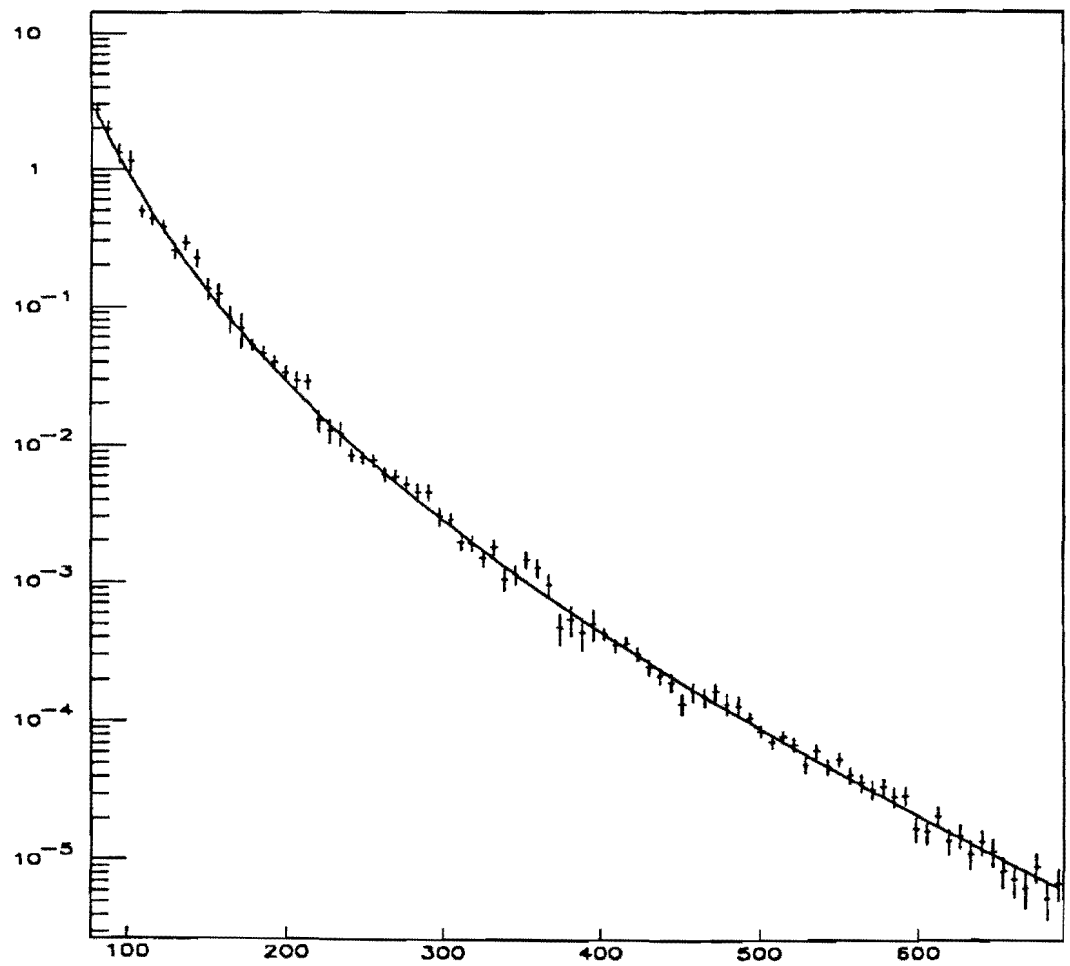

Fig. 9.1 $d\sigma/dM_{jj}$ spectrum from ISAJET

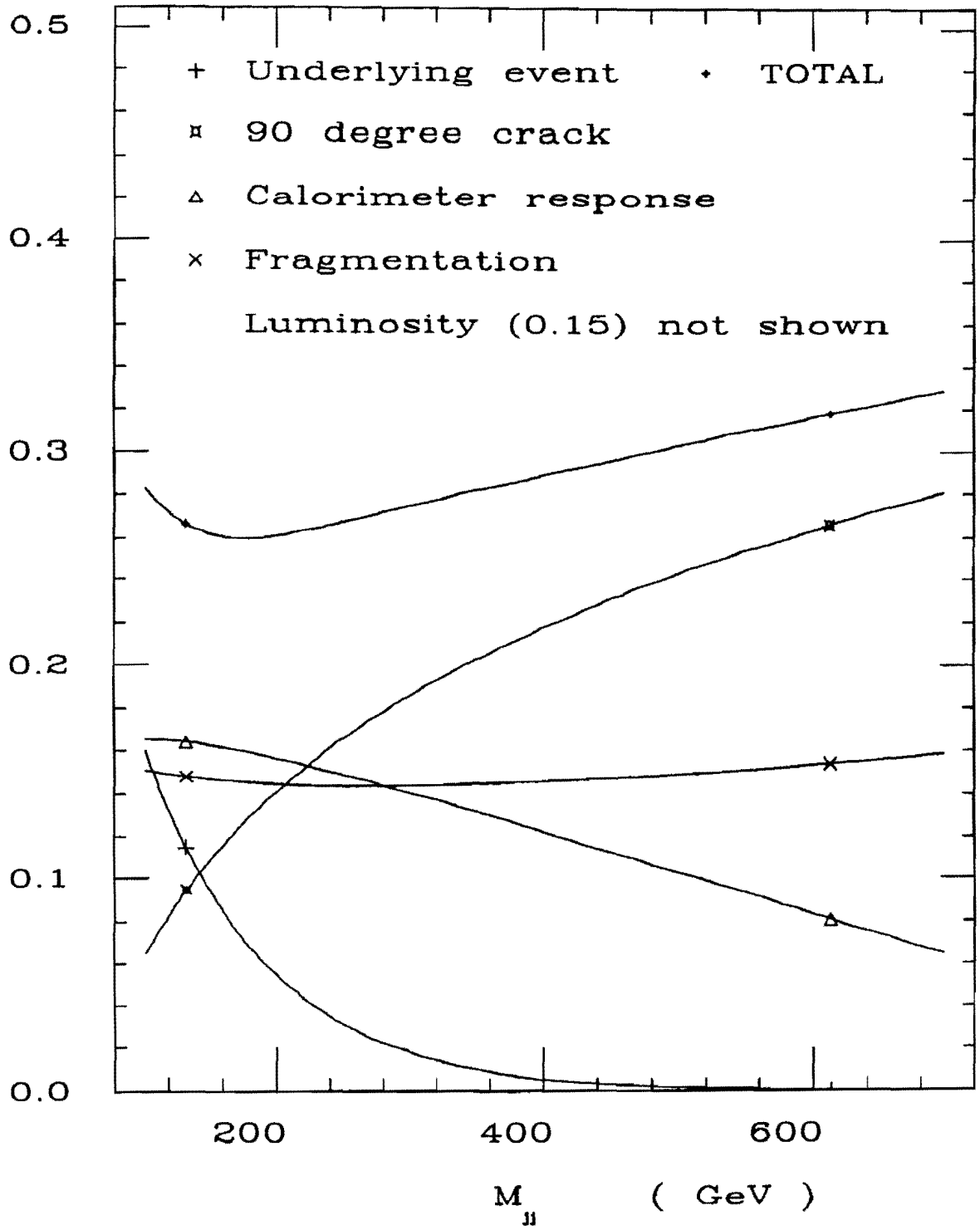

Fig 9.2 Relative systematic uncertainties on $d\sigma/dM_{jj}$

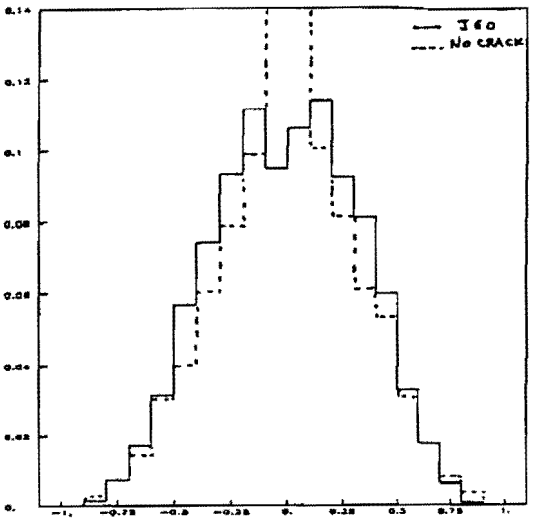

Jet 1 $\eta_{detector}$ (no crack)

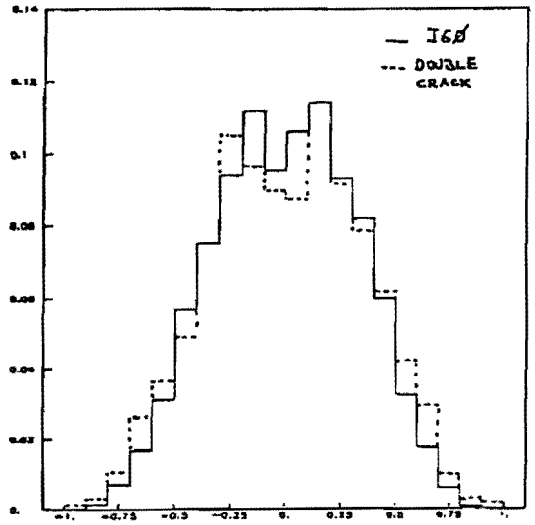

Jet 1 $\eta_{detector}$ (doubled crack)

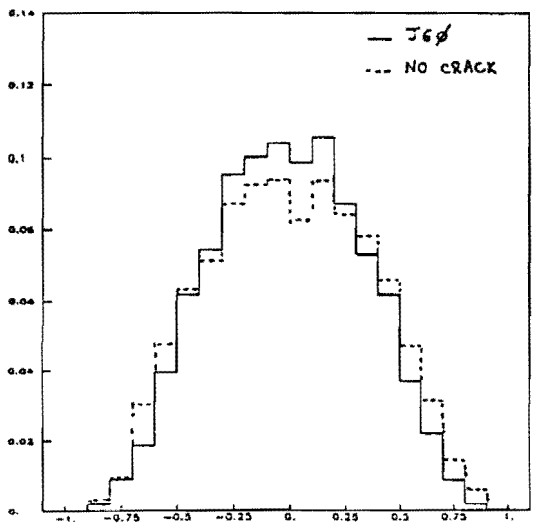

Jet 2 $\eta_{detector}$ (no crack)

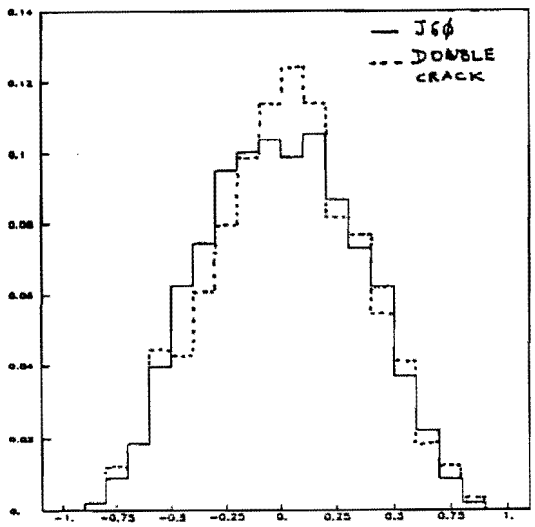

Jet 2 $\eta_{detector}$ (doubled crack)

Fig 9.3 $\eta_{detector}$ distributions for leading jets from simulation and JET_60 trigger.

CHAPTER 10

Radiation effects

The significance of a $d\sigma/dM_{jj}$ measurement is subject to some doubt because of the lack of a precise understanding of which are the multijet systems whose mass distributions are relevant to our physics investigations. The source of this ambiguity is the presence of radiation from initial and final states in the hard parton scattering process. Radiation can produce additional clusters of energy – i.e. additional jets – and the presence of these additional jets can lead to different strategies when trying to define "effective" dijet events.

We chose to define M_{jj} simply as the mass of the system composed of the two leading E_T jets. Additional jets are treated in an inclusive way, i.e. we accept their presence, but do not take them into account in any way. This is a well defined procedure, which experimentally saves us from having to deal with low energy jets in an exclusive way.

However, even with this definition, the comparison of our spectrum with the $2 \rightarrow 2$ QCD calculation must take radiation effects into account. The impact of radiation on the result also depends on clustering parameters and event selection criteria which eventually determine the definition of leading and secondary jets. Ideally, the two measured leading jets are supposed to reproduce the two final state partons considered in the theoretical calculation.

Since we plan to compare data with a leading order $2 \rightarrow 2$ QCD calculation, we would like to suppress events from hard higher order diagrams. On the other hand, final state radiation produced in the fragmentation process should be included in the mass, for a fair comparison to the leading order $2 \rightarrow 2$ QCD calculation.

This is also the case if we wish to investigate possible resonances in the dijet spectrum. In fact, if some energy is lost due to final state radiation off one leading parton into which the resonance decays, the mass of the whole multi-jet system will correspond to the resonance mass rather than the mass of the two leading jets only. On the other hand, when considering additional jets for the calculation of the mass, we must avoid adding jets coming from initial state radiation, as these would also introduce a spurious offset and worsen the resolution.

One cannot tell by sure whether a secondary jet is due to initial or final state radiation, and this is an unavoidable source of uncertainty. Strictly speaking, the above question is meaningless, because the scattering amplitudes from the two kinds of processes add up coherently. A distinction is possible only in special cases, for example in kinematical regions where one of the two kinds of amplitudes is negligible with respect to the other.

In summary, to arrive at a fair comparison with $2 \rightarrow 2$ QCD, one would have to shoot for the

following goals:

1) reject widely spread multi-jet events (Mercedes-like), which are likely to be caused by hard higher order processes;
2) include in the multi–jet system clusters generated by bremsstrahlung from the final state;
3) exclude from the multi–jet system clusters generated by bremsstrahlung from the initial state.

This program can only be fulfilled to some approximation. We shall present here a comparative study, where we investigate the effect of different jet and dijet mass definitions and of different event selection criteria on the mass spectrum and on the comparison with QCD.

10.1 Definition of jet

Experimentally a jet is defined by the clustering algorithm and its parameters: the cone radius R, the candidate tower threshold E_{tow} and the seed tower threshold E_{seed}. The two tower energy thresholds are set in order to reject noise and underlying energy fluctuations.

The cone radius R is a critical parameter that can be chosen in a range of values. Changing R will change the energy attributed to the jet. This parameter is to be considered as the main knob for tuning the algorithm. For this reason it is interesting to measure the sensitivity of the mass spectrum to the cone radius R. We will examine both the Montecarlo predictions and the results of the study performed on the data.

10.2 ISAJET predictions

We used Isajet to predict the influence of gluon radiation on the leading dijet mass spectrum. This helps us in estimating the magnitude of the effect and identifying proper variables for separating initial from final radiation. The simulated leading dijet mass spectrum was compared to the final state parton mass spectrum. This was defined in terms of the parton 4–momenta before radiation. To obtain the dijet mass spectrum, the events generated by Isajet were simulated through the detector by QFL and then analyzed with the same code applied to the data [28]. The events were generated with the P_T spectrum given by $2 \rightarrow 2$ perturbative QCD.

To obtain good statistics at large masses, we generated several sets of data applying increasing P_T thresholds to the Isajet generated partons. The different sets were relatively normalized and joined together by cutting off the threshold region. Since in the analysis path we apply the cuts $|Y_{boost}|<0.4$ and $|Y^*|<0.4$ to the dijet system, for economy the Isajet partons

were generated in the limited rapidity range [-1, 1]. To check that these limits do not introduce any bias we also generated a control sample over a much larger rapidity range. Fig. 10.1 shows the parton rapidity distribution of the control sample after the Y_{boost} and Y^* cuts. It is clear that the rapidity range [-1, 1] is appropriate.

Finally, the unsmearing procedure of Chapter 7 was applied to obtain the spectrum shown in Fig. 10.2b. The points represent the simulated measurement with the statistical errors while the solid line is the $2 \rightarrow 2$ QCD calculation with EHLQ1 structure function and $Q^2=P_T^2$. While the distribution of the parent partons (fig. 10.2a) agrees with the theoretical curve (this is just a consistency check!), the dijet spectrum is significantly lower. This is to be attributed to the radiated energy that escapes the jet cone.

In the attempt of separating the final state radiation from the initial state radiation, we plotted the spatial distribution of the bremsstrahlung energy. The scatter plot in Fig. 10.3 shows the energy flux (in the η–φ space) of the gluons radiated from the final state partons. Each entry in the scatter plot refers to one gluon and it is weighted by the gluon energy; the horizontal axis represents the φ distance between the gluon and the parent parton ($\Delta\varphi = \varphi_{gluon} - \varphi_{parton}$), while the vertical axis represents the η distance. The position of the parent parton in the scatter plot is at the origin.

Most of radiation in fig. 10.3 is confined within a cone around the parent parton. This is not a surprise, because of the QCD collinear divergence, but it should be pointed out that a not negligible amount of radiation extends outside the clustering cone radius R=0.7. This radiation is responsible for the difference between the spectra in Figs. 10.2a, 10.2b .

For comparison with Fig. 10.3, Fig. 10.4 shows the same kind of plot obtained with the gluons radiated from the initial state partons. Since this time there is no obvious way of associating the bremsstrahlung gluons to one of the two final state partons, the origin of the scatter plot in Fig. 10.4 is chosen to be one of these partons, randomly selected. Fig. 10.4 shows no correlation between the initial state radiation and the final state partons. The comparison of Fig. 10.4 with Fig. 10.3 suggests that the R distance (in η-φ space) between the radiated and the leading jets is a good variable for an approximate separation between final and initial state bremsstrahlung.

Summarizing, the indications from ISAJET are:

1) the effect of gluon radiation on the dijet mass spectrum is appreciable when using a clustering cone of radius 0.7;
2) the bremsstrahlung radiation from the final state partons, though not confined within a cone of radius 0.7 around the parent parton, is nevertheless strongly correlated to the parton direction and largely contained within this radius;
3) the bremsstrahlung radiation from the initial state partons shows no correlation with the final state parton directions, and

4) as a consequence of 2) and 3) above, the R distance between the leading jets and the radiation is a useful variable to partially separate the final state radiation from the initial state radiation.

10.3 Distribution of non–leading jets in the data.

The spatial distribution of radiated gluons in ISAJET indicates that the contribution to the production of non leading jets from final state bremsstrahlung peaks around the leading jets. It is desirable to investigate the event topology in the data and make a comparison with the above Montecarlo results.

We studied in the data the spatial distribution of the third jet in the event. We plotted the position of the third jet with respect to the leading jets (the jets are numbered in order of decreasing transverse energy). In the scatter plots of Fig. 10.5 each point indicates the η–φ position of the third jet in one event (only jets with a transverse energy greater than 10 GeV are considered). The position of the first (respectively second) jet in the scatter plots is at the origin. In each plot, the other leading jet is concentrated near to the right lower corner. The depletion around the origin is obviously due to the clustering algorithm which includes in the leading jet all radiation inside R=0.7. This figure puts into evidence the arbitrariness of the cone radius choice in the definition of jets. The scatter plots in Fig. 10.5 show that the third jet is more likely to be close to the second one. The comparison of Fig. 10.5 with Figs 10.3 and 10.4 suggests that in order to investigate the effects of final state radiation on the mass spectrum one can vary the clustering cone radius. Increasing the radius will include more final state radiation, at the price of accepting more "background" from initial state radiation.

10.4 Sensitivity of M_{jj} to QCD Radiation

It is interesting to measure directly from the data the sensitivity of the dijet mass spectrum to QCD radiation. For what we said so far, a simple and effective way is to measure the variations of the mass spectrum when changing the clustering cone radius. Extending or reducing the cone means including more or less final state radiation in the definition of a jet. Performing this program literally would require running the clustering algorithm many times, which is very CPU consuming, and, more important, detailed tower information required by the clustering algorithm is not readily available on disk, but must be retrieved from the original tapes, that is a very slow process. Also, the use of larger clustering cones would imply including undesired underlying event energy in proportion to R^2. To preserve the advantage of using the data already available on disk and to avoid including more underlying event energy than necessary, we used

the technique of merging jets. The basic idea is that when a significant amount of energy is emitted outside the clustering cone, it will likely be recognized as a separate jet by the clustering algorithm. The procedure is as follows:

- We use the jets as identified by the algorithm with a cone radius 0.7.
- We select the two leading jets in E_T.
- We merge to each leading jet, by adding the 4-momenta, all non-leading jets within a cone of radius R_{cut} (in η–φ space). Then we examine how the cross section depends on R_{cut}.

Only a fraction of the whole jet data sample is used, namely 840 nb^{-1}. The distributions were not unsmeared and this gives higher cross sections [28,30]. Fig. 10.6 shows the ratio of the mass spectrum after jet merging to the mass spectrum of the two leading jets ($\sigma_{merge}/\sigma_{lead}$) for different values of R_{cut}. The effect grows up to a factor ≈ 2 for a radius $R_{cut}=1.6$. For comparison, Fig. 10.7 shows the prediction from ISAJET + QFL, obtained with the same analysis path. Although the simulation indicates a slightly larger effect on the mass spectrum, the agreement is amazingly good.

It is to be pointed out that, within the statistical errors, both the data and the simulation show a flat distribution of the ratio $\sigma_{merge}/\sigma_{lead}$ as a function of M_{jj}. This means that the radiation does not significantly affect the shape of the mass spectrum. We will take advantage of this result in the next Chapter, when comparing our data to theoretical predictions.

Note that the ratio plotted in Figs. 10.6, 10.7 is sensitive to the η dependent energy correction applied to the jets. However, the comparison with Isajet is consistent because both data and simulation were treated in the same way.

10.5 ISAJET vs. HERWIG

To gain a deeper insight into the value of the indications based on Montecarlo, we further investigated the dynamical information contained in the scatter plots of Fig. 10.5. We looked for variables exhibiting dynamical properties that could be easily compared with Montecarlo predictions. This would allow checking that the main physics features are under control. What we do is:

a) We change the coordinates in the scatter plot of Fig. 10.6 from the "cartesian" ($\Delta\varphi$, $\Delta\eta$) to the "polar" (R,α), and we define the density as a function of the new coordinates: $\sigma(R,\alpha) = r\,(\Delta\varphi, \Delta\eta)$ ($\alpha=0$ on the $\Delta\eta=0$ axis).

b) We study the dependence of σ on R, integrating over α the density in each annulus: $\int\sigma(R,\alpha)d\alpha$ (Fig 10.8).

c) We study the dependence of σ on α, integrating the density in R over α–sectors: $\int\sigma(R,\alpha)RdR$ (Fig 10.9).

The solid lines in Figs. 10.8 and 10.9 represent the real data while the dashed lines represent the Montecarlo predictions. In addition to the ISAJET sample we also generated a sample with HERWIG[31], because this Montecarlo handles radiation in a different and more sophisticated fashion. As a matter of fact, the R distribution is steeper in ISAJET than in HERWIG, that appears to fit the data a bit better. But the difference in the α distribution is obvious: the data show an enhancement of the density as α approaches 90° that is not seen in ISAJET while it is reproduced very well by HERWIG. By recalling the definitions of the variables in Fig. 10.5, one sees that $\alpha \approx 90°$ means that jet 3 is close to the plane defined by the second jet and the beam axis (which is the plane identified by $\Delta\varphi = 0$).

This suggests that the enhancement may come from an effect of interference between coherent color radiation from initial and final state partons [31]. This hypothesis is supported by the fact that one major difference between ISAJET and HERWIG is that the latter tries to take into account coherence effects in radiation while the former does not. Actually, this subject may be interesting enough to be worth a detailed study for its own sake.

However, the conclusion we want to draw here is that the agreement of the simulation with the data is adequate for supporting the significance of our measurement and for a rough estimate of the effect of radiation.

Actually, our data are detailed enough to probe the theory at a deeper level than the $2\rightarrow2$ scattering scheme. A full exploitation of the information contained in our measurement will only be possible on comparing with higher order calculations (and corresponding Montecarlos).

10.6 Sensitivity to the $\Delta\varphi$ Cut

Entangled with the problem of gluon radiation is the question of multijet events from hard higher order QCD diagrams. When comparing the measured mass spectrum to the $2\rightarrow2$ QCD calculation, these multijet events are considered as a background. Higher order processes are already suppressed by a factor α_s, but to further reject multijet events we required the two leading jets to be back to back within 20° in the transverse plane ($\Delta\varphi = |\varphi_1 - \varphi_2| < 20°$) [28]. This is actually only a bland attempt at separating two jet events. For obvious kinematical reasons the $2\rightarrow2$ QCD calculation predicts $\Delta\varphi = 0$, while requiring $\Delta\varphi = 0$ in the real data would leave, of course, no events.

This amounts to stating, once more, that the $2\rightarrow2$ QCD calculation does not take into account gluon radiation (even if the detector resolution also contributes a small $\Delta\varphi$ spread). For this reason it is not clear what the best value for the $\Delta\varphi$ cut is, and it is probably desirable to

keep it loose. At any rate, it is necessary to check the sensitivity of the cross–section to the cut. Verification of results and comparison to theory will rely again on Montecarlo simulation.

We measured the mass spectrum for different values of the $\Delta\varphi$ cut, namely 10°, 20°, 30°, and 180° (that is no cut). The spectrum obtained with no cut was used as a reference. We then calculated the fractional differences $(\sigma_{cut}-\sigma_{nocut})/\sigma_{cut}$. The results (interpolated) are shown in Fig. 10.10. One observes that the shape of the mass spectrum depends on the $\Delta\varphi$ cut, although not dramatically. The standard cut $\Delta\varphi < 20°$ that was adopted for most of the analysis reduces the cross section at low masses by about 20%. This shows that we should not attach too much importance to the lower end of the spectrum when comparing the data to theory.

10.7 Summary

The presence of gluon radiation complicates the comparison between the measured dijet mass spectrum and the theoretical predictions. In particular the comparison with the $2\rightarrow2$ QCD calculation, that is in principle the simplest verification to be done, becomes delicate when one requires enough accuracy that gluon bremsstrahlung becomes important. The mass spectrum is less inclusive than the single jet E_T spectrum, is sensitive to QCD radiation, and the result depends on the cuts used to select the events ($\Delta\varphi$) and to identify radiation (R_{cut}).

If on one side this makes the experimenter's life harder, on the other hand it allows a deeper probing of the theory. In this situation, our attitude can be summarized as follows:

1) We measure the differential cross section $d\sigma/dM_{jj}$ with specified parameters and cuts. To this purpose we operatively defined the jet as the set of all particles exiting the primary vertex within a cone of fixed size. No attempt was made to reconstruct the energy of the original parton by means of "out–of–cone" corrections.
2) We make a first comparison with the prediction from $2\rightarrow2$ QCD calculations, without taking gluon radiation into account. In the near future more and more detailed QCD predictions will be available, in particular from fully consistent higher order calculations. When theoretical predictions of the energy flux within cones of given size will be available, the comparison with this measurement will be more accurate. This would be impossible if out of cone corrections based on present models had been applied to the jet energy.
3) We measured the sensitivity of the mass spectrum to the $\Delta\varphi$ and R_{cut} cuts. This gives a quantitative assessment of the size of the effects of gluon radiation.
4) While waiting for more accurate QCD predictions, we started detailed comparisons of the data with the ISAJET and HERWIG shower Montecarlos. This also allows a comparison between ISAJET and HERWIG, using variables which put the different

dynamical approaches adopted by the two programs into evidence.

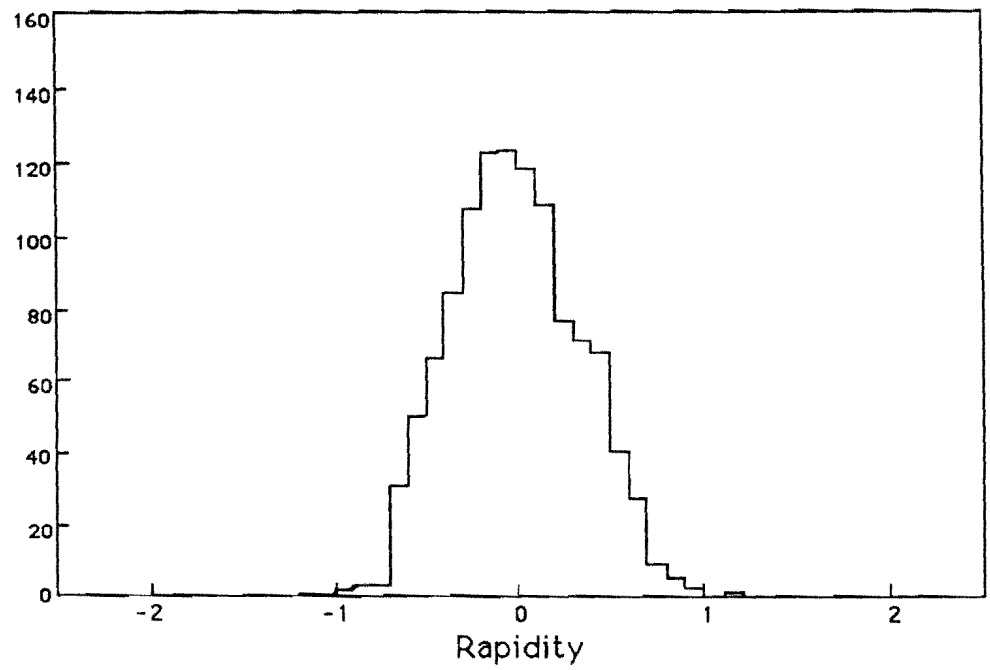

Fig 10.1 Rapidity of partons generating central jet pairs ($|Y_{boost}|$, $|Y^*|<0.4$)

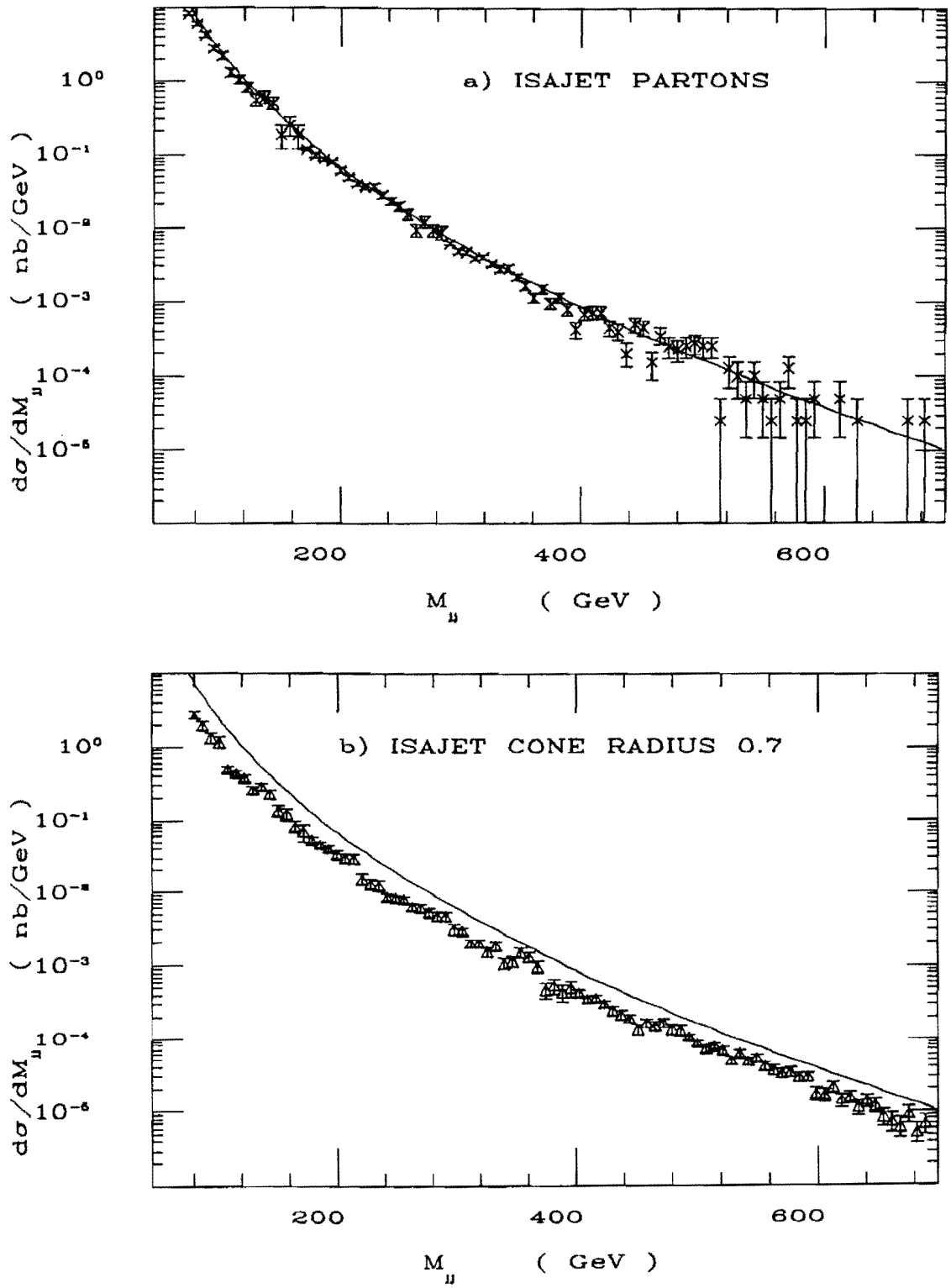

Fig 10.2 M_{jj} spectrum of partons (a) and jets of radius 0.7 (b) according to ISAJET

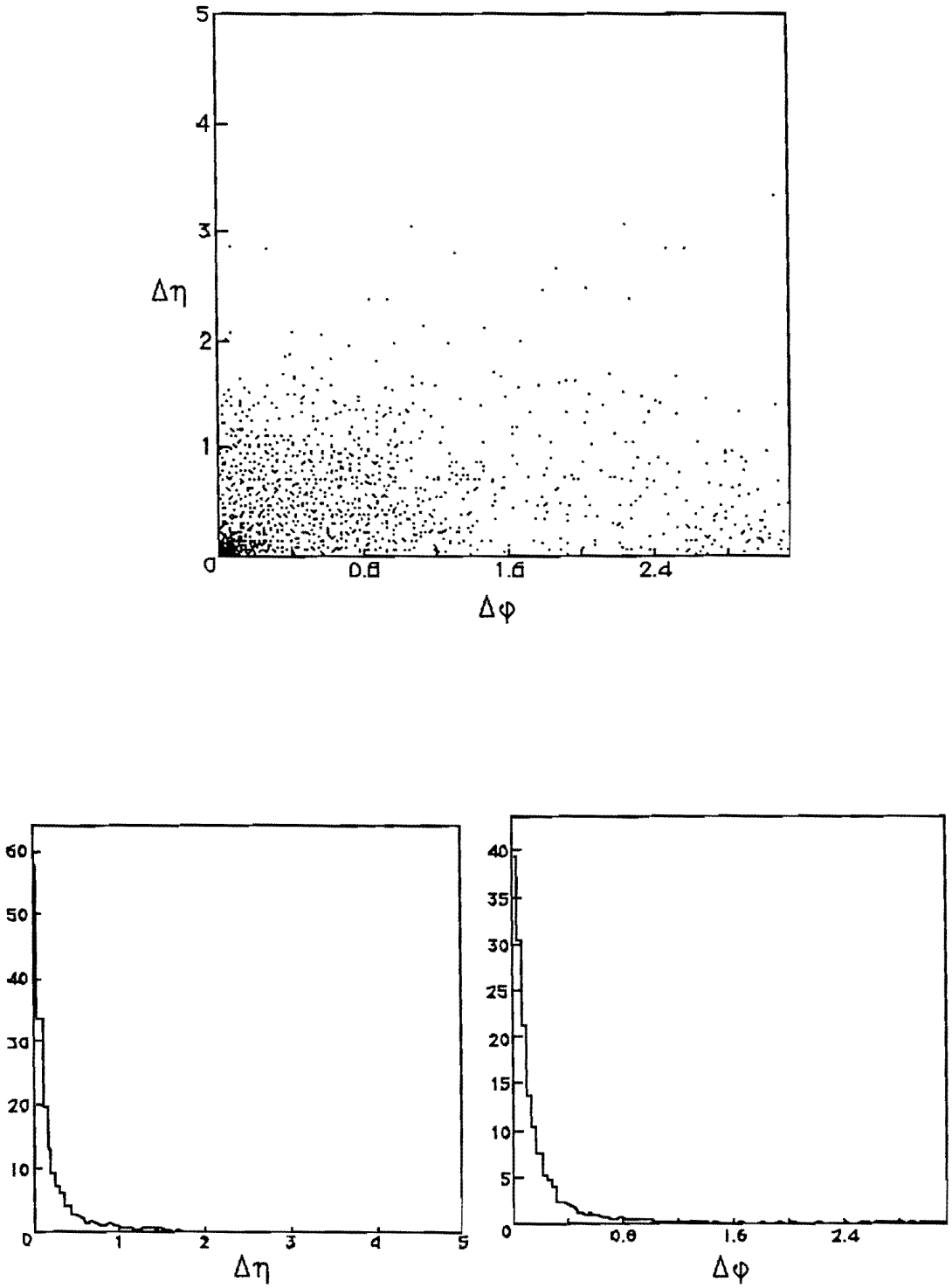

Fig 10.3 $\Delta\varphi$ vs. $\Delta\eta$ for gluons radiated by final state partons

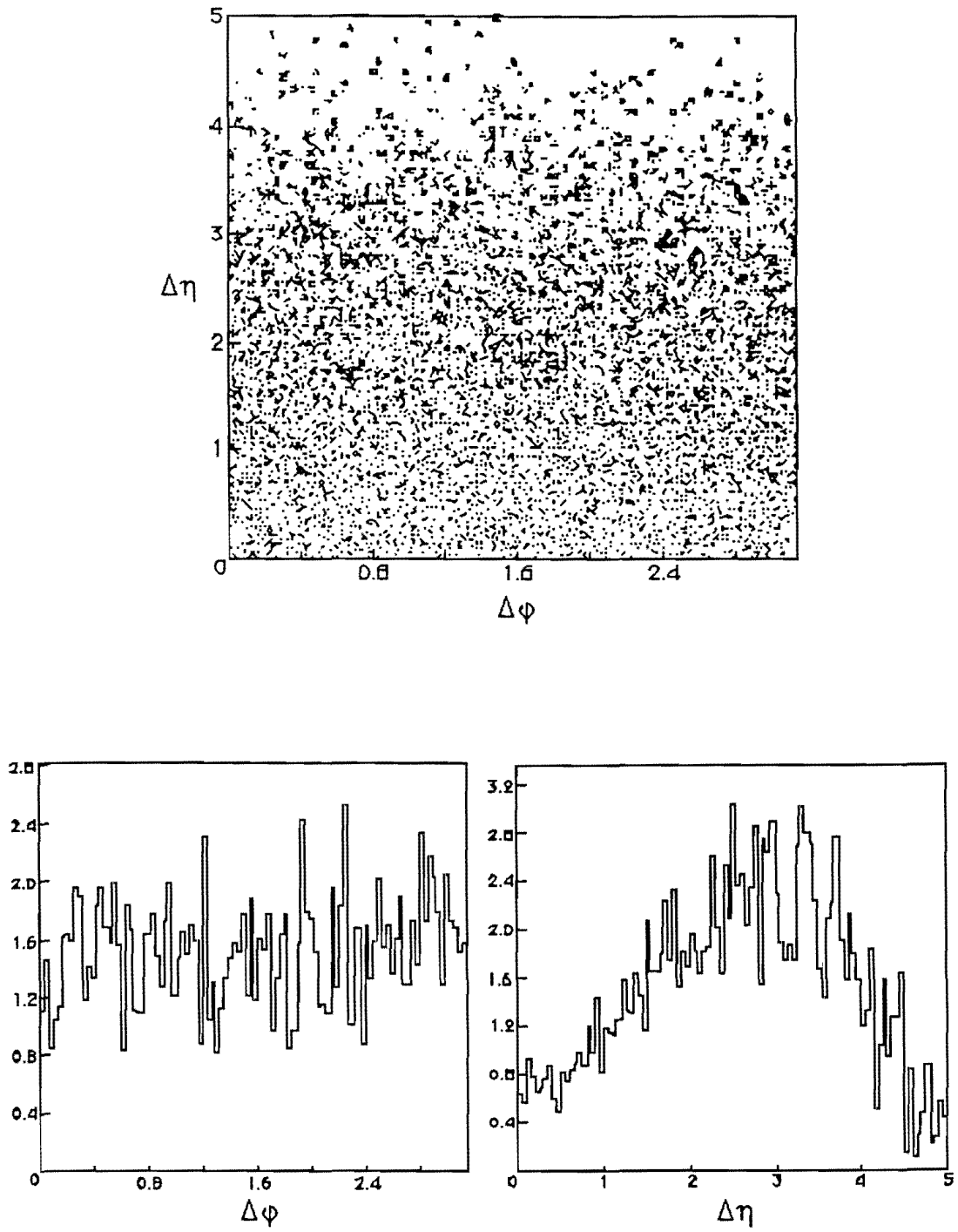

Fig 10.4 $\Delta\varphi$ vs. $\Delta\eta$ for gluons radiated in the initial state. The distance is taken from a randomly chosen final parton

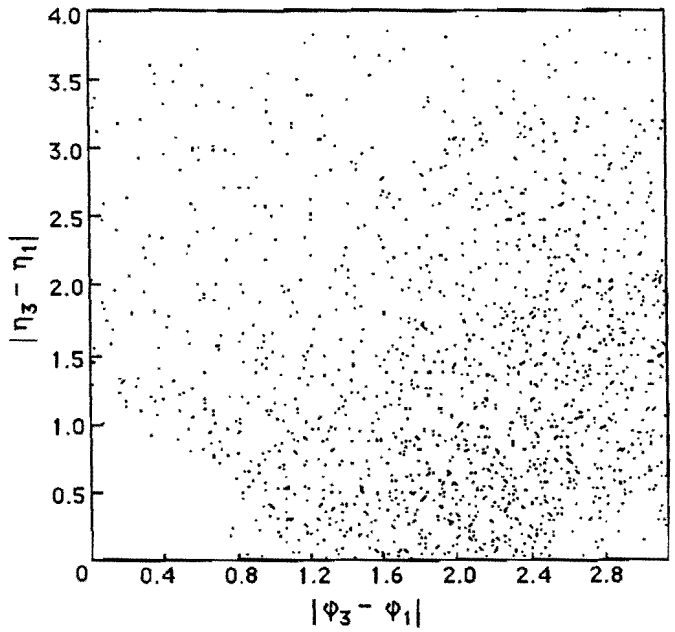

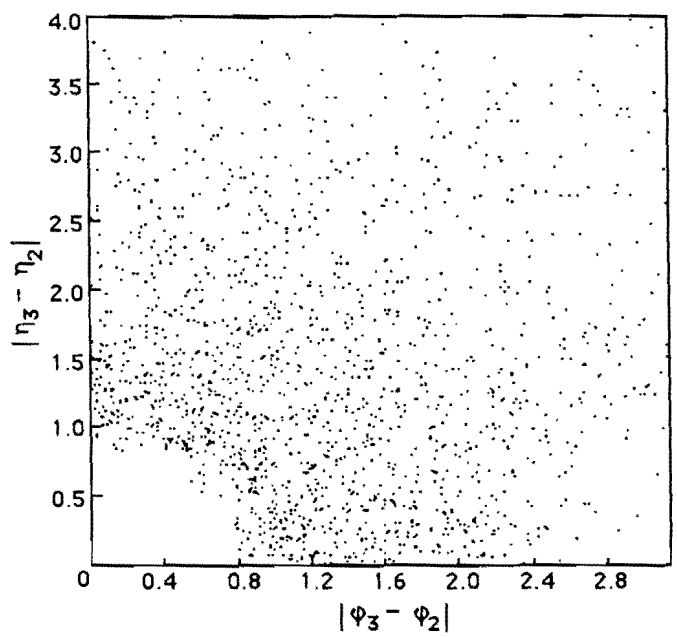

Fig 10.5 $\Delta\varphi$ vs. $\Delta\eta$ of jet 3, relative to jet 1 (top) and jet 2 (bottom)

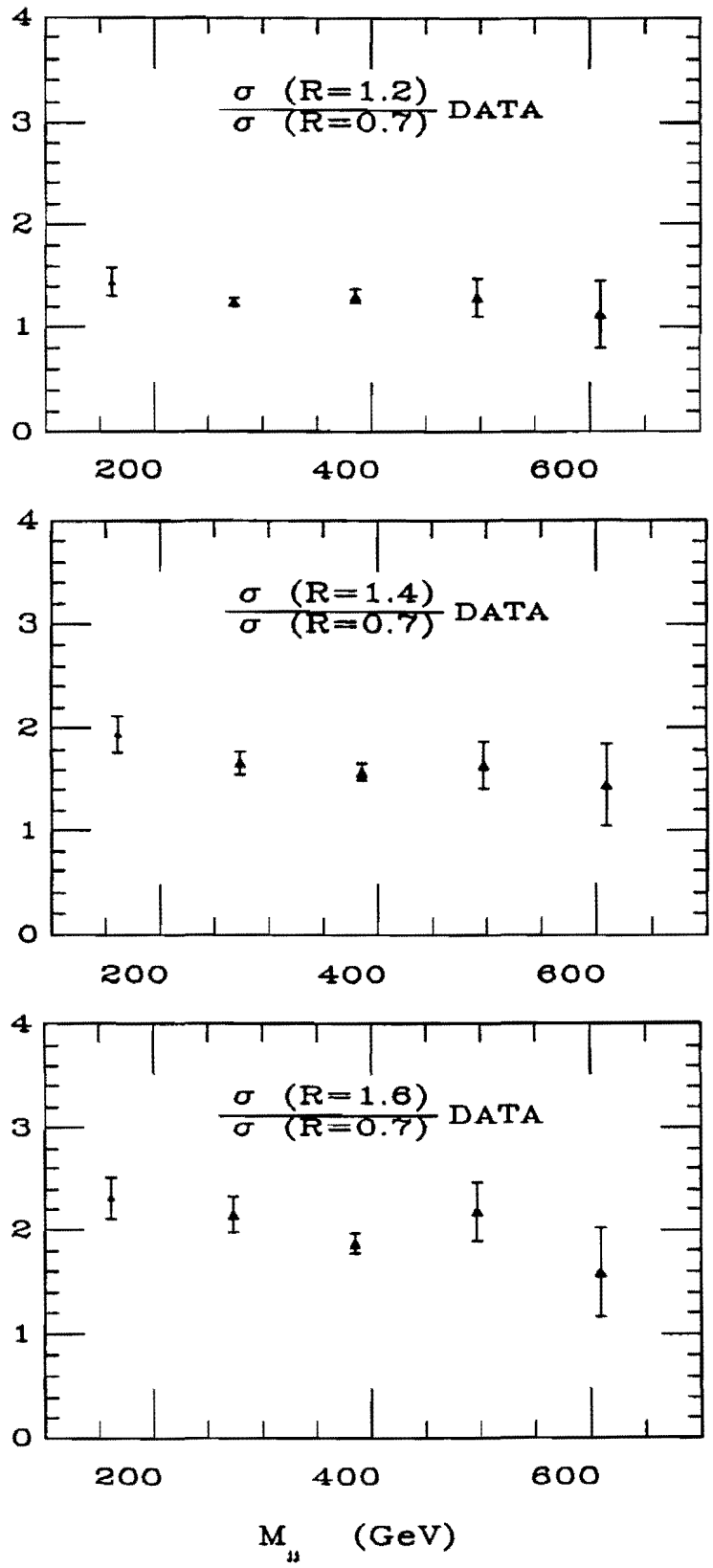

Fig 10.6 Ratio of M_{jj} spectra with different merging radii to the unmerged spectrum (data)

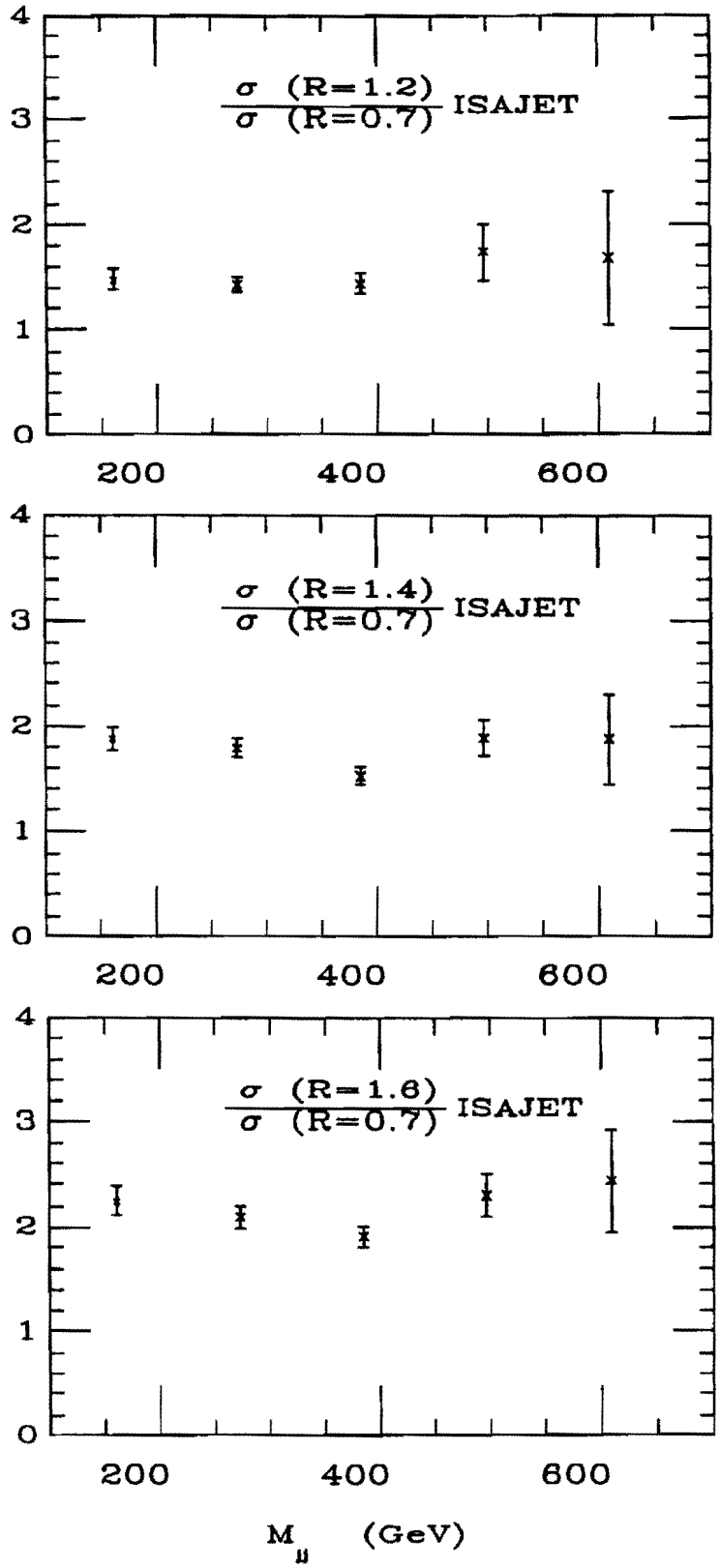

Fig 10.7 Ratio of M_{jj} spectra with different merging radii to the unmerged spectrum (ISAJET)

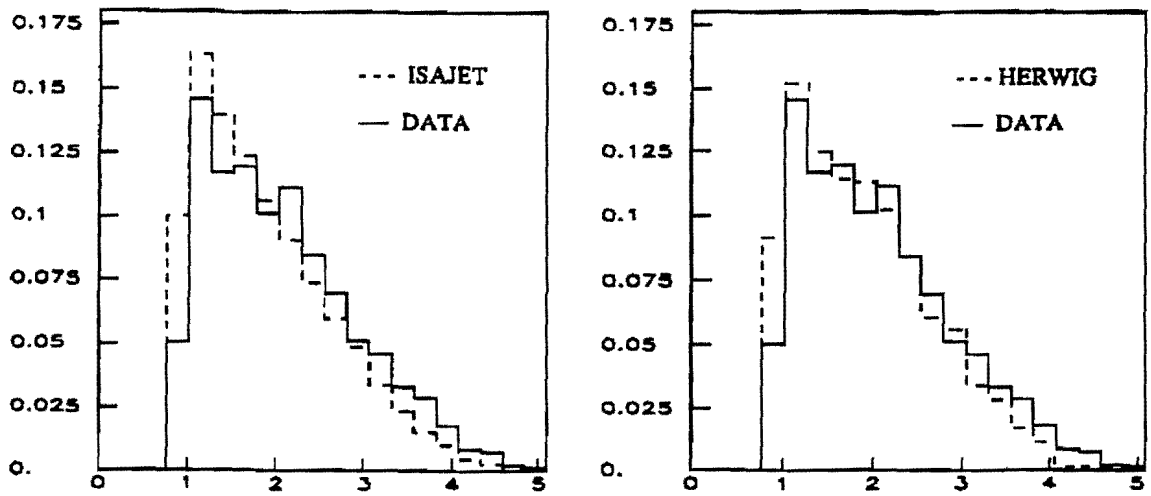

Fig 10.8 R distribution compared to ISAJET and HERWIG predictions

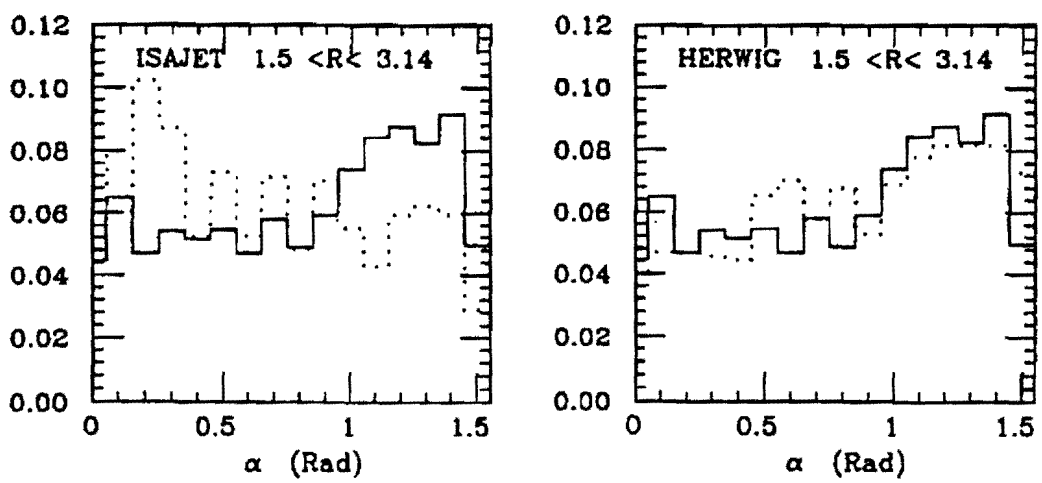

Fig 10.9 α distribution compared to ISAJET and HERWIG predictions

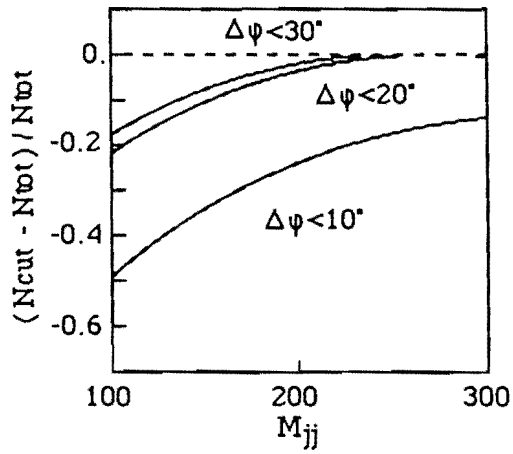

Fig 10.10 Effect of $\Delta\varphi$ cut on the M_{jj} spectrum

CHAPTER 11

Comparing data and theory

11.1 Absolute Comparison to Leading Order QCD

We calculated the theoretical predictions from 2→2 QCD diagrams [32], varying the Q^2 scale within the range $0.5\ P_T^2 \div 2\ P_T^2$ and using different parametrizations for the parton structure functions, namely DO1, DO2, EHLQ1, EHLQ2. The results are summarized in the band shown in Fig.11.1, representing the envelope of all predictions for different Q^2 and structure functions. This is compared to our data corrected for experimental resolution (as described in Chapter 8) on an absolute scale. Error bars are statistical only. A single bar is drawn on a side to indicate the size of the systematic uncertainty.

It is seen that our data are consistent with the theoretical band over the whole mass range, although lying somewhat on the lower edge of the predictions. As a matter of fact, according to the discussion of the previous Chapter, we should expect the data to be lower than the prediction due to the effect of gluon radiation, that is not taken into account in this comparison. Had we used a Montecarlo calculation in place of the theoretical calculation, or had we used the jet cone which is suggested by the Montecarlo (≈ 1) , the data point would be better centered within the band.

To go beyond this level of accuracy it is probably necessary to wait for a next–to–leading QCD calculation, similar to that already available for the E_T spectrum, which depends explicitly on the cone size and is much less sensitive to the Q^2 scale[33].

In the meantime, we can take advantage of the indication from the Montecarlo that the radiation does not affect the shape of the spectrum to proceed in the comparison by normalizing the theory to the observed spectrum.

11.2 Relative Comparison to Leading Order QCD

We account for the radiation effect by multiplying the theory by a normalization constant θ, determined by fitting the data. Unfortunately, since the difference between predictions at different Q^2 scales is not simply a multiplicative factor, we cannot absorb it in the same

constant. This effect can be seen in Fig.11.2, where the ratio between predictions at different Q^2 scales is plotted versus M_{jj}. It appears that the shape of the spectrum can change by up to 25% within the considered Q^2 range. Therefore, we look for the best fit to our data by varying independently θ, Q^2, and structure functions.

A point to be considered with care is how to take into account systematic uncertainties. One might be tempted to conclude that, since our systematic error is essentially a constant fraction (≈30%) of the cross section over the whole range, it is automatically absorbed into the normalization constant. This would be true if the systematic deviations in two different bins were totally correlated. This happens when the systematic uncertainty comes from a single source. An example of systematic error of this kind is the luminosity uncertainty: whatever error we make in estimating the value of the luminosity, all data points move together, up or down, by the same factor. Our systematic uncertainty comes instead from a number of almost independent sources, and the single contributions are not constant versus M_{jj}. The total uncertainty comes out to be a constant only by chance.

A quick–and–dirty solution would be to make the opposite assumption that the systematic errors are completely uncorrelated, namely to add them in quadrature to the statistical errors. Indeed, a systematic error with no bin–to–bin correlation is not really systematic, but rather statistical. This is not a good approximation in our case, and has the only advantage of being conservative. Actually, it is so conservative that it would deteriorate substantially the discriminating power of the comparison.

In our work we assume the systematic deviations from any individual source to be completely correlated, but the different contributions to be independent from each other. Hence we evaluate the error matrix according to the formula:

$$S_{ij} = \sum_{\alpha} \sigma_i^{sys}(\alpha)\sigma_j^{sys}(\alpha) + \delta_{ij}(\sigma_j^{stat})^2$$

where i,j run on the bins, α runs on the different systematic errors and δ_{ij} is the Kronecker delta. The statistical error is estimated as the square root of the bin content.

From this matrix the χ^2 is calculated as:

$$\chi^2 = \sum_{ij} (f(x_i) - y_i)\, S_{ij}^{-1}\, (f(x_j) - y_j)$$

where y_i are the data points and $f(x_i)$ the corresponding value of the fitting function. This expression reduces to the usual:

$$\chi^2 = \sum_i \frac{(f(x_i)-y_i)^2}{\sigma_i^2}$$

when the systematic errors are zero[1] .

This χ^2 is a quadratic function of θ and its minimum is readily found with simple linear algebra.

We have performed this calculation using a number of different Q^2 values and structure functions (Tab. 11.1). In doing this, we excluded the data points below 200 GeV, because they are suspected to be significantly affected by several additional uncertainties (like uncertainty in the smearing correction and collinearity cut). It turns out that the χ^2 values are all similar, that means the shape differences between the various choices are not much larger than the possible distortions of the experimental distribution due to our systematic effects. However, there is a general tendency for the χ^2 to increase when moving rightward and downward in the Table. The best agreement is obtained at $Q^2=0.5*P_T^2$ with DO2 structure functions: $\chi^2=44.3$ with 35 degrees of freedom[2] (we count the structure function choice as an additional continuous parameter). This curve is shown superimposed to our data in Fig. 11.3. A linear plot of the fractional difference between data and theory is also shown in Fig.11.4. From the plots the curve appears to fit the data well. The only anomalous features that could be noticed are an isolated high point at $M_{jj} \approx 610$ GeV and a slight negative deviation at the low end (that is easily explained by the effects discussed in the previous Chapter). The high point is 2.9 σ above the fitting curve, if we estimate σ from its bin content, or 3.87 σ if we estimate σ from the bin content expected from QCD. Since its contribution to the global χ^2 is sizable, we have repeated our fits by limiting the χ^2 calculation to the mass region lower than this bin. The results, listed in Tab. 11.2, show a smaller χ^2 in all cases, but the dependence on the parameters is substantially unchanged. We conclude that the global agreement with QCD is not affected by the presence of this deviating bin. We will see that this will instead complicate our tests for a possible compositeness effect. The problem of the cause of this deviation is an open matter. The likelihood of a random fluctuation of that size in a given bin is of the order of 10^{-4}. It follows that the likelihood of finding at least one such fluctuation in an histogram like ours is $\approx 0.5\%$. On the other hand, all events in that region were visually scanned, and all of them appear to be honest dijet events. In conclusion, we think than no definite conclusion can be drawn until the data of the next run will be available, that are expected to increase the statistics of a factor ≈ 5. For this reason, we will test the high mass tail for compositeness–like effects both by including and excluding this point. We will see that this does make a difference.

[1] Note that the above defined χ^2 variable is actually distributed according to a χ^2 distribution only if the expected bin contents are not too small.

[2] This result should not be taken as evidence in favor of this structure functions choice, since other structure functions also give reasonable χ^2 values. In this context, the choice of the best χ^2 has no other meaning than that of best parametrization of our systematic deviations. Note that it has been pointed out that DO2 cannot be valid at high Q^2 [35].

11.3 Testing for Quark Compositeness

We have repeated the analysis of the preceding paragraph by adding a compositeness term at a mass scale Λ, in the range 900 ÷ 2000 GeV. Since two choices are possible for the sign of the contact term, we have used the sign that gives destructive interference with QCD. This gives a slightly lower excess of cross section than the other choice, yielding a more conservative limit. The resulting χ^2 are reported in Tab. 11.3, limiting the choice to $Q^2=0.5*P_T^2$ that gives the lowest values. We notice that the dependence on the choice of structure functions is similar to what obtained with pure QCD. The best fit is obtained with DO2 at Λ=1.5 TeV (Figs. 11.5 and 11.6), giving a χ^2=43.03 with 35 degrees of freedom. Comparing this to the value χ^2=44.3 obtained from pure QCD, we see that the improvement is not statistically significant, and cannot justify the introduction of an additional parameter. Even clearer results are obtained by excluding the last three points, like we did in the previous paragraph. In this case the best choice for Λ lies beyond 2000 GeV. In fact, it appears clearly from the plots that the value Λ=1.5 TeV is mainly determined by the single high bin at 610 GeV: all other bins are excellently described by the QCD curve.

However, a deeper investigation is possible. Since the presence of an internal structure of quarks manifests itself only when M_{jj} approaches the compositeness scale, our tests are mostly influenced by the high mass region, where the statistics is low. This implies that our assumption of Gaussian fluctuations with variance equal to the bin content, used in the χ^2 test, is not a good approximation. Therefore, we have performed a more careful test by normalizing the theory to the data below an intermediate mass value, and performing a likelihood ratio test with the data in the upper mass range. To do this, it is necessary to work on the raw bin contents, uncorrected for resolution smearing, and to smear the theoretical curve instead. However, we will keep displaying in the plots the unsmeared data with the plain theoretical curve for convenience.

The lower region is used to normalize the theoretical curves, using the linear fit already described. We perform a fit to the upper region by maximizing the likelihood of obtaining our data set by varying the available parameters, for both the QCD and compositeness curves. Then we form the likelihood ratio:

$$\lambda = \frac{\max L(y|f(Q^2,\text{str. f.},\infty))}{\max L(y|f(Q^2,\text{str. f.},\Lambda))}$$

where $L(y|f)$ is the likelihood of obtaining our data set y if the parent distribution is f.

Then, if QCD is true, the quantity:

$$-2\log(\lambda)$$

follows a χ^2 distribution with a number of degrees of freedom equal to the number of

additional free parameters in the alternative theory (one: Λ).

In practice, instead of evaluating the maximum likelihood we evaluate the minimum of the quantity:

$$\xi^2 = -2\log\left[\frac{L(y|f(Q^2,\text{str. f.},\Lambda))}{L(y|y)}\right]$$

where $L(y|y)$ is the likelihood of our data set if the expected values were equal to the observed ones.

From this we get:

$$-2\log(\lambda) = \xi^2(\text{QCD}) - \xi^2(\text{Comp.}).$$

Since the bin contents are Poisson distributed, ξ^2 can be written as :

$$\xi^2 = 2\sum_{i=1}^{n}\left\{[f(x_i)-y_i] + y_i\log\left(\frac{y_i}{f(x_i)}\right)\right\}.$$

The systematic errors are neglected, both because they are partially canceled by the fit to the lower region and because the statistical errors are dominant at these large masses.

The ξ^2 value provides additional information about the goodness of the fit for each curve, independently of the comparison with the other one. In fact, it can be proven that, if the expected bin contents are not too small, the distribution of this quantity is also a χ^2 distribution, with a number of degrees of freedom equal to the number of bins minus the number of free parameters [34].

Note that no such condition is required for the likelihood *ratio* to have a χ^2 distribution, therefore the corresponding test can be performed also with very narrow bins.

We have chosen to split our data set at M_{jj} = 400 GeV. This gives 28 bins in the lower range and 10 bins in the upper range. Tab. 11.4 shows the χ^2 values evaluated in the normalization region, and the ξ^2 in the upper tail for different values of Λ. Only the data obtained with DO2 structure functions and $Q^2=0.5P_T^2$ are listed, since all other choices give equivalent or worse results. The minimum values of ξ^2 are 25.23 for QCD and 15.83 for compositeness, obtained for Λ=1.15 TeV. The difference is $-2\log(\lambda)$=9.4 with 1 degree of freedom, that means QCD would be excluded at the 95% confidence level. However, this result has little meaning because the agreement with the compositeness prediction, taken by itself, is also bad: ξ^2=15.83 with 7 degrees of freedom is excluded at the 95% CL, too.

In fact, it appears (Figs. 11.7÷11.10) that the statistical preference for compositeness is almost exclusively due to the single bin at 610 GeV, and not to a global excess of cross section in the tail of the spectrum that would be produced by a contact term in the Lagrangian.

We have repeated our analysis after excluding this bin from the calculations (Tab. 11.4, third column). In this case we obtain the minimum values ξ^2=9.39 for QCD and ξ^2=7.61 for Λ=1.40 TeV (Fig. 11.11,11.12). This time both fits are good and the resulting likelihood ratio $-2\log(\lambda)$=1.33 with 1 degree of freedom gives no evidence for compositeness.

11.4 Lower limit to the compositeness scale

From the data in Tab. 11.4 a lower limit for the compositeness scale can be obtained. If compositeness exists at scale Λ, then the likelihood ratio between Λ and the value Λ_{fit} found by maximizing the likelihood

$$\xi^2(\Lambda) - \xi^2(\Lambda_{fit}) = -2\log\left[\frac{L(y|f(\Lambda))}{L(y|f(\Lambda_{fit}))}\right]$$

follows the χ^2 distribution with 1 degree of freedom. Therefore, the probability for Λ to have a value such that $\xi^2(\Lambda)-\xi^2(\Lambda_{fit}) < \alpha$ can be calculated for any α. By inverting this procedure we have the standard method for finding a confidence interval around the estimate Λ_{fit}. Given the required confidence level, α can be found in the χ^2 distribution tables (for instance, 95% C.L. yields α=3.841), and the Λ range is determined by $\xi^2(\Lambda) < \xi^2(\Lambda_{fit}) + \alpha$ (see Fig. 11.13). However, our situation is somewhat different, since the line $\xi^2(\Lambda) = \xi^2(\Lambda_{fit}) + \alpha$ intersects our curve only in one point, due to the fact that, on the right side, $\xi^2(\Lambda)$ is always lower than (and tends asymptotically to) ξ^2(QCD). Therefore, we need to work with two values α_1, α_2 rather than one, one of them being fixed by $\xi^2(\Lambda_{fit}) + \alpha_2 = \xi^2(QCD)$, and determine the other α_1 in order to have

$$1/2P(\chi^2<\alpha_1) + 1/2P(\chi^2<\alpha_2) = C.L.$$

In addition, our test should be unilateral rather than bilateral, because we are considering only excesses of cross–section over QCD. This is easier to see by taking, say, $1/\Lambda$ as the fit parameter in place of Λ. Then it appears natural to extend the curve to negative values of $1/\Lambda$, by formally interpreting a negative Λ as corresponding to a negative rather than positive deviation from the QCD cross–section. Since negative deviations are excluded by physics in our case, the probability of a "negative Λ" must be set to zero and all other probabilities must be renormalized by dividing by $[1- 1/2*p(\chi^2>\xi^2(QCD)-\xi^2(\Lambda_{fit})]$. Putting all together, the lower limit Λ_{min} at the confidence level CL turns out to satisfy the equation:

$$p(\chi^2>\xi^2(\Lambda_{min})-\xi^2(\Lambda_{fit})) = (2-p(\chi^2>\xi^2(QCD)-\xi^2(\Lambda_{fit}))*(1-CL)$$

Hence, by putting CL=95% :

$$p(\chi^2>\xi^2(\Lambda_{min})-\xi^2(\Lambda_{fit})) = 1.75*0.05 = 0.0875$$

$$\xi^2(\Lambda_{min})-\xi^2(\Lambda_{fit}) = 2.8$$

we can see from Fig. 14 that this corresponds to

$$\Lambda_{min} = 1.13 \text{ TeV}$$

By including bin 53, we would find with the same procedure a $\approx$100GeV lower Λ_{min}, but this lower limit would bring along also an *upper* limit. Yet, the fact that the lower limit is almost unaffected is, in a way, reassuring.

By performing the same analysis with the opposite sign for the contact term (constructive interference with QCD), we get $\approx$50 GeV higher limits.

11.5 Conclusions

Using the central jet data of the 1988-1989 CDF run ($\int Ldt = 4.6pb^{-1}$), we found that $2\rightarrow2$ QCD describes adequately the jet–pair mass distribution up to masses of $\approx$800 GeV. A lower limit to the compositeness scale Λ_c>1.1 TeV was derived.

A more detailed comparison to QCD will be possible when α_s^3 cross–section calculations will become available.

In the next CDF run, a factor 5 increase in statistics is expected, which will allow probing QCD to still higher Q^2.

Q^2/P_T^2	Structure function			
	D01	D02	EHLQ1	EHLQ2
0.5	44.44	44.30	45.49	47.25
0.7	44.55	44.73	46.17	47.93
1.0	45.32	44.84	47.31	48.82
1.3	45.67	45.00	48.64	49.60
2.0	46.12	45.93	50.91	51.14

Tab 11.1 χ^2 dependence on Q^2 scale and structure function for the QCD fit to our data (M_{jj}>200 GeV), with 35 d.o.f.

Q^2/P_T^2	Structure function			
	D01	D02	EHLQ1	EHLQ2
0.5	35.88	35.55	36.46	37.69
0.7	35.94	35.89	37.04	38.30
1.0	36.69	35.90	38.08	39.11
1.3	36.99	36.00	39.31	39.82
2.0	37.35	36.81	41.43	41.23

Tab 11.2 Same as Tab. 11.1, after excluding the 3 highest bins from the fit (32 d.o.f.).

Λ	Structure function			
	D01	D02	EHLQ1	EHLQ2
900	67.15	54.93	63.77	62.68
1000	56.65	48.65	53.82	52.73
1100	49.76	45.43	47.76	47.33
1200	46.30	44.13	44.63	44.99
1300	44.00	43.15	43.70	44.25
1400	43.49	43.33	43.70	44.24
1500	43.32	43.03	43.51	44.52
1600	43.63	43.42	43.50	44.88
1800	43.50	43.85	44.15	45.55
2000	43.82	43.97	44.53	46.05

Tab 11.3 χ^2 for compositeness fits (35 d.o.f.)

Λ	χ^2	ξ^2	ξ^2 No bin 53
900	30.73	33.85	33.52
950	30.18	24.99	23.77
1000	29.93	20.00	17.61
1050	29.89	17.38	13.76
1100	29.76	16.18	11.30
1150	29.56	15.83	9.77
1200	29.75	15.90	8.74
1250	29.79	16.35	8.19
1300	29.48	16.94	7.86
1350	29.53	17.63	7.76
1400	29.47	18.20	7.61
1450	29.48	18.96	7.75
1500	29.33	19.40	7.66
1550	29.33	19.94	7.72
1600	29.47	20.51	7.89
1650	29.35	21.00	8.00
1800	29.56	22.05	8.21
2000	29.62	23.22	8.66
QCD	29.44	25.23	9.39

Tab 11.4 χ^2 (25 d.o.f.) and ξ^2 (7 and 6 d.o.f.) for compositeness fits to the upper tail.

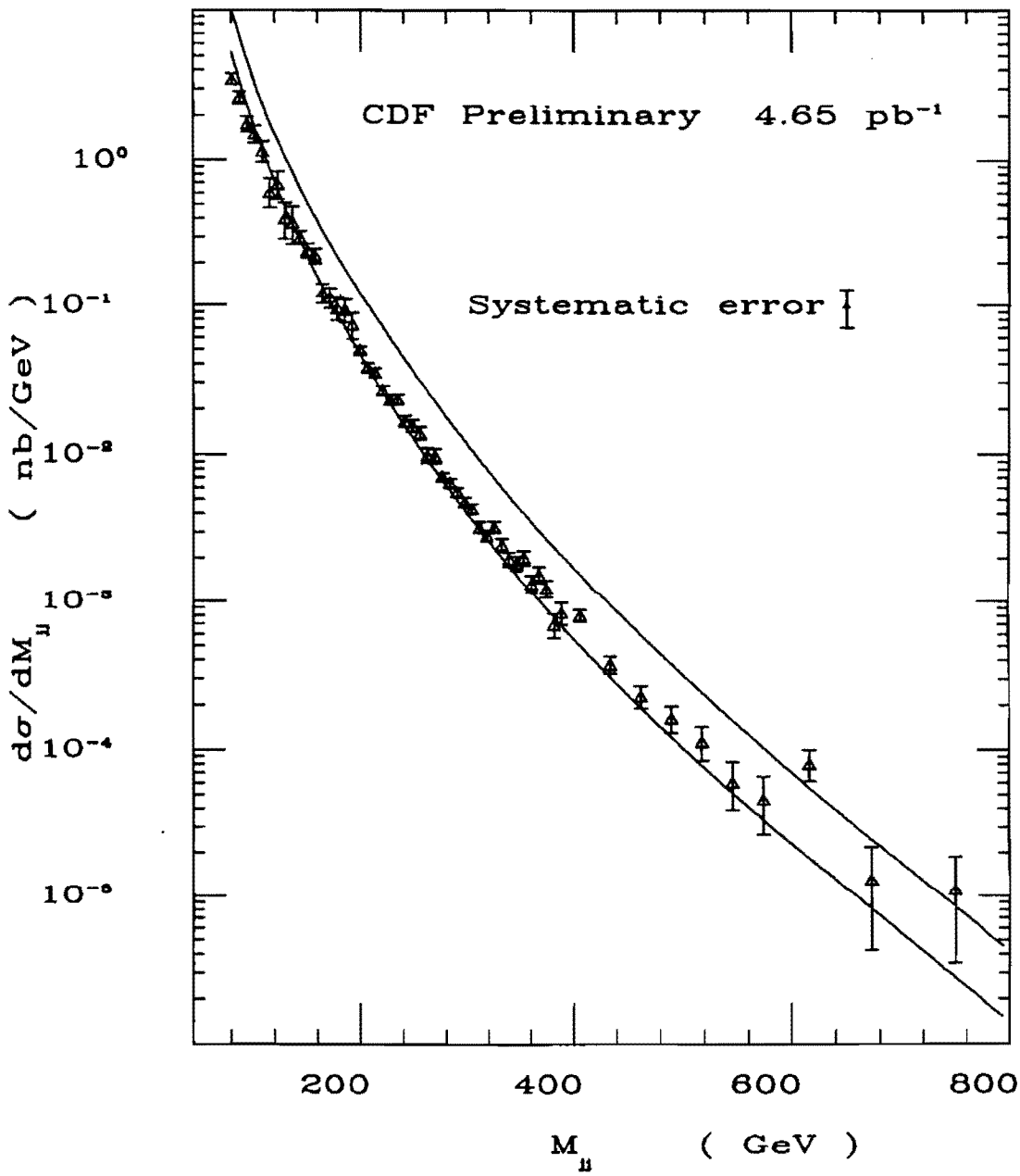

Fig 11.1 Absolute comparison between CDF data and QCD. The band is the envelope of all structure functions and Q^2 choices described in the text.

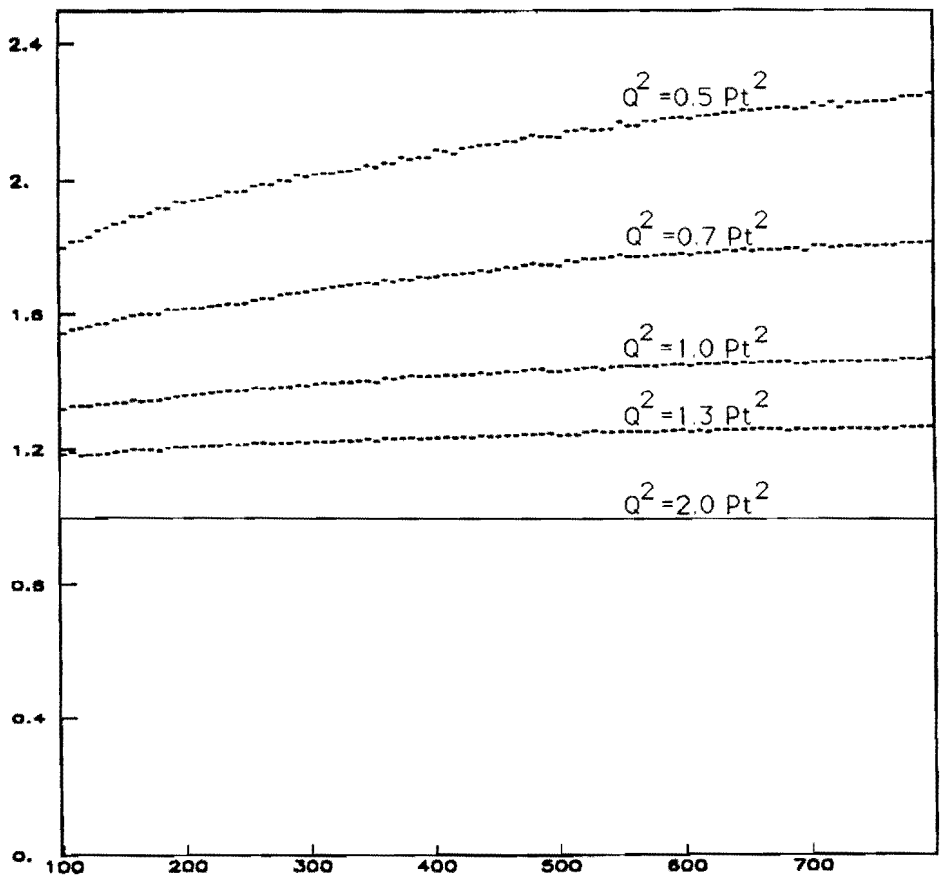

Fig 11.2 QCD curves with different Q^2 choices, normalized to $Q^2 = 2.0P_T^2$.

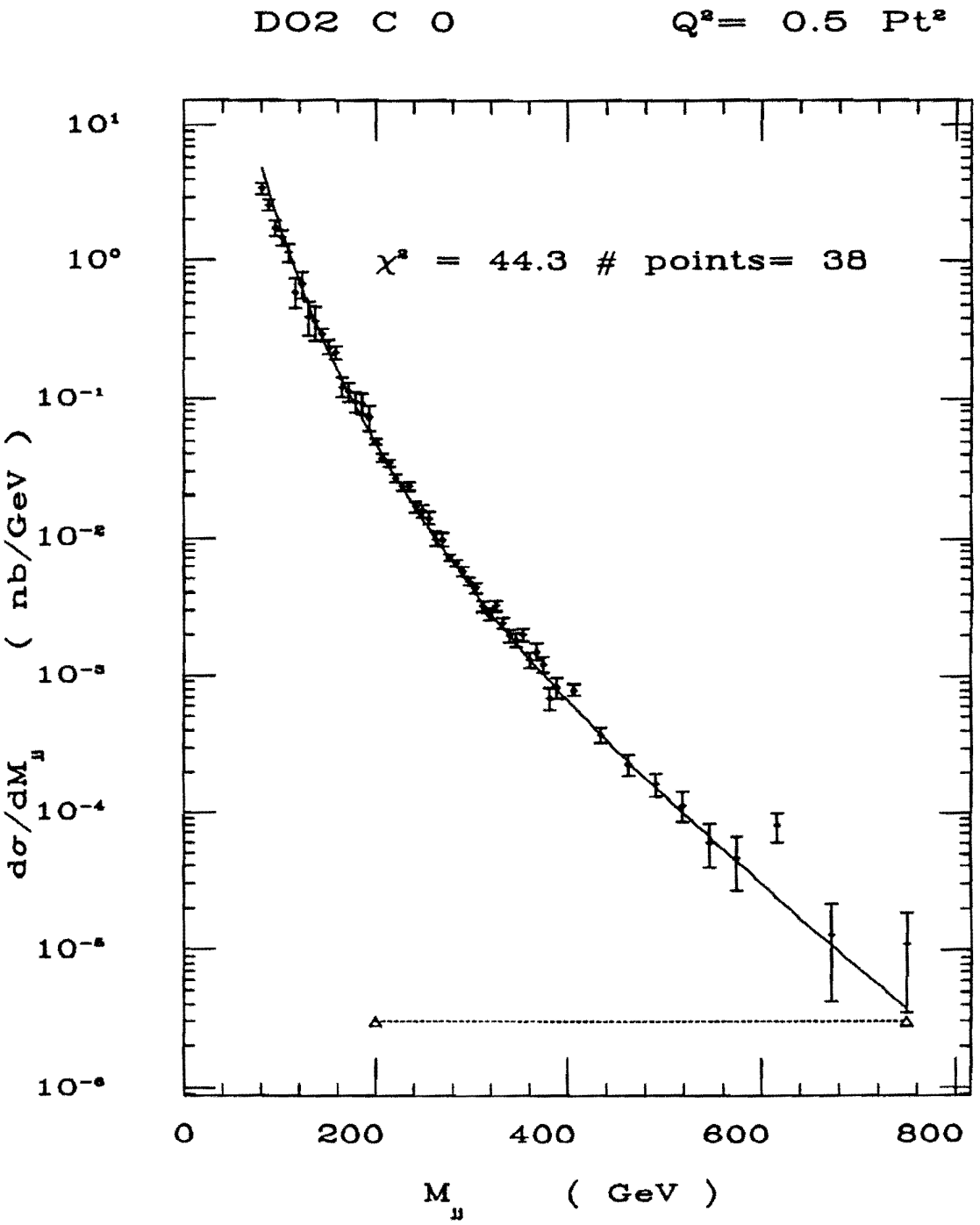

Fig 11.3 The best global fit with QCD.

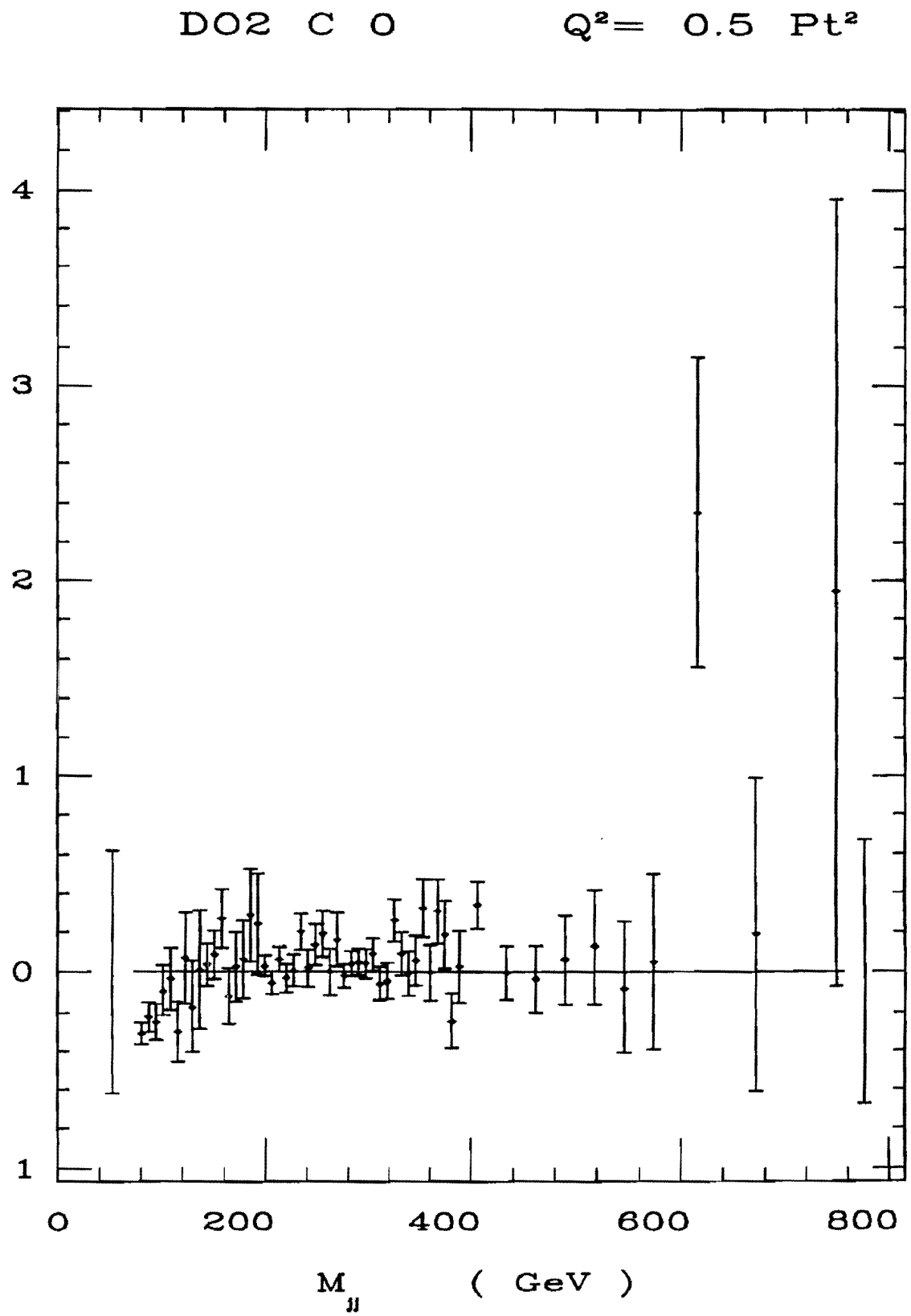

Fig 11.4 Linear plot of (data–theory)/theory of the best global fit with QCD.

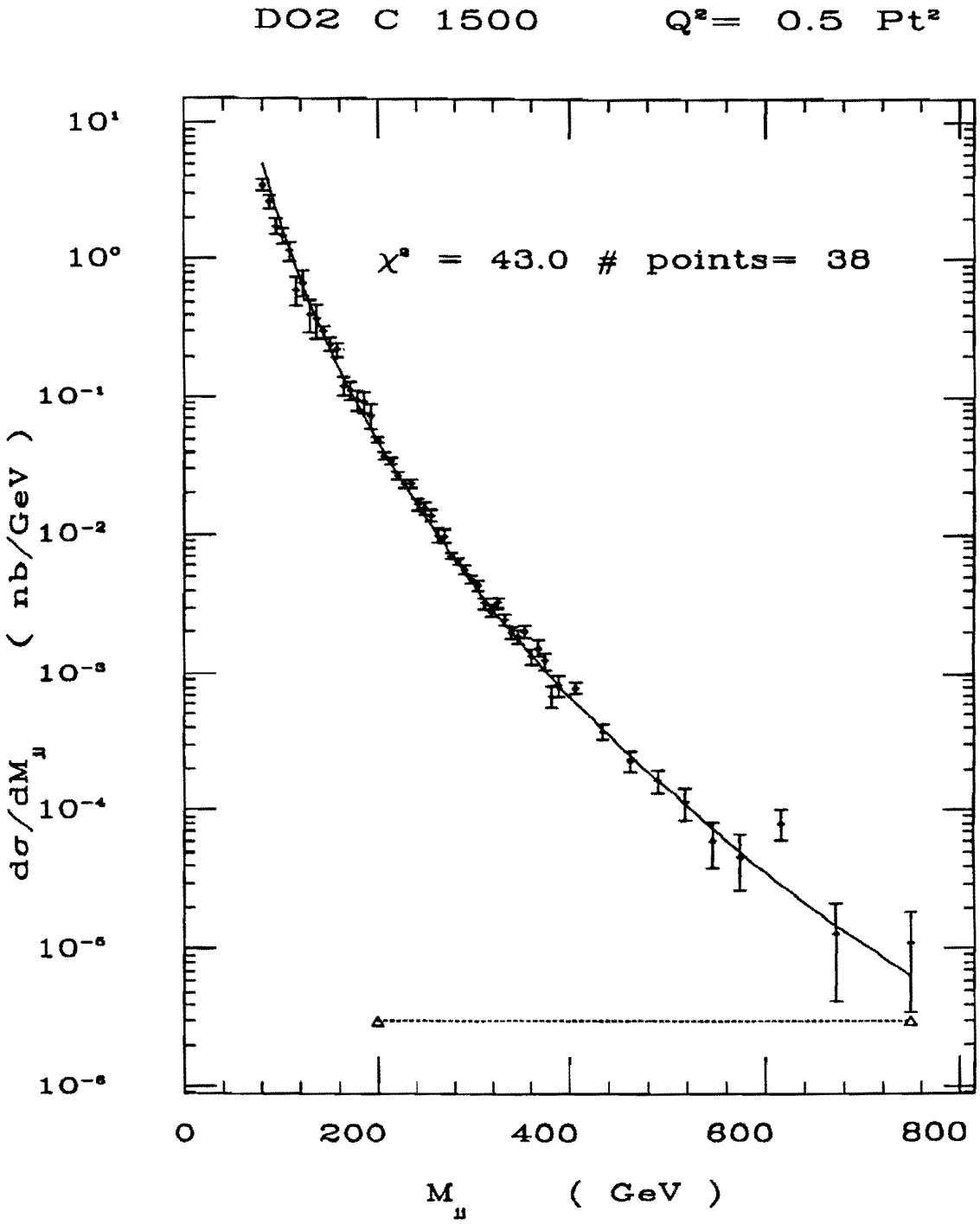

Fig 11.5 Best global fit with compositeness.

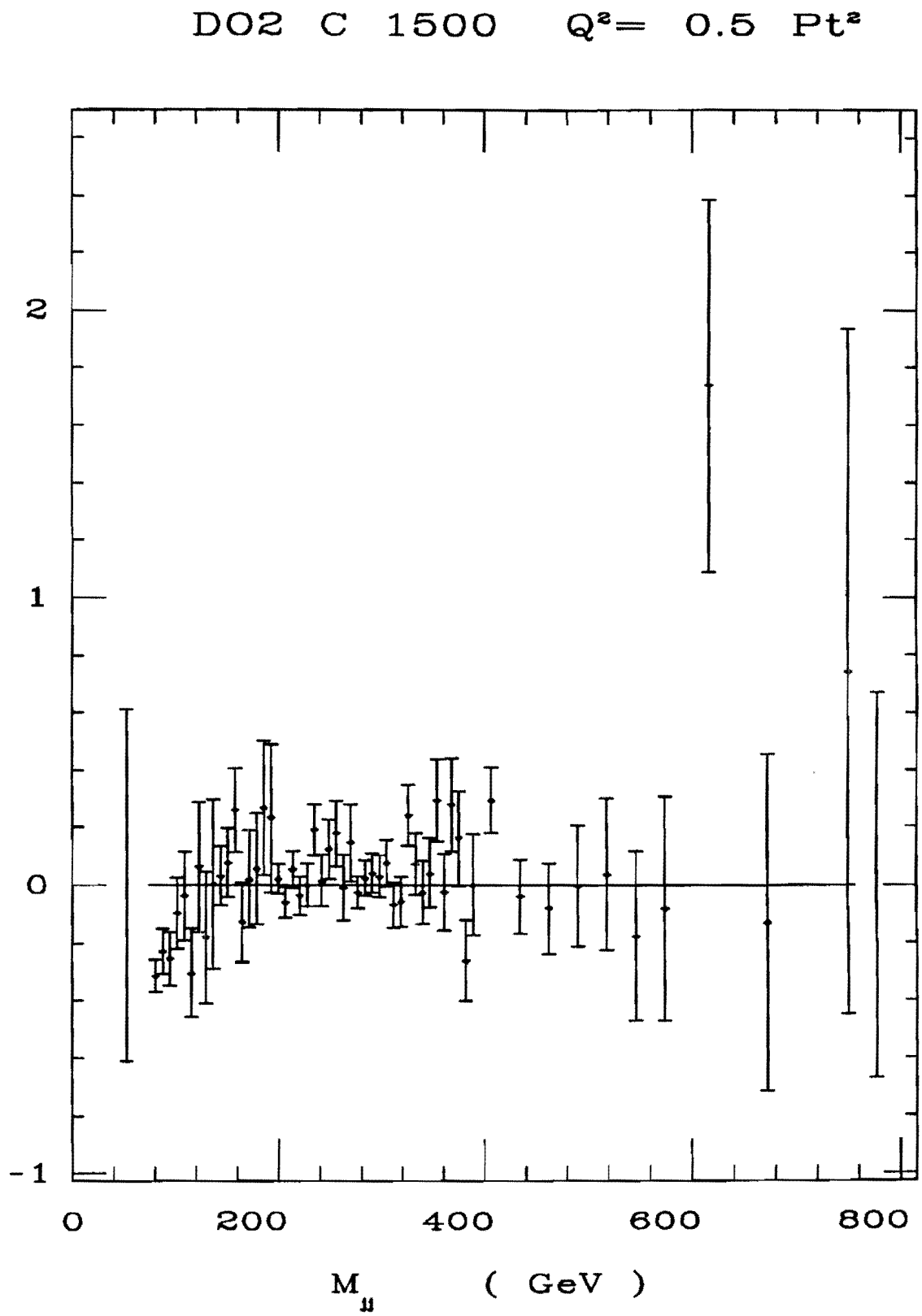

Fig 11.6 Linear plot of (data–theory)/theory of the best global fit with compositeness.

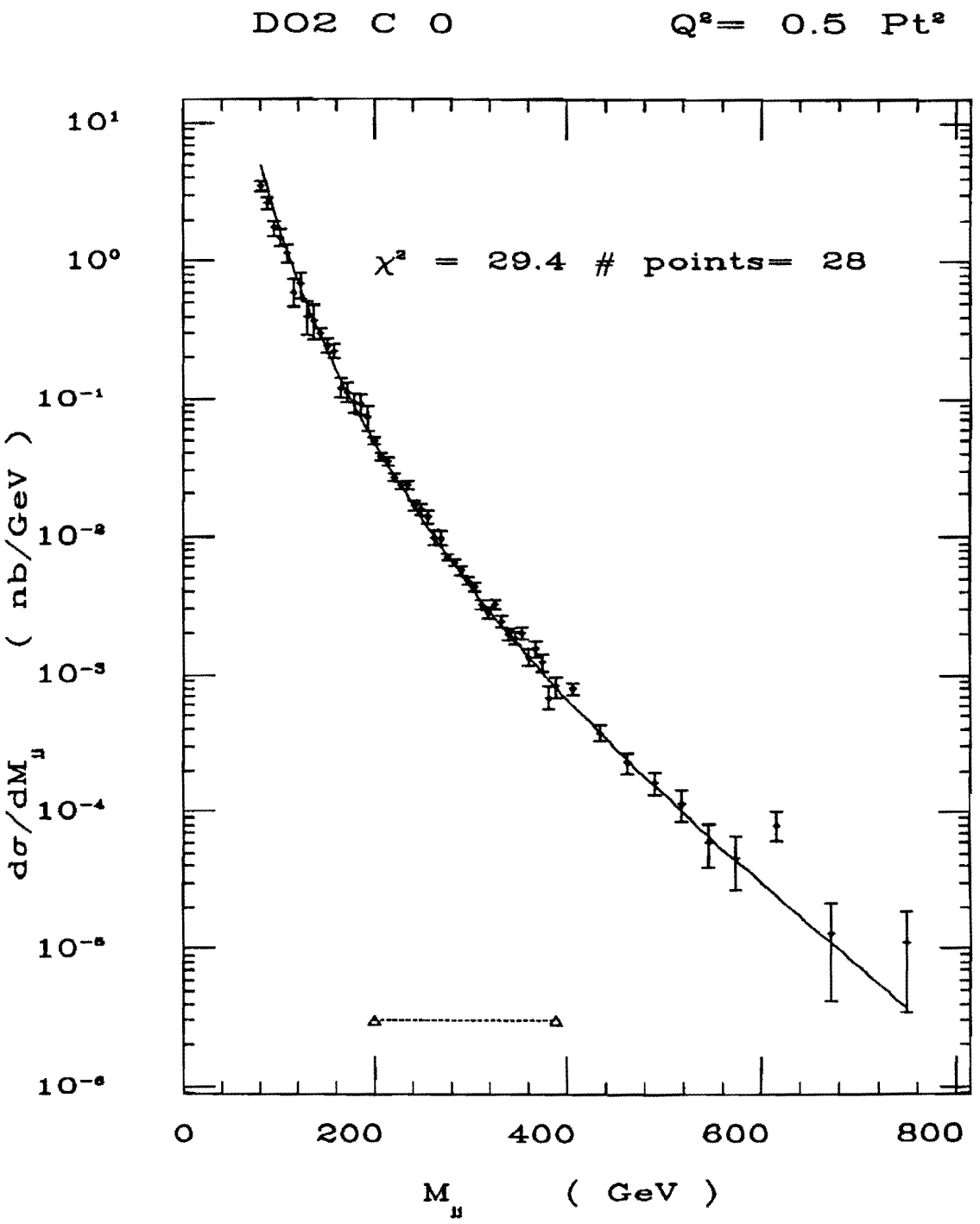

Fig 11.7 Best fit to the high mass region (M_{jj}>400 GeV) with QCD. The χ^2 in the normalization (dashed) region is quoted in the figure.

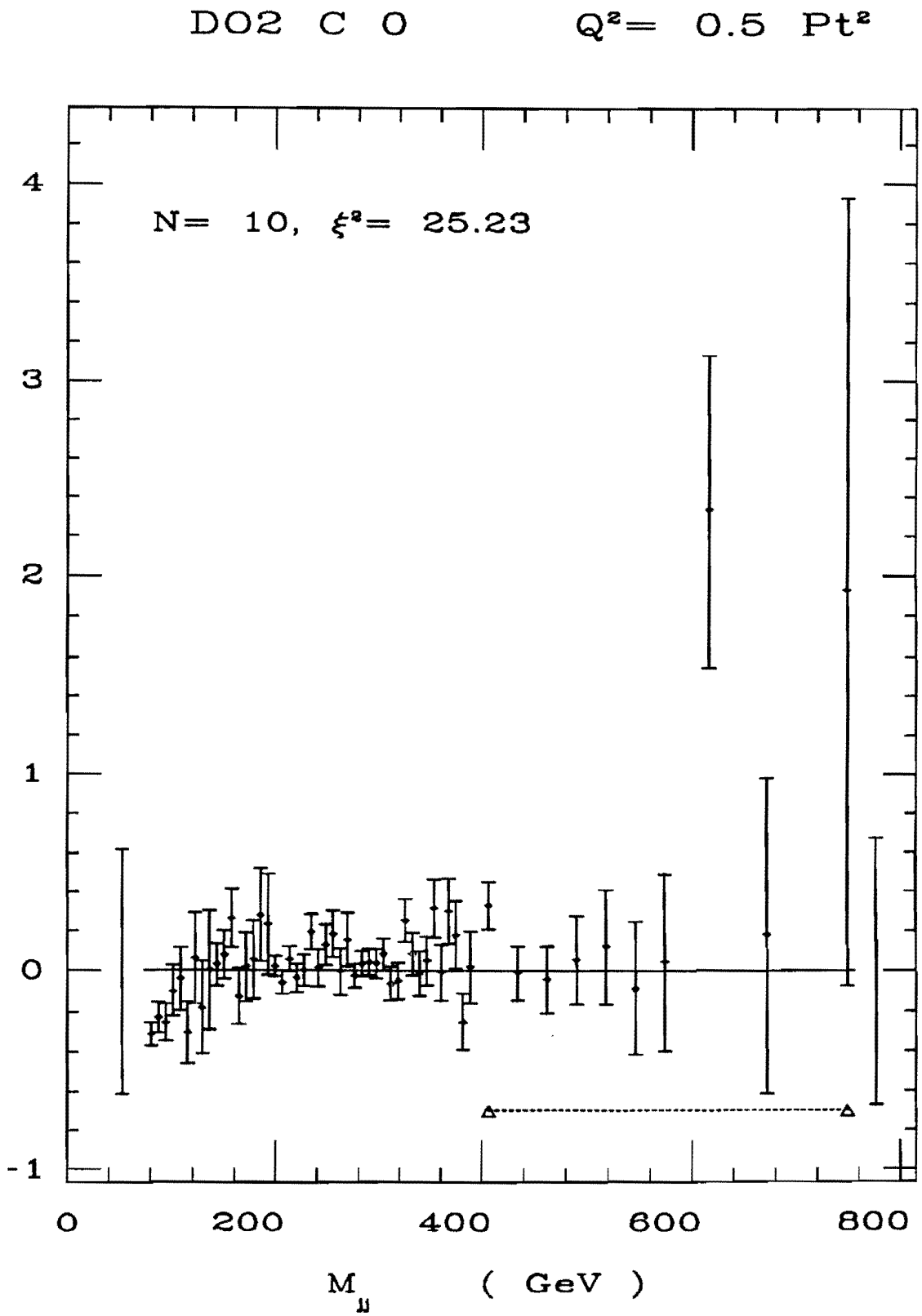

Fig 11.8 Linear plot of (data–theory)/theory for the QCD fit after normalizing to the range $200<M_{jj}<400$ GeV. The dotted line indicates the fitted range.

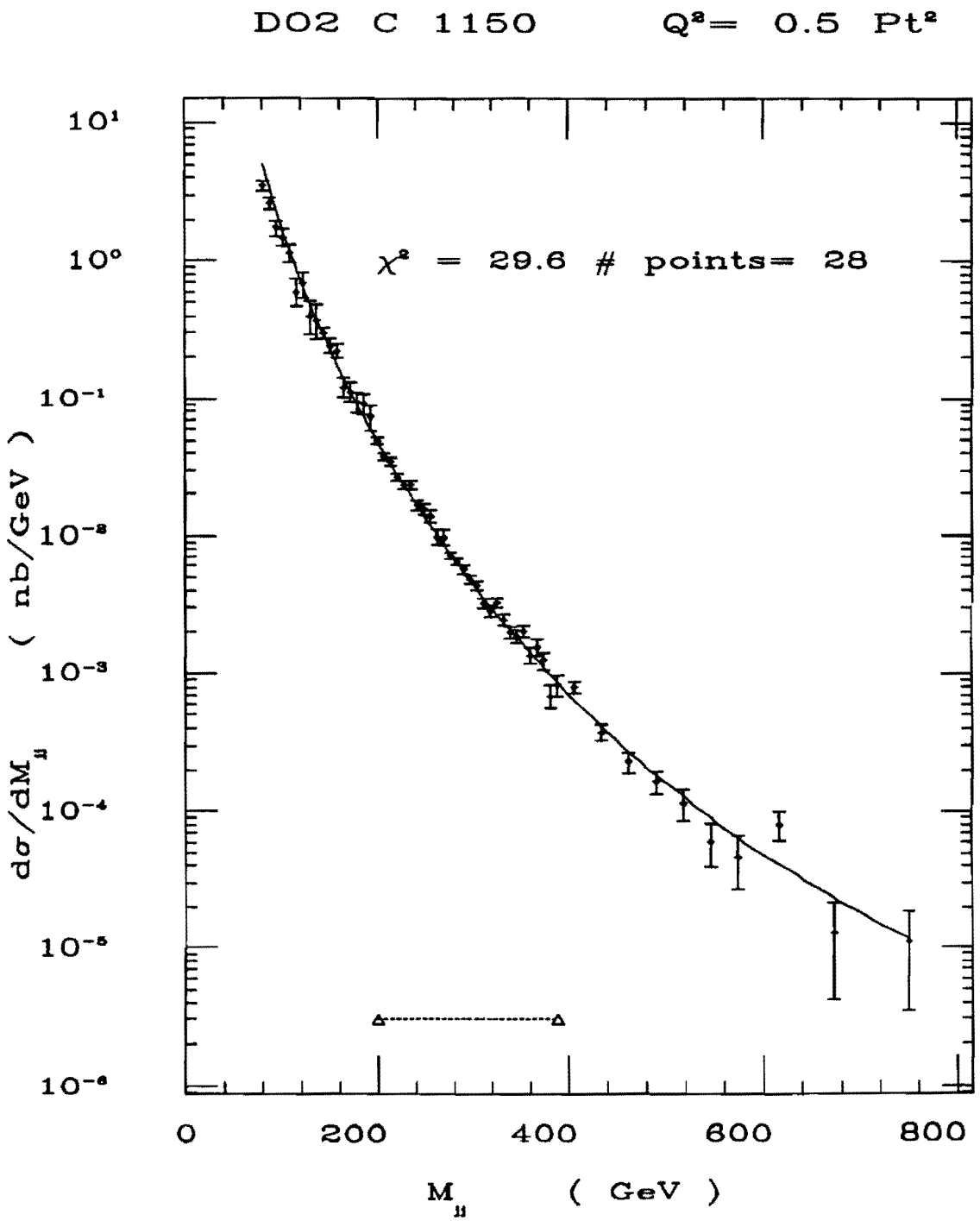

Fig 11.9 Best fit to the high mass region (M_{jj}>400 GeV) with compositeness. The χ^2 in the normalization (dashed) region is shown.

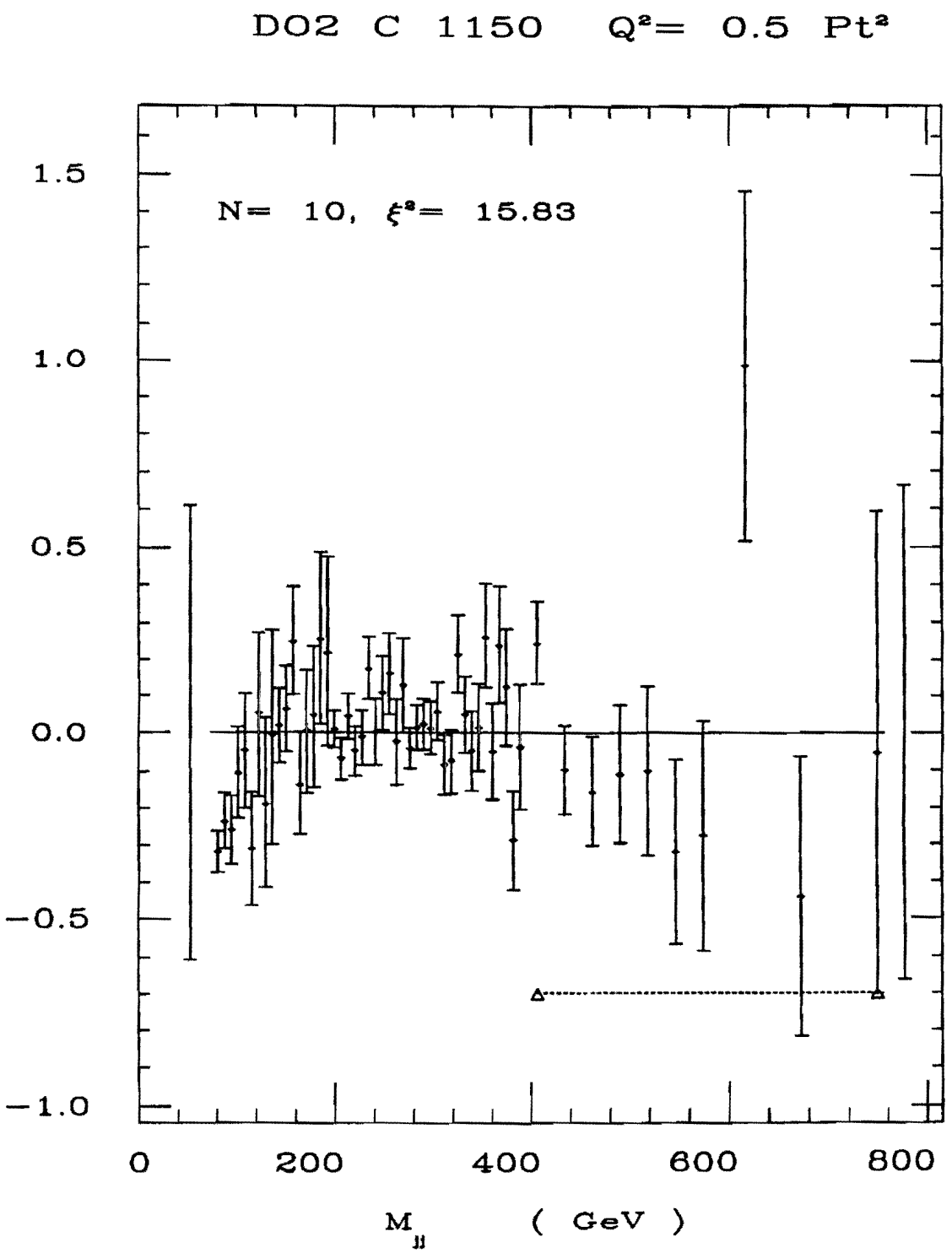

Fig 11.10 Linear plot of (data–theory)/theory for compositeness fit, after normalizing to the range ($200<M_{jj}<400$ GeV).

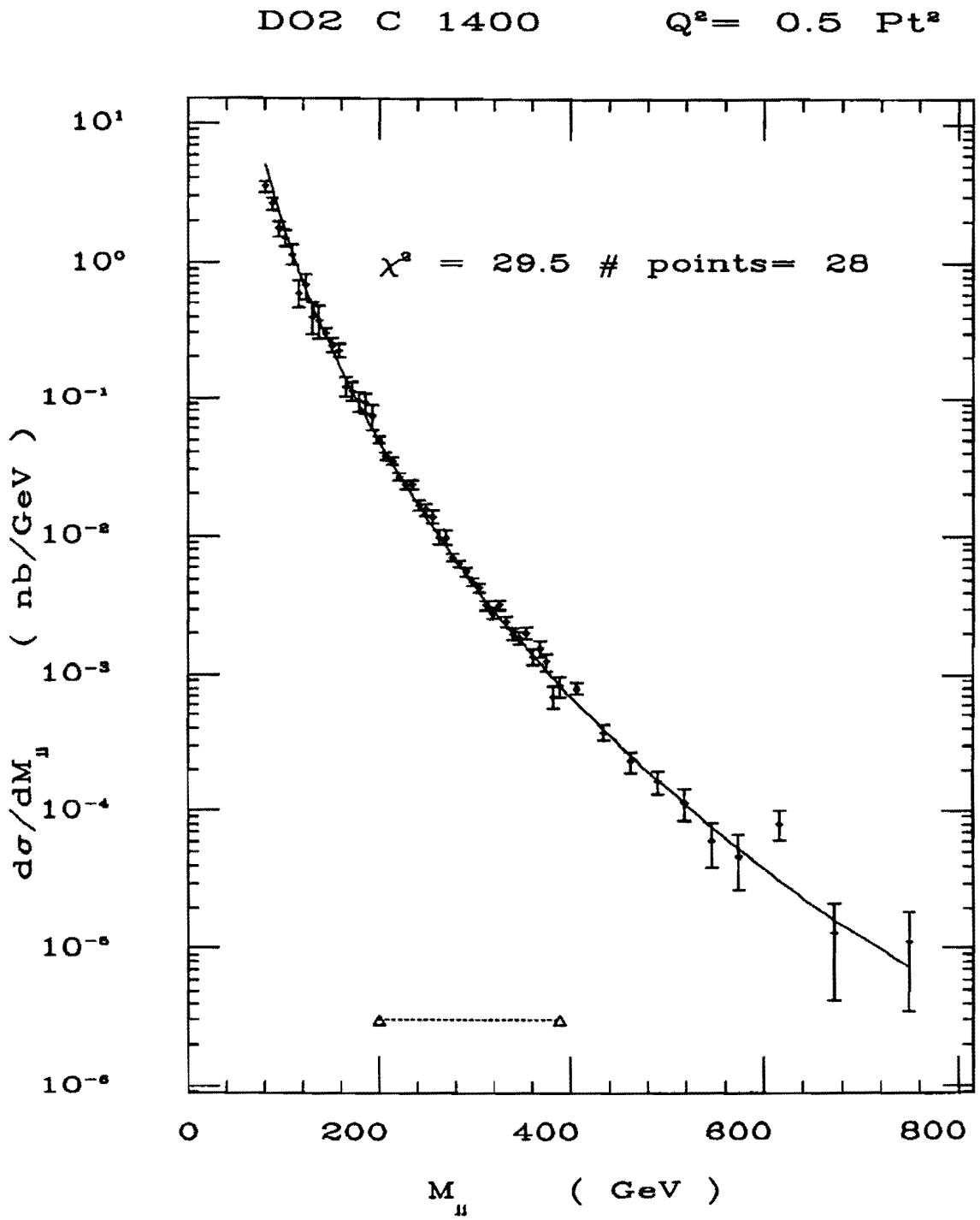

Fig 11.11 Best fit to the high mass region (M_{jj}>400 GeV) with compositeness, excluding the point at 610 GeV from the fit.

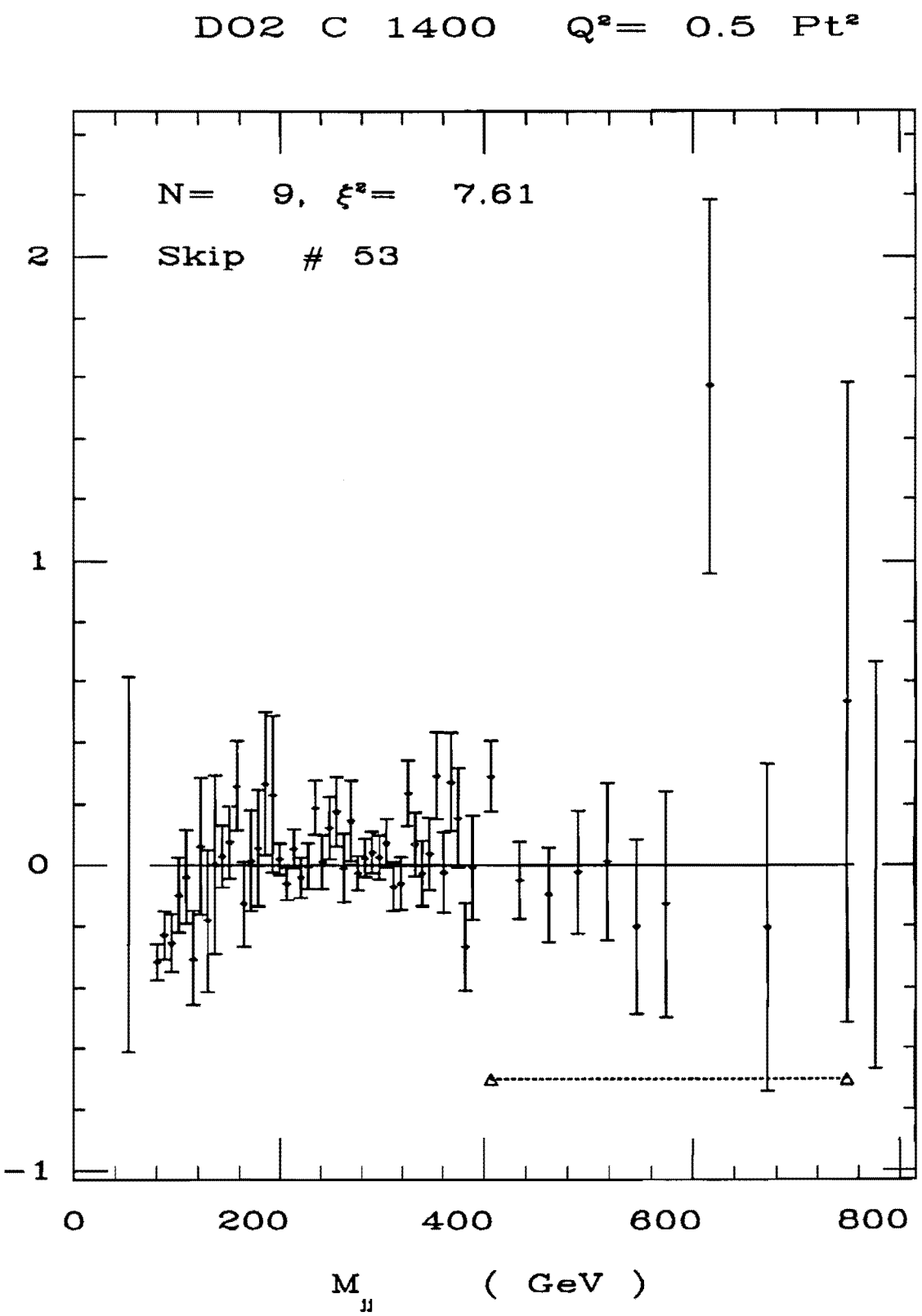

Fig 11.12 Linear plot of (data–theory)/theory from the compositeness fit, after normalizing to the range $200<M_{jj}<400$ GeV. The point at 610 GeV is excluded from the fit.

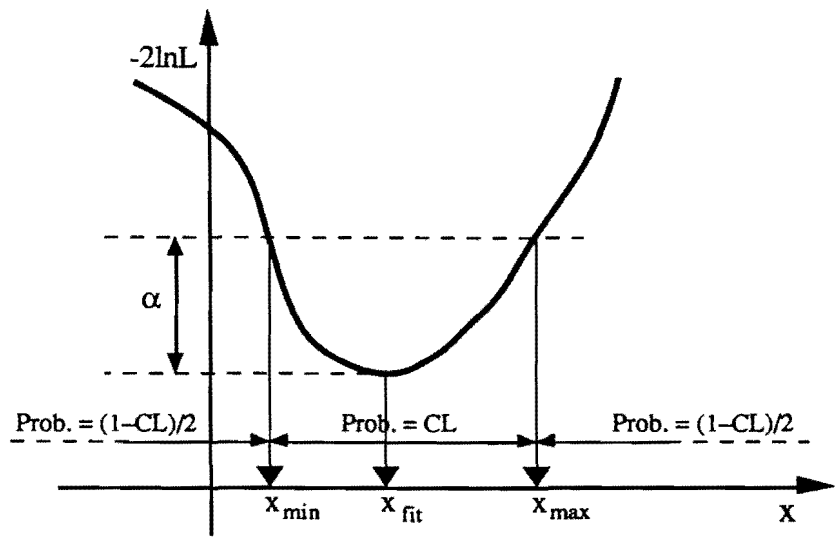

Fig 11.13 Illustration of the standard method for finding a confidence interval for a given confidence level.

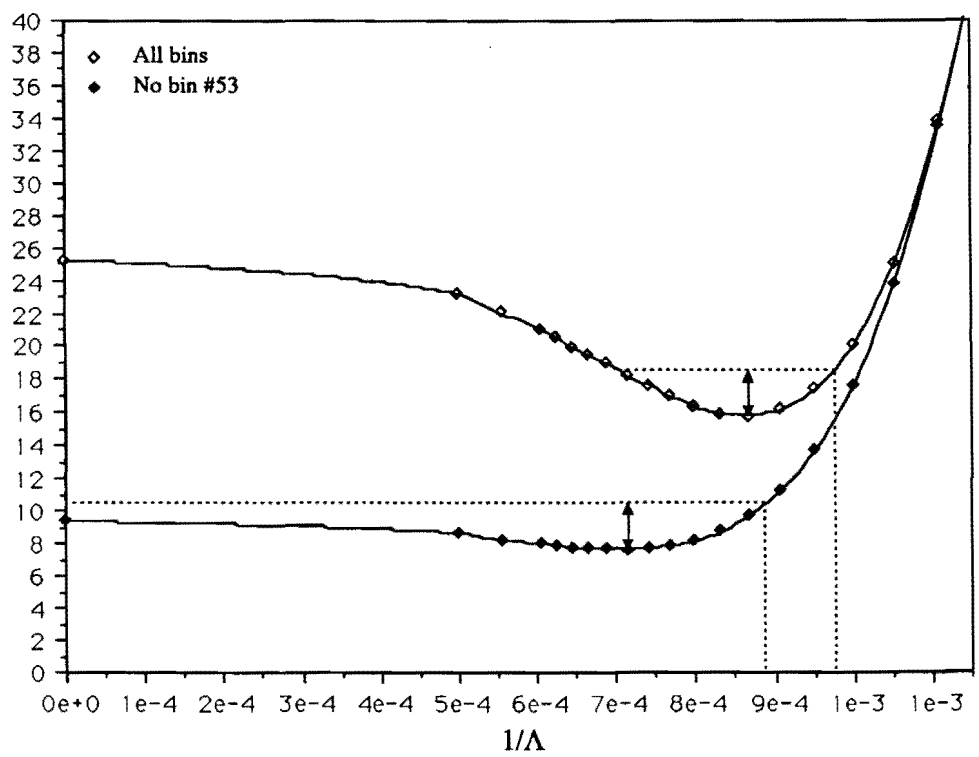

Fig 11.14 Plot of ξ^2 from Tab. 11.4. The dotted lines indicate the 95% C.L. boundaries.

REFERENCES

[1] H.D. Politzer, Phys. Rev. Lett. 30(1973) 1346 and D. J. Gross and F.Wilczek, Phys. Rev. Lett. 30(1973) 1343.

[2] D. W. Duke and J. F. Owens, Phys. Rev. D30(1984) 49.

[3] E. Eichten, I. Hinchliffe, K.Lane, C. Quigg, Rev. Mod. Phys. 56(1984) 579.

[4] F. E. Paige and S. D. Protopopescu, talk at the XVI International Symposium on Multiparticle Dynamics, 1985 (Brookhaven Nat. Lab. report BNL–37066(1985)).

[5] E. Eichten, I. Hinchliffe, K.Lane, C. Quigg, Rev. Mod. Phys. 56(1984) 684.

[6] P. H. Frampton and S. L. Glashow, Phys. Lett. 190B(1987) 157.

[7] J. Bagger, C. Schmidt, S. King, Phys. Rev. D37(1988) 1188.

[8] P. H. Frampton and S. L. Glashow, Phys. Rev. Lett. 58(1987) 157.

[9] Nucl. Instr. and Meth. A267(1988) 249–366, A268(1988) 24–104, A269(1988) 33–50, A271(1988) 387–403.

[10] S. Bertolucci et al., Nucl. Instr. and Meth. A267(1988) 301.

[11] A.Mukherjee, CDF internal note #1002(1989).

[12] Nucl. Instr. and Meth. A269(1988) 51–100.

[13] R. Carey *et al.*, CDF internal note #605(1988).

[14] J. Hauser, T. Hessing, J. Huth, CDF internal note #855(1989).

[15] D. Brown and R. Carey, CDF internal note #755(1988).

[16] S. Kuhlmann *et al.*, CDF internal note #686(1988).

[17] S. Behrends *et al.*, CDF internal note #1015(1989).

[18] R. St. Denis, Ph.D. Thesis, Harvard University (1988).

[19] P. Bagnaia *et al.*, Phys. Lett. B144(1984) 283.

[20] S. Behrends, M. D. Shapiro, E. Pare, CDF internal note #1066(1989).

[21] M. Dell' Orso, P. Giannetti, G. Punzi, CDF internal note #896(1989).

[22] S. Dell'Agnello and G. Punzi, CDF internal note #1064(1989).

[23] B. Hubbard, Ph.D.Thesis, Lawrence Berkeley Lab., LBL–27687(1989).

[24] T. Hessing, priv. comm.

[25] S. Kuhlmann, J.Yoh, CDF internal note #548(1987).

[26] T. Hessing, CDF internal note #957(1989).

[27] D. Brown, S. Kannappan, M. Shapiro, CDF internal note #753(1988).

[28] S. Dell' Agnello,M. Dell'Orso,P. Giannetti,M. Mangano,G. Punzi, CDF internal note #1058(1989).

[29] Y.–D. Tsai, Ph.D. thesis, University of Chicago(1989).

[30] M. Dell'Orso, P. Giannetti, G. Punzi, CDF internal note #1056(1989).

[31] G. Marchesini and B. Webber, Nucl. Phys. B310 (1988) 461.

[32] FORTRAN program by M.Mangano.

[33] S. D. Ellis, Z. Kunszt, D. E. Soper, Phys. Rev. Lett. 62(1989) 726 and Phys. Rev. D40(1989) 2188.

[34] See, for instance, W. T. Eadie *et al.*, "Statistical Methods in Experimental Physics", North–Holland (1971), or M. G. Kendall, A. Stuart, "The Advanced Theory of Statistics", Charles Griffin & Co., London.

[35] E. Eichten, I. Hinchliffe, K.Lane, C. Quigg, Rev. Mod. Phys. 56(1984)592